SYNTHESIS AND PHENOTYPIC DISCOVERY OF MOLECULAR PROBES OF BIOLOGICAL SYSTEMS

By

J. Matthew Meinig

Submitted to the graduate degree program in Medicinal Chemistry and the Graduate Faculty of the University of Kansas in partial fulfillment of the requirements for the degree of Doctor of Philosophy.

_____

Chairperson: Dr. Blake R. Peterson

_____

Dr. Michael F. Rafferty

_____

Dr. Robert P. Hanzlik

_____

Dr. Mario Rivera

_____

Dr. Jeffrey P. Krise

Date of defense: July 20, 2015, 9:00 a.m.

School of Pharmacy, Room 1020

The Dissertation Committee for J. Matthew Meinig

certifies that this is the approved version of the following dissertation:

SYNTHESIS AND PHENOTYPIC DISCOVERY OF MOLECULAR PROBES OF BIOLOGICAL SYSTEMS

_____

Chairperson: Dr. Blake R. Peterson

Date Approved: July 20, 2015

ABSTRACT

The Peterson laboratory has had a long-standing interest in fluorescent probes of biological systems. My research in the Peterson group has focused on the design, synthesis, and biological evaluation of fluorescent small molecules that exhibit specific patterns of subcellular localization and studies of their downstream biological effects. The relationship between this approach and the strategy of phenotypic drug discovery is described in Chapter 1. Chapter 2 describes the discovery of the intrinsic blue fluorescence of the potent anti-cancer/anti-viral compound AKT inhibitor-IV (AKTIV), and how we used this property to discover that its mechanism of biological action involves accumulation in mitochondria and associated effects on mitochondrial morphology and cellular bioenergetics. Chapter 3 describes the synthesis of a novel class of hydrophobic fluorinated rhodol fluorophores that selectively accumulate in the endoplasmic reticulum. These fluorophores were shown to enable delivery of linked small-molecules to control a specific biological pathway in this organelle. Building on these studies, Chapter 4 describes screening of a variety of fluorescent probes against the vertebrate model organism zebrafish (*Danio rerio*). These studies led to the discoveries that hydrophobic rhodamines can be used to target zebrafish mitochondria, and acid-activated fluorophores can accumulate in acidic tissues of the embryonic yolk. Chapter 5 describes another project involving the synthesis of novel cholesteryl dimers and analysis of the *in vitro* stability of liposomes that incorporate these compounds.

ACKNOWLEDGEMENTS

My sincerest thanks go to my advisor, Prof. Blake R. Peterson, for his invaluable support and mentorship over my graduate career. Under his guidance, I have had the opportunity to work on a number of diverse and gratifying projects in chemical biology. I would also like to thank the entire faculty of the Department of Medicinal Chemistry for their support both in and out of the classroom and laboratory. Special thanks go to the members of my defense committee, Dr. Mike Rafferty, Dr. Robert Hanzlik, Dr. Jeff Krise, and Dr. Mario Rivera, for their time and consideration.

I would like to also thank members of the Peterson group that contributed to this work and other projects I have participated in, specifically Dr. Liqiang Fu, Dr. Chamani Perera, Dr. Aaron Bender, and Dr. Zach Woydziak. Additionally, I would like to thank Dr. David Hymel, Molly Lee, Kelsey Knewston, and Gavin Gao for excellent feedback and friendship throughout the years. I also greatly appreciate our collaboration with the Rodney Ho group.

Finally, I would like to thank my wife, Meaghan, my parents, Jim and Linda, and my sisters, Laura and Katherine, for their unwavering support of my lifelong love of science and motivation throughout my graduate career.

TABLE OF CONTENTS

LIST OF FIGURES

Chapter 1

Phenotypic Drug Discovery and Subcellular Targeting of Small Molecules

1.1 Phenotypic Approaches for Discovery of Novel Mechanisms

Most first-in-class drugs are discovered through a process termed phenotypic screening.[1-2] These agents exhibit novel mechanisms of action and are crucial for tackling neglected diseases or diseases with suboptimal therapies. This screening approach uses models of disease in cell culture or *in vivo* to identify candidate therapeutics without specifying a molecular target (Figure 1.1, compare panels A and B). Between 1999 and 2008, 28 out of 50 approved small-molecule therapies with new mechanisms of action were derived from some type of phenotypic screen (Figure 1.1, panel C).[1] The remaining small-molecule agents were derived from a target-based approach, exemplified by screening and optimizing a small-molecule inhibitor against an expressed protein target *in vitro*, typically based on structural data. This target-based approach is the principal tool used to identify "follower" drugs, where second- or third-generation molecules share a mechanism of action with first-in-class agents after a target has been clinically validated. The heavy reliance of the pharmaceutical industry on screening of large chemical libraries, and an infrastructure based on target-based screening and optimization, is being challenged, as it has been suggested the investment in this approach has not significantly increased the number of agents brought to market. Although the distinction between phenotypic and target-based

discoveries can be controversial due to modern approaches that combine both techniques,[2] it is clear that phenotypic screening plays an important role in the development of novel therapies in the modern drug discovery process.

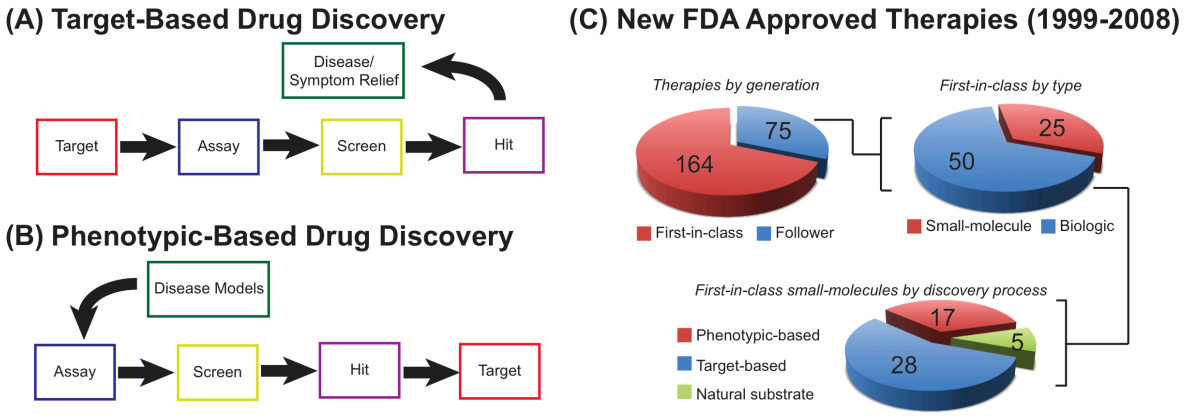

Figure 1.1. General workflows of target-based (Panel A) and phenotype-based (Panel B) drug discovery. New therapies approved by the FDA, organized by generation, type, and origin of discovery, are shown in Panel C.

The power of phenotypic discovery is attributed to a number of factors. First, this approach, unbiased by interest in a specific target protein, does not presume a cause-and-effect relationship between a specific target and downstream modulation of the disease, which can lead to serendipitous discoveries.[3] Second, successful cell-based and *in vivo* screening methods requires certain favorable bio-pharmacokinetic properties such as permeability, tissue accumulation, and metabolism in order for compounds to be active. In contrast, the pharmacokinetics of candidates optimized *in vitro* in a target-based screen typically must be optimized after screening.

Phenotypic screening in earlier eras of pharmaceutical development relied heavily on direct experimentation in mammals such as mice or rats. Considering the significant cost of doing modern animal-based screens on large scales, phenotypic assays today may involve cell-based models, invertebrate animals, and small vertebrate model organisms. Modern genetic techniques, such as CRISPR/Cas9 genome editing,[4] allow easier entry into novel models for this approach. Advances in high-throughput cellular and *in vivo* screening techniques allow more quantitative approaches based on microscopy[5] and flow cytometry.[6] High-content phenotypic assays can be used for high-throughput screening of small-molecule libraries.[7]

1.2 Fluorescent Probes in Phenotypic Screens

Fluorescent assays have played a large role in phenotypic screens because fluorescence can often be bright, easily visualized, and readily quantified in biological systems.[8] Both fluorescent transgenes and small-molecule probes have been used in phenotypic assays, and often both approaches compliment each other in multicolor experiments. The former typically involves the expression of fluorescent proteins, such as green-fluorescent protein (GFP), and following changes in expression, distribution, or lifetime. For example, a phenotypic screen looking for changes in the cellular distribution of the protein FOXO1 was originally used to discover AKT Inhibitor-IV, the small-molecule that is central to Chapter 2 of this dissertation.[9] Other examples include siRNA screens for genes affecting trafficking of the mannose-

6-phosphate receptor, as it relates to neurodegenerative diseases,[10] and small-molecule screens against ER-mitochondrial trafficking and morphology related to models of Parkinson's disease.[11]

Compared with fluorescent proteins, fluorescent small molecules have been less frequently used in phenotypic screens. This is likely due to the greater complexity involved in creation of a chemical probe verses a genetic construct for most biologists. However, small-molecule fluorophores have great potential for novel phenotypic screens because of their diverse chemical, structural, and photophysical properties. For example, small-molecule fluorescent probes have been used in phenotypic screens for vacuolization in the malarial parasite *P. falciparum*,[12] protection of the mitochondrial network critical in neurodegeneration,[13] and cytotoxicity in the blood fluke *Schistosoma*.[14] One interesting example of using small-molecule fluorophores in a phenotypic assay incorporated five different fluorescent organelle markers with unique spectral profiles to simultaneously probe the distribution and morphology of the nucleus, the mitochondria, the endoplasmic reticulum, the Golgi apparatus, and the actin network.[15] A major focus of this dissertation is studies of the biological properties of fluorescent probes, discovered by phenotypic screening, that accumulate in specific organelles of mammalian cells through different mechanisms of action.

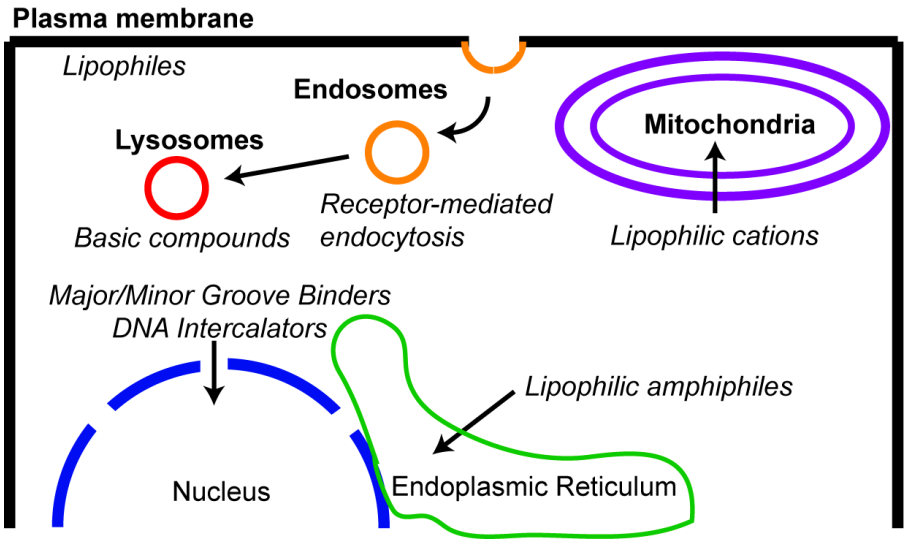

Figure 1.2. Common organelles of mammalian cells and mechanisms for targeting of these subcellular compartments with small molecules.

1.3. Targeting Subcellular Compartments with Small Molecules

Mammalian cells are a highly complex biological system. This system is compartmentalized into various cellular organelles that include specific subsets of biomolecules (Figure 1.2). The cell maintains this non-uniform distribution of biomolecules through complex sorting systems. Proteins that are targeted to subcellular organelles or subdomains of organelles include peptide sequences encoding a cellular "address." For example, proteins destined for localization in the endoplasmic reticulum (ER) include the tetrapeptide sequence KDEL at the C-terminus.[16-18] This KDEL peptide signals for retrograde transport from the Golgi or cytosol back to the ER via specific receptors (KDEL1-3).[18] Phospholipids, primarily synthesized in the ER and mitochondria, are similarly asymmetrically distributed in different subcellular membranes.[19-20] This asymmetry is maintained by a system of protein transporters and controlled fusion of membrane vesicles.[21]

Since drug targets are non-uniformly distributed throughout the cell, effective pharmacological agents must be able to reach the intended target, while avoiding accumulation in non-relevant organelles.[22-23] As previously mentioned, target-based drug discovery typically yields candidates that must be further optimized for pharmacokinetic properties. In order to make more "drug-like" molecules, this optimization may involves calculated and measured parameters such as lipid partitioning coefficients, hydrogen bond donors and acceptors, oral availability, and tissue distribution. However, for small molecules that affect intracellular targets, subcellular distribution represents an additional potentially important factor that has not been traditionally considered during drug development.

The targeting of bioactive compounds to specific subcellular compartments is typically achieved by one of two mechanisms. First, small-molecules can specifically accumulate in a subcellular compartment due to intrinsic physicochemical properties. Alternatively, subcellular delivery can result from interaction with an organelle-specific resident protein or linkage to a targeting signal. Fluorescent probes that accumulate in specific organelles allow investigation of mechanisms of subcellular targeting because their specific accumulation can be easily observed by fluorescence microscopy (see structures in Figures 1.3 and 1.5). In the following sections, the concept of subcellular targeting will be further defined by examples of small-molecules that accumulate in cellular compartments due to interaction with proteins, lipids, or unique physicochemical properties of an organelle.

1.3.1 The Plasma Membrane

The plasma membrane, a lipid bilayer that separates the extracellular space from the cytosol, houses a variety different drug targets. These drug targets include major families of proteins such as the G-protein coupled receptors (GPCRs), receptor tyrosine kinases, viral fusion proteins, and ion channels. Drugs that reach the systemic circulation typically have free access to targets on the extracellular side of the plasma membrane. However, membrane anchoring by membrane integral peptides or lipids has been shown to be an effective tool in limiting the scope of the drug to the plasma membrane to enhance efficacy.[24]

Enfuvirtide (T-20/Fuzeon)[25] is a first-in-class viral fusion inhibitor used to treat infection by multi-drug resistant HIV. This drug is a synthetic 36-amino acid peptide the mimics the gp41 viral protein and prevents fusion of the virus with the plasma membrane of the host. When enfuvirtide was expressed fused to a membrane-spanning domain of the low-affinity nerve growth factor receptor (LNGFP), its potency against entry of HIV-1 was improved 20-fold compared with the non-anchored drug.[26] Another peptide fusion inhibitor termed C34, based on a different portion of the pg41 sequence, was shown[27] to also be a potent inhibitor of HIV-1 fusion (IC_{50} = 205 pM) and a membrane-targeted cholesterol-linked analogue was shown to improve potency by over 50-fold (IC_{50} = 4 pM). The cholesterol-linked C34 also proved to be effective against enfuvirtide-resistant viral strains.[27] These examples of plasma membrane anchoring of fusion inhibitors illustrates potential advantages of localizing drugs to the same cellular compartment as their molecular target by controlling non-productive

diffusion. The cholesterol-linked C34 has been showed to preferentially associate with lipid rafts on the plasma membrane, exemplifying the value of domain-specific targeting for small-molecule drugs within an organelle.[28] The benefit of subcellular targeting by plasma membrane anchoring has also been demonstrated in a variety of other drug classes including hepatitis B viral fusion inhibitors,[29] β-secretase inhibitors,[30] and a class of lipidated GPCR modulators termed Pepducins.[31]

As the first lipid membrane encountered by an agent, the plasma membrane can accumulate highly lipophilic molecules such as the long chain carbocyanine dye DiI (Figure 1.3 panel A).[32] Fluorescent probes, such as DiI, targeted to the plasma membrane can be useful for studies of subcellular localization of agents by fluorescence microscopy. Because dyes of this category stably incorporate into the plasma membrane, they are also commonly used to track cell lineages and migration *in vivo*.[33]

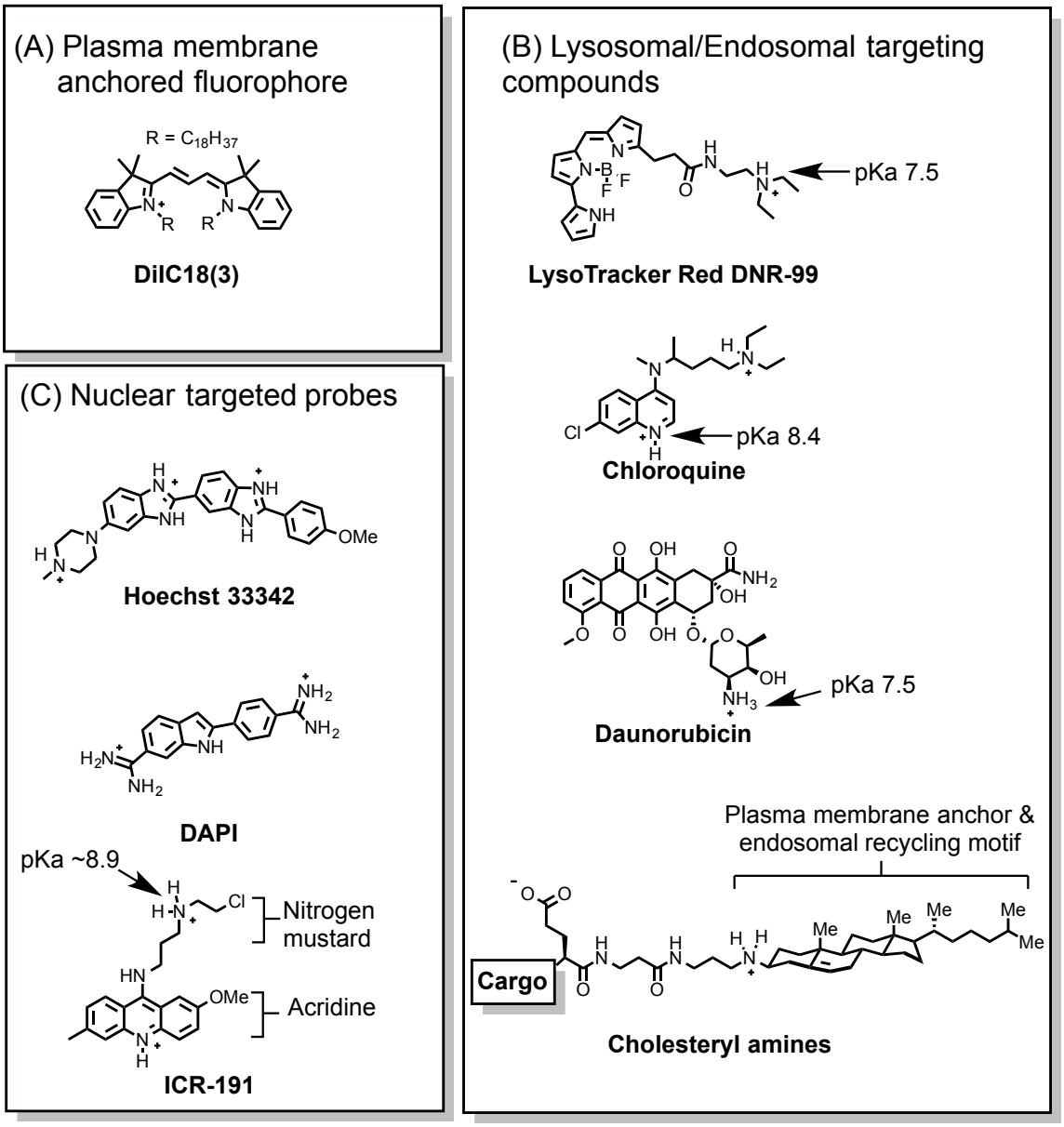

Figure 1.3. Structures of molecular probes localized to specific subcellular regions. Panel A: The plasma-membrane anchored fluorophore DiI. Panel B: The lysosomotropic agents LysoTracker Red DNR-99 (Life Technologies), chloroquine, and the anticancer agent daunorubicin. Cholesterylamines with this general structure are typically localized to the plasma membrane and early endosomes. Panel C: Nuclear-localized compounds include the DNA minor-groove binders Hoechst 33342 and DAPI, and the acridine mutagen ICR-191 (pKa calculated with ChemAxon MarvinSketch 6.2).

1.3.2 Endosomes and Lysosomes

The endosomal/lysosomal system, associated with the plasma membrane by dynamic membrane trafficking processes, is a series of membrane-enclosed compartments responsible for endocytosis, receptor trafficking, and digestion of nutrients. Endocytosis encompasses a number of mechanisms, including pinocytosis and receptor-mediated endocytosis (RME), where a cell internalizes extracellular material by invagination of the plasma membrane to generate vesicles that fuse to form endosomes that subsequently mature and fuse with lysosomes. The transition from early endosomes to late endosomes (pH ~6) and lysosomes (pH ~5) is accompanied by lowering of the luminal pH due to the protein vacuolar ATPase (V-ATPase).[34] Interestingly, it has been shown that cancer cells typically exhibit elevated endosomal pH compared with normal cells.[35-38] However, resistance to the anticancer drug Adriamycin in MCF-7 cells was shown to correlate with a decrease in endosomal pH, resulting in extensive endosomal trapping of the drug and, thereby, a decreased free concentration.[35] A fluorescent probe that visualizes the *ex vivo* acidity caused by V-ATPase is discussed in Chapter 4 of this dissertation. Due to the relatively low pH of these compartments compared with the cytosol, weakly basic molecules such as the BODIPY fluorophore LysoTracker Red (pKa = 7.5, Life Technologies, Figure 1.3 panel B) can selectively accumulate in the lumen of these organelles.[39-41] This phenomena of lysosomal accumulation is termed lysosomotropism and is a common feature of moderately basic compounds (pKa ~ 7-9).[41] The antimalarial drug chloroquine (pKa = 8.5, Figure 1.3 panel B) is known to accumulate in

lysosomes and is used in *in vitro* experiments to raise lysosomal lumen pH.[39] The topoisomerase inhibitor daunorubicin is also lysosomotropic (pKa = 7.5, Figure 1.3 panel B),[42] and an increase in lysosomal trapping of daunorubicin coupled due to a decrease in the pH of the lumen of the lysosome has been implicated in clinical drug resistance.[43]

Antibody-drug conjugates (ADCs) are a clinically successful class of drugs useful for targeting of cancer cells that overexpress distinctive cell-surface receptors.[44-45] The antibody-receptor complex undergoes RME and enters endosomes and/or lysosomes. A linked cytotoxic warhead can then be released in these acidic compartments from an acid-labile linker such as a hydrazone, proteolytic cleavage of a linker, or complete degradation of the targeted antibody. Trastuzumab emtansine (marketed as Kadcyla), used to treat HER2-positive breast cancer, is composed of a monoclonal antibody that binds the receptor HER2 linked to the tubulin-binding agent maytansine.[46-47] Upon RME, the antibody-receptor complex cycles through endosomal compartments, and the antibody is eventually degraded in the lysosome, which releases the potent cytotoxic agent maytansine. Brentuximab vedotin[48-50] (marketed as Adcetris), a antibody against CD30 linked to the tubulin binding agent monomethyl auristatin E (MMAE), is used clinically to treat several types of lymphoma. In lysosomes, MMAE is liberated from the antibody by the protease capthesin B.[49, 51] An increasing pipeline of ADCs[44, 52] highlights the utility of targeted-release of potent cytotoxins in the endosomal/lysosomal system after RME.

The Peterson laboratory has extensively studied mimics of cell surface receptors based on analogues of cholesterol. Probes derived from cholesterylamine (Figure 1.3, panel B)[53] have been shown to rapidly cycle (recycling half-life ~3 min in Jurkat lymphocytes) between the plasma membrane and early endosomes, similar to the kinetics of trafficking of cell surface receptors during RME Examples of using these synthetic cholesterylamines to deliver covalent or non-covalent cargo to the endosomal/lysosomal system include fluorescent small-molecules,[54-55] IgG,[56] vancomycin,[57] and membrane-lytic peptides.[58] The precise mechanism of how these cholesterylamines incorporate into membranes, an active area of investigation by the Peterson laboratory, appears to involve a receptor-mediated process.[59] These synthetic mimics of cell-surface receptors provide a unique tool for targeting of cargo to the lumen of endosomes.

1.3.3 The Endoplasmic Reticulum

The endoplasmic reticulum (ER) is responsible for the synthesis of secreted and integral membrane proteins, lipid production, and calcium homeostasis. Little is known about targeting the ER with small molecules, but it has been proposed[23, 60] that amphipathic and moderately lipophilic compounds can selectively associate with the cholesterol-poor membranes of the ER. The commercial fluorophore ER-Tracker Blue-White DPX is widely used for ER-imaging, although its specific mechanism of accumulation in this organelle has

not been studied.[61] A novel fluorophore that selectively targets and accumulates in the ER is described in Chapter 3 of this dissertation.

Because of the importance of the ER in protein homeostasis, the delivery of protein and peptide-based agents to this organelle is of interest. In MOLT-4 cells, ER-specific targeting was achieved by treating cells with an exogenous derivative of green-fluorescent protein (GFP) containing an N-terminal cell-penetrating TAT peptide and the C-terminal ER-localization sequence KDEL.[62] This approach was used as a proof-of-concept for a dual TAT/KDEL ER-targeting technique. In a related strategy, some natural protein toxins hijack the cellular trafficking machinery, translocating the toxin from the extracellular environment through the Golgi apparatus and ER.[63-65] One such toxin, Shiga toxin, is the primary virulence factor produced by *S. dysenteria*. This toxin binds to glycolipid globotriaosylceramide (Gb3, also known as CD77) on the plasma membrane.[66] Following retrograde transport to the cytosolic face of the ER membrane, Shiga toxin inhibits protein synthesis by catalytic removal of an adenosine from the 60S subunit of the ribosome.[67] The ability of Shiga toxin to hijack the cellular trafficking machinery for ER-specific targeting has garnered interest in the delivery of other agents to this important organelle. When dendritic cells were treated with a catalytically inactive B-subunit of Shiga toxin linked to peptide antigens, the antigens were delivered to the ER and resulted in presentation by major histocompatibility complex (MHC) molecules.[68-69] This approach has shown promise in mouse models for the development of adjuvant-free vacinations.[70] The ER-targeted delivery and release of the topoisomerase I inhibitor SN-38 was

demonstrated using the B-subunit of Shiga toxin, and toxicity was shown to be dependent on expression of the receptors Gb3/CD77.[71] Because Gb3/CD77 is overexpressed in certain cancer cells such as B-cell lymphomas[72-73] and colorectal carcinomas,[74-75] targeting of the ER through conjugation of agents to Shiga toxin has promise for the development of selective anticancer therapies.[76-77]

1.3.4 The Nucleus

The nucleus is a double-membrane enclosed organelle that houses the genomic DNA of eukaryotic cells. Exchange of material between the cytosol and the nucleus occurs through large protein-based (~120 MDa)[78] nuclear pore complexes (NPCs).[79] Small-molecules such as the common fluorescent DNA-binding compound Hoechst 33342 and DAPI (Figure 1.3 panel C)[80] can freely diffuse through NPCs and bind DNA in the nucleus.[81] The acridine dye ICR-191 (Figure 1.3 panel C), a mutagen commonly used in forward genetic studies, consists of an intercalating motif that targets the alkylating activity of the nitrogen mustard to DNA in the nucleus. Alkylating agents such as ICR-191 preferentially target guanines at the N7 position,[82] and are useful for creating frame-shift mutations in forward genetics studies.[83] Unlike small molecules, larger biomolecules such as proteins, RNA, and viral DNA rely on receptor-mediated transport through the NPC, mediated by nuclear localization and nuclear export peptides.[84]

For cellular transfection experiments, subcellular targeting of exogenous DNA to the nucleus is necessary. Viral transduction using common lentiviral[85-87]

or adenoviral[88-89] vectors overcomes this issue by utilizing viral pathways for cellular entry and delivery of the desired DNA to the nucleus. In order for genes of non-viral DNA to be expressed, the DNA must pass through several cellular barriers such as the plasma membrane or endocytic vesicles and then enter the nucleus through the NPC. To circumvent this issue of delivery of exogenous DNA into the nucleus, a variety of transfection agents have been developed. DNA packaged into cationic liposomes (lipoplexes) is frequently used for *in vitro* transfection, but has proved to be of limited use *in vivo*.[90] Additionally, DNA complexed with positively charged amine-containing polymers can be taken up by cells and reach the cytosol.[91] The mechanism of nuclear transport of uncomplexed cytosolic DNA remains unclear, but the addition nuclear-localization sequence peptides has been shown to enhance gene expression through more efficient nuclear targeting.[92-93]

1.3.5 Mitochondrial Function Enables Targeting by Small-Molecules

The mammalian mitochondrion is a complex organelle responsible for the majority of cellular respiration as well as regulating cellular apoptotic signaling (Figure 1.4). Mitochondria are composed of two phospholipid bilayer membranes termed the inner and outer membrane. The outer membrane separates the cytosol from the inter-membrane space and is permeable to solutes less than 5000 Da because of the presence of the membrane protein porin. The inner membrane is responsible for separating the inter-membrane space from the mitochondrial matrix and contains protein complexes involved in oxidative

phosphorylation. Oxidative phosphorylation (OXPHOS) establishes the mitochondrial membrane potential (ψ_m) across the inner membrane (-100 to -180 mV, depending on cell type) consisting of a gradient of protons.[94] This proton gradient is used by the mitochondrial F_1F_0-ATPase to drive synthesis of ATP from ADP. The mitochondrial electrochemical gradient drives the selective accumulation of some cationic small molecules into mitochondria.

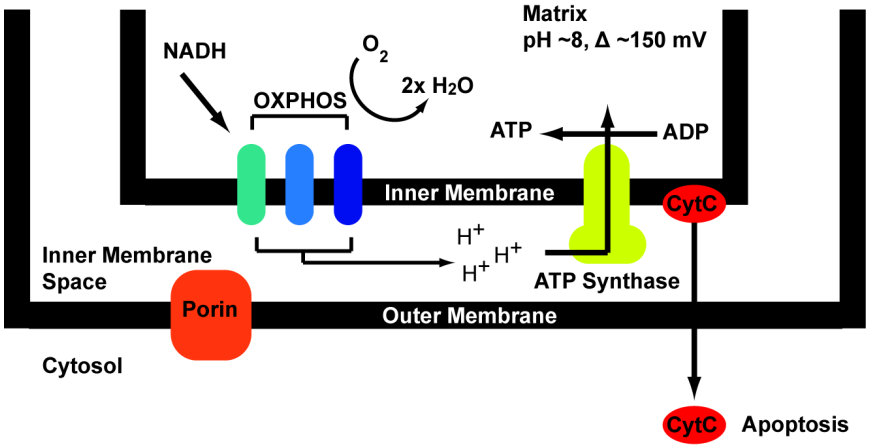

Figure 1.4. Functions of mitochondria of mammalian cells. Key features include the outer and inner membrane, the protein complexes of oxidative phosphorylation (OXPHOS), the electrochemical gradient of protons in the inner membrane space, the mitochondrial ATP synthase that uses the electrochemical gradient to produce ATP, and cytochrome C (CytC) that is released from the inner membrane space to the cytosol during apoptosis.

Lipophilic, cationic molecules accumulate in the matrix of mitochondria by diffusion down the negative electrochemical potential through the inner membrane (Figure 1.4).[94-96] This phenomena is exemplified by fluorophores (Figure 1.5 panel A) that selectively accumulate into polarized mitochondria such rhodamine esters, the commercial MitoTracker dyes (Life Technologies), and the hydrophobic rhodamine HR101.[97] HR101 was first synthesized in the Peterson laboratory, and some new studies of this compound are described in Chapter 4

of this dissertation (Figure 1.5, panel A). These types of fluorophores retain a permanent positive charge, but they are lipophilic enough to freely diffuse through the inner membrane and down the potential of the electrochemical gradient to accumulate in the mitochondrial matrix.

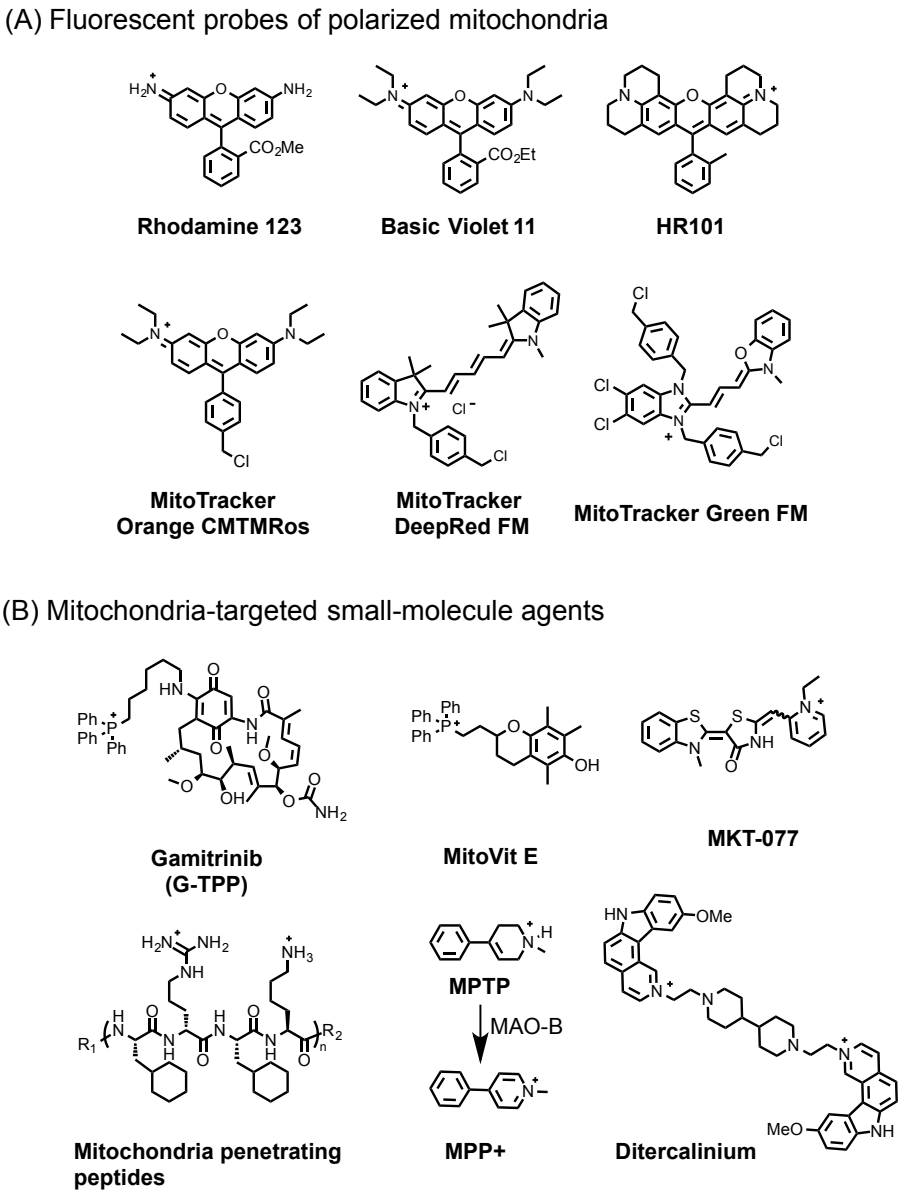

Figure 1.5. Panel A: Fluorescent probes of mitochondria employed in microscopy. The commercial MitoTracker dyes (Life Technologies) contain benzyl chloride motifs, which are useful for retention in the mitochondria following chemical fixation. Panel B: Mitochondria-targeted inhibitors of mitochondria-resident biomolecules.

Practitioners of medicinal chemistry and chemical biology can take advantage of the electrochemical gradient of mitochondria to design mitochondria-targeted agents. Examples of small molecules that accumulate in mitochondria can be found in Figure 1.5. Through the addition of lipophilic cationic groups, small molecules can accumulate in mitochondria to limit undesired interactions with non-mitochondrial targets. This approach was successfully used in targeting the HSP90 inhibitor geldanamycin to mitochondria to inhibit the mitochondria-specific isoform (TRAP-1) using guanidinium repeats or triphenylphosphonium cations (Figure 1.5 panel B).[98] Triphenylphosphonium salts[99-101] have also been used to target a number of antioxidants to the mitochondria such as MitoVit E (Figure 1.5, panel B). Cell-penetrating peptides (CPP), based on the sequence of HIV transactivator of transcription (TAT), have garnered interest for their ability to deliver normally cell-impermeable material into the cytosol.[102-103] However, traditional TAT-based CPP sequences do not penetrate the inner mitochondrial membrane.[104] New peptide sequences termed mitochondrial penetrating peptides (MPP, Figure 1.5 panel B), with alternating unnatural hydrophobic/cationic residues, have been shown to specifically deliver cargo through the plasma membrane and into mitochondria.[105]

Certain cationic small molecules can accumulate in mitochondria without engineered targeting motifs. MKT-077 is a rhodacyanine derivative (Figure 1.5 panel B) that inhibits the mitochondrial protein chaperone mortalin.[106] This compound has been shown[107] to exhibit a 4-fold selectively for targeting the cancer line CX-1 verses the non-cancer line CV-1. The cationic neurotoxin MPP+

(1-methyl-4-phenylpyridinium, Figure 1.5 panel B) is a useful agent for creating animal models of Parkinson's disease.[108-111] Animals treated with the metabolic precursor MPTP convert MPTP to MPP+ due to the activity of monoamine oxidase-B (MAO-B).[112] The dopamine transporter (DAT)[113] causes dopaminergic cells selectively to accumulate MPP+, leading to selective death of dopaminergic cells and severe Parkinson's symptoms. Mitochondria maintain multiple copies of a circular DNA of approximately 16.6 kB that is independent of genomic DNA.[114] Selective targeting of this mitochondrial DNA by the intercalator ditercalinium (Figure 1.5 panel B) can lead to selective loss of mitochondrial DNA verses genomic DNA.[115-117] The ability to direct biologically active small molecules to this important organelle through engineered linkers or an inherent permanent positive charge provides unique tools for controlling biological systems.

1.5 Outline of this Dissertation

Building on a renewed interest in phenotypic discovery methods, my research has focused on the design, synthesis, and biological evaluation of fluorescent small molecules that exhibit specific patterns of subcellular localization and studies of their downstream biological effects. Chapter 2 describes work redefining the mechanism of action of the potent anti-cancer/anti-viral compound AKT inhibitor-IV (AKTIV) as a specific inhibitor of mitochondrial function. This chapter describes investigations of the photophysical properties of AKTIV as well as the effects on cellular bioenergetics and mitochondrial morphology. Chapter 3 describes the synthesis and biological evaluation of novel

fluorinated, hydrophobic rhodols that specifically accumulate in the ER and can deliver a cytotoxic warhead to this organelle to selectively target the ERAD pathway. Chapter 4 describes the discovery of two fluorescent molecular probes that are active in the vertebrate model organism zebrafish (*Danio rerio*), including hydrophobic rhodamines targeted to mitochondria and acid-activated fluorophores that accumulate in acidic tissues. Chapter 5 describes an unrelated project involving the synthesis of novel dimers of cholesterol and *in vitro* stability analysis of liposomes that incorporate these compounds.

1.6 References

1. Swinney, D. C.; Anthony, J., How were new medicines discovered? *Nat. Rev. Drug Discov.* **2011,** *10* (7), 507-519.

2. Eder, J.; Sedrani, R.; Wiesmann, C., The discovery of first-in-class drugs: origins and evolution. *Nat. Rev. Drug Discov.* **2014,** *13* (8), 577-587.

3. Marks, P. A.; Breslow, R., Dimethyl sulfoxide to vorinostat: development of this histone deacetylase inhibitor as an anticancer drug. *Nat. Biotechnol.* **2007,** *25* (1), 84-90.

4. Cong, L.; Ran, F. A.; Cox, D.; Lin, S.; Barretto, R.; Habib, N.; Hsu, P. D.; Wu, X.; Jiang, W.; Marraffini, L. A.; Zhang, F., Multiplex Genome Engineering Using CRISPR/Cas Systems. *Science* **2013,** *339* (6121), 819-823.

5. Lang, P.; Yeow, K.; Nichols, A.; Scheer, A., Cellular imaging in drug discovery. *Nat. Rev. Drug Discov.* **2006,** *5* (4), 343-356.

6. Krutzik, P. O.; Nolan, G. P., Fluorescent cell barcoding in flow cytometry allows high-throughput drug screening and signaling profiling. *Nat. Methods* **2006,** *3* (5), 361-368.

7. Bickle, M., The beautiful cell: high-content screening in drug discovery. *Anal. Bioanal. Chem.* **2010,** *398* (1), 219-226.

8. Zanella, F.; Lorens, J. B.; Link, W., High content screening: seeing is believing. *Trends Biotechnol.* **2010,** *28* (5), 237-245.

9. Kau, T. R.; Schroeder, F.; Ramaswamy, S.; Wojciechowski, C. L.; Zhao, J. J.; Roberts, T. M.; Clardy, J.; Sellers, W. R.; Silver, P. A., A chemical genetic screen identifies inhibitors of regulated nuclear export of a Forkhead transcription factor in PTEN-deficient tumor cells. *Cancer Cell* **2003,** *4* (6), 463-476.

10. Anitei, M.; Chenna, R.; Czupalla, C.; Esner, M.; Christ, S.; Lenhard, S.; Korn, K.; Meyenhofer, F.; Bickle, M.; Zerial, M.; Hoflack, B., A high-throughput siRNA screen identifies genes that regulate mannose 6-phosphate receptor trafficking. *J. Cell Sci.* **2014,** *127* (23), 5079-5092.

11. Su, L. J.; Auluck, P. K.; Outeiro, T. F.; Yeger-Lotem, E.; Kritzer, J. A.; Tardiff, D. F.; Strathearn, K. E.; Liu, F.; Cao, S.; Hamamichi, S.; Hill, K. J.; Caldwell, K. A.; Bell, G. W.; Fraenkel, E.; Cooper, A. A.; Caldwell, G. A.; McCaffery, J. M.; Rochet, J.-C.; Lindquist, S., Compounds from an unbiased chemical screen reverse both ER-to-Golgi trafficking defects and mitochondrial dysfunction in Parkinson's disease models. *Dis. Model. Mech.* **2010,** *3* (3-4), 194-208.

12. Lee, Y. Q.; Goh, A. S. P.; Ch'ng, J. H.; Nosten, F. H.; Preiser, P. R.; Pervaiz, S.; Yadav, S. K.; Tan, K. S. W., A High-Content Phenotypic Screen Reveals the

Disruptive Potency of Quinacrine and 3′,4′-Dichlorobenzamil on the Digestive Vacuole of Plasmodium falciparum. *Antimicrob. Agents Chemother.* **2014,** *58* (1), 550-558.

13. Wang, D.; Wang, J.; Bonamy, G. M. C.; Meeusen, S.; Brusch, R. G.; Turk, C.; Yang, P.; Schultz, P. G., A Small Molecule Promotes Mitochondrial Fusion in Mammalian Cells. *Angew. Chem. Int. Ed.* **2012,** *51* (37), 9302-9305.

14. Peak, E.; Chalmers, I. W.; Hoffmann, K. F., Development and Validation of a Quantitative, High-Throughput, Fluorescent-Based Bioassay to Detect *Schistosoma* Viability. *PLOS Neglect. Trop. D.* **2010,** *4* (7), e759.

15. Gustafsdottir, S. M.; Ljosa, V.; Sokolnicki, K. L.; Anthony Wilson, J.; Walpita, D.; Kemp, M. M.; Petri Seiler, K.; Carrel, H. A.; Golub, T. R.; Schreiber, S. L.; Clemons, P. A.; Carpenter, A. E.; Shamji, A. F., Multiplex Cytological Profiling Assay to Measure Diverse Cellular States. *PLoS ONE* **2013,** *8* (12), e80999.

16. Arar, K.; Monsigny, M.; Mayer, R., Synthesis of oligonucleotide-peptide conjugates containing a KDEL signal sequence. *Tetrahedron Lett.* **1993,** *34* (50), 8087-8090.

17. Singh, P.; Tang, B. L.; Wong, S. H.; Hong, W., Transmembrane topology of the mammalian KDEL receptor. *Mol. Cell. Biol.* **1993,** *13* (10), 6435-6441.

18. Yamamoto, K.; Fujii, R.; Toyofuku, Y.; Saito, T.; Koseki, H.; Hsu, V. W.; Aoe, T., The KDEL receptor mediates a retrieval mechanism that contributes to quality control at the endoplasmic reticulum. *EMBO J.* **2001,** *20* (12), 3082-3091.

19. van Meer, G.; de Kroon, A. I. P. M., Lipid map of the mammalian cell. *J. Cell Sci.* **2011,** *124* (1), 5-8.

20. van Meer, G.; Voelker, D. R.; Feigenson, G. W., Membrane lipids: where they are and how they behave. *Nat. Rev. Mol. Cell Biol.* **2008,** *9* (2), 112-124.

21. Kohlwein, S. D.; Daum, G.; Schneiter, R.; Paltauf, F., Phospholipids: synthesis, sorting, subcellular traffic - the yeast approach. *Trends Cell Biol.* **1996,** *6* (7), 260-266.

22. Zheng, N.; Tsai, H. N.; Zhang, X.; Rosania, G. R., The Subcellular Distribution of Small Molecules: From Pharmacokinetics to Synthetic Biology. *Mol. Pharm.* **2011,** *8* (5), 1619-1628.

23. Zheng, N.; Tsai, H. N.; Zhang, X.; Shedden, K.; Rosania, G. R., The Subcellular Distribution of Small Molecules: A Meta-Analysis. *Mol. Pharm.* **2011,** *8* (5), 1611-1618.

24. Rajendran, L.; Udayar, V.; Goodger, Z. V., Lipid-anchored drugs for delivery into subcellular compartments. *Trends Pharmacol. Sci.* **2012,** *33* (4), 215-222.

25. Furuta, R. A.; Wild, C. T.; Weng, Y.; Weiss, C. D., Capture of an early fusion-active conformation of HIV-1 gp41. *Nat Struct Mol Biol* **1998,** *5* (4), 276-279.

26. Hildinger, M.; Dittmar, M. T.; Schult-Dietrich, P.; Fehse, B.; Schnierle, B. S.; Thaler, S.; Stiegler, G.; Welker, R.; von Laer, D., Membrane-Anchored Peptide Inhibits Human Immunodeficiency Virus Entry. *J. Virol.* **2001,** *75* (6), 3038-3042.

27. Ingallinella, P.; Bianchi, E.; Ladwa, N. A.; Wang, Y.-J.; Hrin, R.; Veneziano, M.; Bonelli, F.; Ketas, T. J.; Moore, J. P.; Miller, M. D.; Pessi, A., Addition of a cholesterol group to an HIV-1 peptide fusion inhibitor dramatically increases its antiviral potency. *Proc. Natl. Acad. Sci. U. S. A.* **2009,** *106* (14), 5801-5806.

28. Hollmann, A.; Matos, P. M.; Augusto, M. T.; Castanho, M. A. R. B.; Santos, N. C., Conjugation of Cholesterol to HIV-1 Fusion Inhibitor C34 Increases Peptide-Membrane Interactions Potentiating Its Action. *PLoS ONE* **2013,** *8* (4), e60302.

29. Gripon, P.; Cannie, I.; Urban, S., Efficient Inhibition of Hepatitis B Virus Infection by Acylated Peptides Derived from the Large Viral Surface Protein. *J. Virol.* **2005,** *79* (3), 1613-1622.

30. Rajendran, L.; Schneider, A.; Schlechtingen, G.; Weidlich, S.; Ries, J.; Braxmeier, T.; Schwille, P.; Schulz, J. B.; Schroeder, C.; Simons, M.; Jennings, G.; Knölker, H.-J.; Simons, K., Efficient Inhibition of the Alzheimer's Disease β-Secretase by Membrane Targeting. *Science* **2008,** *320* (5875), 520-523.

31. O'Callaghan, K.; Kuliopulos, A.; Covic, L., Turning Receptors On and Off with Intracellular Pepducins: New Insights into G-protein-coupled Receptor Drug Development. *J. Biol. Chem.* **2012,** *287* (16), 12787-12796.

32. Boullier, J. A.; Brown, B. A.; Bush, J. C.; Barisas, B. G., Lateral Mobility of a Lipid Analog in the Membrane of Irreversible Sickle Erythrocytes. *Biochim. Biophys. Acta* **1986,** *856* (2), 301-309.

33. Parish, C. R., Fluorescent dyes for lymphocyte migration and proliferation studies. *Immunol. Cell Biol.* **1999,** *77* (6), 499-508.

34. Demaurex, N., pH Homeostasis of Cellular Organelles. *News Physiol. Sci.* **2002,** *17* (1), 1-5.

35. Altan, N.; Chen, Y.; Schindler, M.; Simon, S. M., Defective acidification in human breast tumor cells and implications for chemotherapy. *J. Exp. Med.* **1998,** *187* (10), 1583-1598.

36. Ndolo, R. A.; Jacobs, D. T.; Forrest, M. L.; Krise, J. P., Intracellular Distribution-based Anticancer Drug Targeting: Exploiting a Lysosomal Acidification Defect Associated with Cancer Cells. *Mol. Cell Pharmacol.* **2010,** *2* (4), 131-136.

37. Kokkonen, N.; Rivinoja, A.; Kauppila, A.; Suokas, M.; Kellokumpu, I.; Kellokumpu, S., Defective acidification of intracellular organelles results in aberrant secretion of cathepsin D in cancer cells. *J. Biol. Chem.* **2004,** *279* (38), 39982-8.

38. Gong, Y. P.; Duvvuri, M.; Krise, J. P., Separate roles for the Golgi apparatus and lysosomes in the sequestration of drugs in the multidrug-resistant human leukemic cell line HL-60. *J. Biol. Chem.* **2003,** *278* (50), 50234-50239.

39. Wibo, M.; Poole, B., PROTEIN DEGRADATION IN CULTURED CELLS: II. The Uptake of Chloroquine by Rat Fibroblasts and the Inhibition of Cellular Protein Degradation and Cathepsin B1. *J. Cell Biol.* **1974,** *63* (2), 430-440.

40. Goldman, S. D. B.; Funk, R. S.; Rajewski, R. A.; Krise, J. P., Mechanisms of amine accumulation in, and egress from, lysosomes. *Bioanalysis* **2009,** *1* (8), 1445-1459.

41. Ndolo, R. A.; Luan, Y.; Duan, S.; Forrest, M. L.; Krise, J. P., Lysosomotropic Properties of Weakly Basic Anticancer Agents Promote Cancer Cell Selectivity In Vitro. *PLoS ONE* **2012,** *7* (11), e49366.

42. Sanli, S.; Altun, Y.; Guven, G., Solvent Effects on pKa Values of Some Anticancer Agents in Acetonitrile–Water Binary Mixtures. *Journal of Chemical & Engineering Data* **2014,** *59* (12), 4015-4020.

43. Schuurhuis, G. J.; van Heijningen, T. H. M.; Cervantes, A.; Pinedo, H. M.; de Lange, J. H. M.; Keizer, H. G.; Broxterman, H. J.; Baak, J. P. A.; Lankelma, J., Changes in subcellular doxorubicin distribution and cellular accumulation alone can largely account for doxorubicin resistance in SW-1573 lung cancer and MCF-7 breast cancer multidrug resistant tumour cells. *Br. J. Cancer* **1993,** *68* (5), 898-908.

44. Lambert, J. M., Drug-conjugated antibodies for the treatment of cancer. *Br. J. Clin. Pharmacol.* **2013,** *76* (2), 248-262.

45. Bouchard, H.; Viskov, C.; Garcia-Echeverria, C., Antibody–drug conjugates—A new wave of cancer drugs. *Bioorg. Med. Chem. Lett.* **2014,** *24* (23), 5357-5363.

46. Verma, S.; Miles, D.; Gianni, L.; Krop, I. E.; Welslau, M.; Baselga, J.; Pegram, M.; Oh, D.-Y.; Diéras, V.; Guardino, E.; Fang, L.; Lu, M. W.; Olsen, S.; Blackwell, K., Trastuzumab Emtansine for HER2-Positive Advanced Breast Cancer. *N. Engl. J. Med.* **2012,** *367* (19), 1783-1791.

47. Barok, M.; Joensuu, H.; Isola, J., Trastuzumab emtansine: mechanisms of action and drug resistance. *Breast Cancer Res* **2014,** *16* (2).

48. Younes, A.; Yasothan, U.; Kirkpatrick, P., Brentuximab vedotin. *Nat. Rev. Drug Discov.* **2012,** *11* (1), 19-20.

49. Doronina, S. O.; Toki, B. E.; Torgov, M. Y.; Mendelsohn, B. A.; Cerveny, C. G.; Chace, D. F.; DeBlanc, R. L.; Gearing, R. P.; Bovee, T. D.; Siegall, C. B.; Francisco, J. A.; Wahl, A. F.; Meyer, D. L.; Senter, P. D., Development of potent monoclonal antibody auristatin conjugates for cancer therapy. *Nat. Biotechnol.* **2003,** *21* (7), 778-784.

50. Francisco, J. A.; Cerveny, C. G.; Meyer, D. L.; Mixan, B. J.; Klussman, K.; Chace, D. F.; Rejniak, S. X.; Gordon, K. A.; DeBlanc, R.; Toki, B. E.; Law, C.-L.; Doronina, S. O.; Siegall, C. B.; Senter, P. D.; Wahl, A. F., cAC10-vcMMAE, an anti-CD30–monomethyl auristatin E conjugate with potent and selective antitumor activity. *Blood* **2003,** *102* (4), 1458-1465.

51. Dubowchik, G. M.; Firestone, R. A.; Padilla, L.; Willner, D.; Hofstead, S. J.; Mosure, K.; Knipe, J. O.; Lasch, S. J.; Trail, P. A., Cathepsin B-Labile Dipeptide Linkers for Lysosomal Release of Doxorubicin from Internalizing Immunoconjugates: Model Studies of Enzymatic Drug Release and Antigen-Specific In Vitro Anticancer Activity. *Bioconjug. Chem.* **2002,** *13* (4), 855-869.

52. Mullard, A., Maturing antibody-drug conjugate pipeline hits 30. *Nat Rev Drug Discov* **2013,** *12* (5), 329-332.

53. Hymel, D.; Peterson, B. R., Synthetic cell surface receptors for delivery of therapeutics and probes. *Adv. Drug Del. Rev.* **2012,** *64* (9), 797-810.

54. Hussey, S. L.; He, E. F.; Peterson, B. R., A synthetic membrane-anchored antigen efficiently promotes uptake of antifluorescein antibodies and associated protein a by mammalian cells. *J. Am. Chem. Soc.* **2001,** *123* (50), 12712-12713.

55. Mottram, L. F.; Boonyarattanakalin, S.; Kovel, R. E.; Peterson, B. R., The Pennsylvania Green Fluorophore: A Hybrid of Oregon Green and Tokyo Green for the Construction of Hydrophobic and pH-Insensitive Molecular Probes. *Org. Lett.* **2006,** *8* (4), 581-584.

56. Boonyarattanakalin, S.; Martin, S. E.; Sun, Q.; Peterson, B. R., A synthetic mimic of human Fc receptors: Defined chemical modification of cell surfaces enables efficient endocytic uptake of human immunoglobulin-G. *J. Am. Chem. Soc.* **2006,** *128* (35), 11463-11470.

57. Boonyarattanakalin, S.; Hu, J. F.; Dykstra-Rummel, S. A.; August, A.; Peterson, B. R., Endocytic delivery of vancomycin mediated by a synthetic cell surface receptor: Rescue of bacterially infected mammalian cells and tissue targeting in vivo. *J. Am. Chem. Soc.* **2007,** *129* (2), 268-269.

58. Sun, Q.; Cai, S.; Peterson, B. R., Selective disruption of early/recycling endosomes: Release of disulfide-linked cargo mediated by a N-alkyl-3 beta-cholesterylamine-capped peptide. *J. Am. Chem. Soc.* **2008,** *130* (31), 10064-10065.

59. Hymel, D.; Cai, S.; Sun, Q.; Henkhaus, R. S.; Perera, C.; Peterson, B. R., Fluorescent Mimics of Cholesterol that Rapidly Bind Surfaces of Living Mammalian Cells. *Chem. Commun.* **2015**.

60. Colston, J.; Horobin, R. W.; Rashid-Doubell, F.; Pediani, J.; Johal, K. K., Why fluorescent probes for endoplasmic reticulum are selective: an experimental and QSAR-modelling study. *Biotech. Histochem.* **2003,** *78* (6), 323-332.

61. Cole, L.; Davies, D.; Hyde, J.; Ashford, A. E., ER-Tracker dye and BODIPY-brefeldin A differentiate the endoplasmic reticulum and Golgi bodies from the tubular-vacuole system in living hyphae of Pisolithus tinctorius. *J. Microsc.* **2000,** *197* (3), 239-249.

62. Ma, W. F.; Chen, H. Y.; Du, J.; Tan, Y.; Cai, S. H., A novel recombinant protein TAT-GFP-KDEL with dual-function of penetrating cell membrane and locating at endoplasm reticulum. *J. Drug Target.* **2009,** *17* (4), 329-333.

63. Sandvig, K.; van Deurs, B., Transport of protein toxins into cells: pathways used by ricin, cholera toxin and Shiga toxin. *FEBS Lett.* **2002,** *529* (1), 49-53.

64. Falnes, P. Ø.; Sandvig, K., Penetration of protein toxins into cells. *Curr. Opin. Cell Biol.* **2000,** *12* (4), 407-413.

65. Sandvig, K.; Skotland, T.; van Deurs, B.; Klokk, T., Retrograde transport of protein toxins through the Golgi apparatus. *Histochem. Cell Biol.* **2013,** *140* (3), 317-326.

66. Okuda, T.; Tokuda, N.; Numata, S.-i.; Ito, M.; Ohta, M.; Kawamura, K.; Wiels, J.; Urano, T.; Tajima, O.; Furukawa, K.; Furukawa, K., Targeted Disruption of Gb3/CD77 Synthase Gene Resulted in the Complete Deletion of Globo-series Glycosphingolipids and Loss of Sensitivity to Verotoxins. *J. Biol. Chem.* **2006,** *281* (15), 10230-10235.

67. Johannes, L.; Decaudin, D., Protein toxins: intracellular trafficking for targeted therapy. *Gene Ther.* **2005,** *12* (18), 1360-1368.

68. Lee, R.-S.; Tartour, E.; Van der Bruggen, P.; Vantomme, V.; Joyeux, I.; Goud, B.; Fridman, W. H.; Johannes, L., Major histocompatibility complex class I

presentation of exogenous soluble tumor antigen fused to the B-fragment of Shiga toxin. *Eur. J. Immunol.* **1998,** *28* (9), 2726-2737.

69. Haicheur, N.; Bismuth, E.; Bosset, S.; Adotevi, O.; Warnier, G.; Lacabanne, V.; Regnault, A.; Desaymard, C.; Amigorena, S.; Ricciardi-Castagnoli, P.; Goud, B.; Fridman, W. H.; Johannes, L.; Tartour, E., The B Subunit of Shiga Toxin Fused to a Tumor Antigen Elicits CTL and Targets Dendritic Cells to Allow MHC Class I-Restricted Presentation of Peptides Derived from Exogenous Antigens. *J. Immunol.* **2000,** *165* (6), 3301-3308.

70. Haicheur, N.; Benchetrit, F.; Amessou, M.; Leclerc, C.; Falguières, T.; Fayolle, C.; Bismuth, E.; Fridman, W. H.; Johannes, L.; Tartour, E., The B subunit of Shiga toxin coupled to full‐size antigenic protein elicits humoral and cell‐mediated immune responses associated with a Th1‐dominant polarization. *Int. Immunol.* **2003,** *15* (10), 1161-1171.

71. El Alaoui, A.; Schmidt, F.; Amessou, M.; Sarr, M.; Decaudin, D.; Florent, J.-C.; Johannes, L., Shiga Toxin-Mediated Retrograde Delivery of a Topoisomerase I Inhibitor Prodrug. *Angew. Chem. Int. Ed.* **2007,** *46* (34), 6469-6472.

72. LaCasse, E. C.; Bray, M. R.; Patterson, B.; Lim, W.-M.; Perampalam, S.; Radvanyi, L. G.; Keating, A.; Stewart, A. K.; Buckstein, R.; Sandhu, J. S.; Miller, N.; Banerjee, D.; Singh, D.; Belch, A. R.; Pilarski, L. M.; Gariépy, J., Shiga-Like Toxin-1 Receptor on Human Breast Cancer, Lymphoma, and Myeloma and Absence From CD34+ Hematopoietic Stem Cells: Implications for Ex Vivo Tumor Purging and Autologous Stem Cell Transplantation. *Blood* **1999,** *94* (8), 2901-2910.

73. Furukawa, K.; Yokoyama, K.; Sato, T.; Wiels, J.; Hirayama, Y.; Ohta, M.; Furukawa, K., Expression of the Gb3/CD77 Synthase Gene in Megakaryoblastic Leukemia Cells: IMPLICATION IN THE SENSITIVITY TO VEROTOXINS. *J. Biol. Chem.* **2002,** *277* (13), 11247-11254.

74. Falguières, T.; Maak, M.; von Weyhern, C.; Sarr, M.; Sastre, X.; Poupon, M.-F.; Robine, S.; Johannes, L.; Janssen, K.-P., Human colorectal tumors and metastases express Gb3 and can be targeted by an intestinal pathogen-based delivery tool. *Mol. Cancer Ther.* **2008,** *7* (8), 2498-2508.

75. Distler, U.; Souady, J.; Hülsewig, M.; Drmić-Hofman, I.; Haier, J.; Friedrich, A. W.; Karch, H.; Senninger, N.; Dreisewerd, K.; Berkenkamp, S.; Schmidt, M. A.; Peter-Katalinić, J.; Müthing, J., Shiga Toxin Receptor Gb3Cer/CD77: Tumor-Association and Promising Therapeutic Target in Pancreas and Colon Cancer. *PLoS ONE* **2009,** *4* (8), e6813.

76. Viel, T.; Dransart, E.; Nemati, F.; Henry, E.; Theze, B.; Decaudin, D.; Lewandowski, D.; Boisgard, R.; Johannes, L.; Tavitian, B., In Vivo Tumor Targeting by the B-Subunit of Shiga Toxin. *Mol. Imaging* **2008,** *7* (6), 239-247.

77. Engedal, N.; Skotland, T.; Torgersen, M. L.; Sandvig, K., Shiga toxin and its use in targeted cancer therapy and imaging. *Microbial Biotechnology* **2011,** *4* (1), 32-46.

78. Reichelt, R.; Holzenburg, A.; Buhle, E. L.; Jarnik, M.; Engel, A.; Aebi, U., Correlation between structure and mass distribution of the nuclear pore complex and of distinct pore complex components. *J. Cell Biol.* **1990,** *110* (4), 883-894.

79. Bagley, S.; Goldberg, M. W.; Cronshaw, J. M.; Rutherford, S. A.; Allen, T. D., The nuclear pore complex. *J. Cell Sci.* **2000,** *113* (22), 3885-3886.

80. Latt, S. A.; Stetten, G., Spectral studies on 33258 Hoechst and related bisbenzimidazole dyes useful for fluorescent detection of deoxyribonucleic acid synthesis. *J. Histochem. Cytochem.* **1976,** *24* (1), 24-33.

81. Olive, P. L.; Chaplin, D. J.; Durand, R. E., Pharmacokinetics, binding and distribution of Hoechst 33342 in spheroids and murine tumours. *Br. J. Cancer* **1985,** *52* (5), 739-746.

82. Sahasrabudhe, S. R.; Luo, X.; Humayun, M. Z., Specificity of base substitutions induced by the acridine mutagen ICR-191: mispairing by guanine N7 adducts as a mutagenic mechanism. *Genetics* **1991,** *129* (4), 981-9.

83. Hoffmann, G. R.; Calciano, M. A.; Lawless, B. M.; Mahoney, K. M., Frameshift mutations induced by three classes of acridines in the lacZ reversion assay in Escherichia coli: Potency of responses and relationship to slipped mispairing models. *Environ. Mol. Mutagen.* **2003,** *42* (2), 111-121.

84. Mohr, D.; Frey, S.; Fischer, T.; Güttler, T.; Görlich, D., *Characterisation of the passive permeability barrier of nuclear pore complexes*. 2009; Vol. 28, p 2541-2553.

85. Bos, T. J.; De Bruyne, E.; Heirman, C.; Vanderkerken, K., In search of the most suitable lentiviral shRNA system. *Curr. Gene Ther.* **2009,** *9* (3), 192-211.

86. Delenda, C., Lentiviral vectors: optimization of packaging, transduction and gene expression. *The Journal of Gene Medicine* **2004,** *6* (S1), S125-S138.

87. Levine, B. L.; Humeau, L. M.; Boyer, J.; MacGregor, R.-R.; Rebello, T.; Lu, X.; Binder, G. K.; Slepushkin, V.; Lemiale, F.; Mascola, J. R.; Bushman, F. D.; Dropulic, B.; June, C. H., Gene transfer in humans using a conditionally replicating lentiviral vector. *Proc. Natl. Acad. Sci. U. S. A.* **2006,** *103* (46), 17372-17377.

88. Mancheno-Corvo, P.; Martin-Duque, P., Viral gene therapy. *Clin. Transl. Oncol.* **2006,** *8* (12), 858-867.

89. McLaughlin, S. K.; Collis, P.; Hermonat, P. L.; Muzyczka, N., Adeno-associated virus general transduction vectors: analysis of proviral structures. *J. Virol.* **1988,** *62* (6), 1963-1973.

90. Li, S.; Huang, L., Nonviral gene therapy: promises and challenges. *Gene Ther.* **2000,** *7* (1), 31-34.

91. Goula, D.; Benoist, C.; Mantero, S.; Merlo, G.; Levi, G.; Demeneix, B. A., Polyethylenimine-based intravenous delivery of transgenes to mouse lung. *Gene Ther.* **1998,** *5* (9), 1291-1295.

92. Zanta, M. A.; Belguise-Valladier, P.; Behr, J. P., Gene delivery: A single nuclear localization signal peptide is sufficient to carry DNA to the cell nucleus. *Proc. Natl. Acad. Sci. U. S. A.* **1999,** *96* (1), 91-96.

93. Subramanian, A.; Ranganathan, P.; Diamond, S. L., Nuclear targeting peptide scaffolds for lipofection of nondividing mammalian cells. *Nat Biotech* **1999,** *17* (9), 873-877.

94. Modica-Napolitano, J. S.; Aprille, J. R., Basis for the Selective Cytotoxicity of Rhodamine 123. *Cancer Res.* **1987,** *47* (16), 4361-4365.

95. Lampidis, T. J.; Bernal, S. D.; Summerhayes, I. C.; Chen, L. B., Selective Toxicity of Rhodamine 123 in Carcinoma Cells in Vitro. *Cancer Res.* **1983,** *43* (2), 716-720.

96. Modica-Napolitano, J. S.; Weiss, M. J.; Chen, L. B.; Aprille, J. R., Rhodamine 123 inhibits bioenergetic function in isolated rat liver mitochondria. *Biochem. Biophys. Res. Commun.* **1984,** *118* (3), 717-23.

97. Mottram, L. F.; Forbes, S.; Ackley, B. D.; Peterson, B. R., Hydrophobic analogues of rhodamine B and rhodamine 101: potent fluorescent probes of mitochondria in living C. elegans. *Beilstein J. Org. Chem.* **2012,** *8*, 2156-2165.

98. Kang, B. H.; Plescia, J.; Song, H. Y.; Meli, M.; Colombo, G.; Beebe, K.; Scroggins, B.; Neckers, L.; Altieri, D. C., Combinatorial drug design targeting multiple cancer signaling networks controlled by mitochondrial Hsp90. *J. Clin. Invest.* **2009,** *119* (3), 454-464.

99. Smith, R. A. J.; Porteous, C. M.; Gane, A. M.; Murphy, M. P., Delivery of bioactive molecules to mitochondria in vivo. *Proc. Natl. Acad. Sci. U. S. A.* **2003,** *100* (9), 5407-5412.

100. Millard, M.; Gallagher, J. D.; Olenyuk, B. Z.; Neamati, N., A Selective Mitochondrial-Targeted Chlorambucil with Remarkable Cytotoxicity in Breast and Pancreatic Cancers. *J. Med. Chem.* **2013,** *56* (22), 9170-9179.

101. Han, M.; Vakili, M. R.; Soleymani Abyaneh, H.; Molavi, O.; Lai, R.; Lavasanifar, A., Mitochondrial Delivery of Doxorubicin via Triphenylphosphine Modification for Overcoming Drug Resistance in MDA-MB-435/DOX Cells. *Mol. Pharm.* **2014,** *11* (8), 2640-2649.

102. Bechara, C.; Sagan, S., Cell-penetrating peptides: 20 years later, where do we stand? *FEBS Lett.* **2013,** *587* (12), 1693-1702.

103. Copolovici, D. M.; Langel, K.; Eriste, E.; Langel, Ü., Cell-Penetrating Peptides: Design, Synthesis, and Applications. *ACS Nano* **2014,** *8* (3), 1972-1994.

104. Gambling, D.; Hughes, T.; Martin, G.; Horton, W.; Manvelian, G.; Group, f. t. S.-D. E. S., A Comparison of Depodur™, a Novel, Single-Dose Extended-Release Epidural Morphine, with Standard Epidural Morphine for Pain Relief After Lower Abdominal Surgery. *Anesth. Analg.* **2005,** *100* (4), 1065-1074.

105. Horton, K. L.; Stewart, K. M.; Fonseca, S. B.; Guo, Q.; Kelley, S. O., Mitochondria-penetrating peptides. *Chem. Biol.* **2008,** *15* (4), 375-382.

106. Wadhwa, R.; Sugihara, T.; Yoshida, A.; Nomura, H.; Reddel, R. R.; Simpson, R.; Maruta, H.; Kaul, S. C., Selective Toxicity of MKT-077 to Cancer Cells Is Mediated by Its Binding to the hsp70 Family Protein mot-2 and Reactivation of p53 Function. *Cancer Res.* **2000,** *60* (24), 6818-6821.

107. Modica-Napolitano, J. S.; Koya, K.; Weisberg, E.; Brunelli, B. T.; Li, Y.; Chen, L. B., Selective Damage to Carcinoma Mitochondria by the Rhodacyanine MKT-077. *Cancer Res.* **1996,** *56* (3), 544-550.

108. Blandini, F.; Armentero, M. T., Animal models of Parkinson's disease. *FEBS J.* **2012,** *279* (7), 1156-66.

109. Blesa, J.; Phani, S.; Jackson-Lewis, V.; Przedborski, S., Classic and New Animal Models of Parkinson's Disease. *J. Biomed. Biotechnol.* **2012**.

110. Duty, S.; Jenner, P., Animal models of Parkinson's disease: a source of novel treatments and clues to the cause of the disease. *Br. J. Pharmacol.* **2011,** *164* (4), 1357-1391.

111. Nass, R.; Hall, D. H.; Miller, D. M.; Blakely, R. D., Neurotoxin-induced degeneration of dopamine neurons in Caenorhabditis elegans. *Proc. Natl. Acad. Sci. U. S. A.* **2002,** *99* (5), 3264-3269.

112. Gessner, W.; Brossi, A.; Bembenek, M. E.; Fritz, R. R.; Abell, C. W., Studies on the mechanism of MPTP oxidation by human liver monoamine oxidase B. *FEBS Lett.* **1986,** *199* (1), 100-102.

113. Kitayama, S.; Mitsuhata, C.; Davis, S.; Wang, J.-B.; Sato, T.; Morita, K.; Uhl, G. R.; Dohi, T., MPP+ toxicity and plasma membrane dopamine transporter: study using cell lines expressing the wild-type and mutant rat dopamine transporters. *Biochimica et Biophysica Acta (BBA) - Molecular Cell Research* **1998,** *1404* (3), 305-313.

114. Taanman, J.-W., The mitochondrial genome: structure, transcription, translation and replication. *Biochimica et Biophysica Acta (BBA) - Bioenergetics* **1999,** *1410* (2), 103-123.

115. Gao, Q.; Williams, L. D.; Egli, M.; Rabinovich, D.; Chen, S. L.; Quigley, G. J.; Rich, A., Drug-Induced DNA-Repair - X-Ray Structure of a DNA-Ditercalinium Complex. *Proc. Natl. Acad. Sci. U. S. A.* **1991,** *88* (6), 2422-2426.

116. Okamaoto, M.; Ohsato, T.; Nakada, K.; Isobe, K.; Spelbrink, J.; Hayashi, J.-I.; Hamasaki, N.; Kang, D., Ditercalinium chloride, a pro-anticancer drug,

intimately associates with mammalian mitochondrial DNA and inhibits its replication. *Curr. Genet.* **2003,** *43* (5), 364-370.

117. Segalbendirdjian, E.; Coulaud, D.; Roques, B. P.; Lepecq, J. B., Selective Loss of Mitochondrial-DNA after Treatment of Cells with Ditercalinium (Nsc-335153), an Antitumor Bis-Intercalating Agent. *Cancer Res.* **1988,** *48* (17), 4982-4992.

Chapter 2

The Anticancer/Antiviral Agent Akt Inhibitor-IV Massively Accumulates in Mitochondria and Potently Disrupts Cellular Bioenergetics

2.1 Introduction

Akt inhibitor-IV (ChemBridge 5233705, CAS 681281-88-9, AKTIV, Figure 2.1 Panel A), a cationic benzimidazole derivative, exhibits a wide range of biological activities. This small molecule was first identified in a chemical genetic screen as an inhibitor of nuclear export of the FOXO1a protein.[1] In U2OS cancer cells, low concentrations of AKTIV (IC_{50} = 0.625 μM) blocked nuclear export of this protein with concomitant inhibitory effects on cellular proliferation (IC_{50} < 1.25 μM).[1] At a higher concentration of 10 μM, phosphorylation of the serine-threonine kinase Akt (protein kinase B) on residues Ser473 and Thr308 was suppressed. Because phosphorylation of FOXO1a by Akt promotes nuclear export, AKTIV was initially proposed to block nuclear export of FOXO1a by inhibiting a kinase in the PI3-kinase (PI3K) / Akt pathway.[1] Other studies of AKTIV confirmed its potent cytotoxic activity (typical IC_{50} values < 2 μM) against a wide range of cancer and other cell lines.[2-7] Although some inhibitors of the PI3K / Akt pathway show promise as anticancer agents,[8-9] more recent studies[10] of AKTIV concluded that this compound does not directly block the activity of any known kinases within this signaling cascade. Moreover, this compound paradoxically increases phosphorylation of Akt when added to BHK-21 cells at 1-2 μM.[10] High concentrations

(10 μM) of this small molecule also activate the unfolded protein response (UPR) and trigger cellular blebbing and apoptosis in HEK293T cells.[11]

In addition to its major effects on cellular proliferation, AKTIV exhibits broad-spectrum antiviral activity. Viruses inhibited by this compound include vesicular stomatitis virus (VSV), respiratory syncytial virus, vaccinia virus in infected BHK-21 cells,[10] and parainfluenzavirus-5 (PIV5) in infected HeLa cells.[12-14] However, the mechanistic basis for this activity is not well understood, the importance of the PI3K / Akt pathway in viral replication is controversial, and AKTIV has been reported to block the replication of negative-strand RNA viruses through an Akt-independent mechanism.[10] The antiviral effects of AKTIV also appear to be independent of its cytotoxic effects on host cells.

To probe the structural features associated with this highly biologically active scaffold, we previously reported the synthesis of AKTIV and a collection of analogues.[13] We demonstrated that this compound and some analogues exhibit selective anticancer activity against human HeLa carcinoma cells when compared with normal human bronchial/tracheal epithelial (NBHE) cells. We further confirmed its antiviral effects against recombinant parainfluenzavirus-5 in HeLa cells. Although the photophysical properties of these compounds have not been previously characterized, during our prior synthesis of analogues of AKTIV, we noticed that some of these compounds were qualitatively fluorescent in solution, and this observation led to the hypothesis that studies of the intrinsic fluorescence of Akt inhibitor-IV, like other fluorescent molecular probes,[15-16] might reveal its biological mechanism of action. We report here an investigation of the mechanism of action of AKTIV that exploits the intrinsic fluorescence

of this small molecule. This approach revealed that AKTIV rapidly accumulates to high levels in mitochondria of treated mammalian cells and profoundly affects the morphology of these organelles. Treatment of cancer cell lines with AKTIV rapidly triggers extensive mitochondrial dysfunction, and this new understanding of its mechanism of action explains many of the diverse biological activities of this potent small molecule.

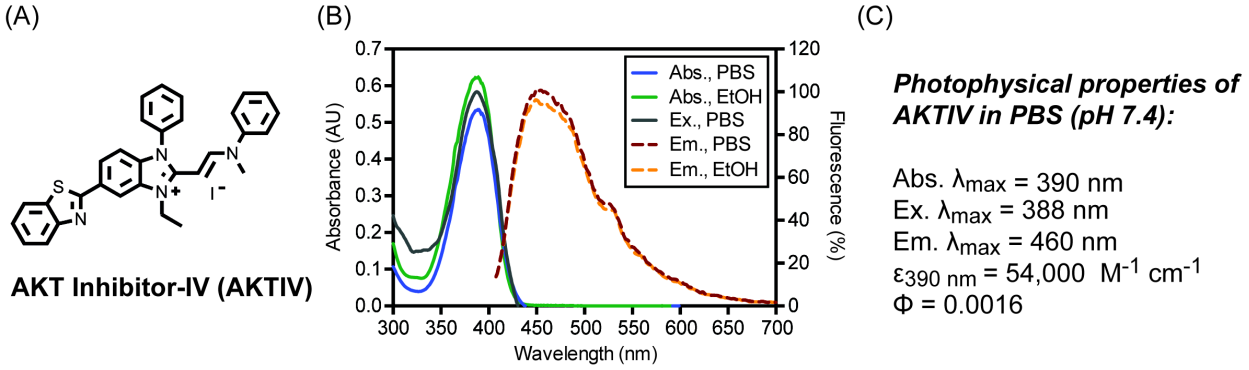

Figure 2.1. Panel A: Chemical structure of AKTIV. Panel B: The absorbance (Abs.), excitation (Ex.), and fluorescence emission (Em.) spectra of AKTIV obtained in PBS (pH 7.4) and ethanol. Panel C: Values for the extinction coefficient (ε), and quantum yield (Φ) in PBS of AKTIV.

2.2 Photophysical Properties of AKTIV

During our prior studies of AKTIV,[13] we observed that dilute solutions of this compound are fluorescent when irradiated with ultraviolet light. To examine the photophysical properties of this compound in detail, we obtained absorbance, fluorescence excitation, and fluorescence emission spectra in aqueous buffer (PBS, pH 7.4) and ethanol. As shown in Figure 2.1 (Panel B), the spectral properties of AKTIV in both of these solvents were very similar, indicating that unlike some common fluorophores, such as dansyl, NBD, and certain coumarins,[17] its fluorescence properties are not highly sensitive to environmental conditions. In these solvents, AKTIV was found

to strongly absorb in the UV–violet region (absorbance $\lambda_{max,\ PBS}$ = 390 nm), with a relatively high extinction coefficient ($\varepsilon_{390\ nm}$) in PBS of 54,000 $M^{-1}\,cm^{-1}$. Upon excitation with UV ($\lambda_{max,\ ex.}$ = 388 nm, Figure 2), AKTIV emitted blue fluorescence with λ_{max} = 460 nm (Figure 2.1, panel B). However, the quantum yield (Φ) of AKTIV was only 0.0016, as determined by comparison with the integrated emission of the coumarin-derived fluorophore Pacific Blue (Φ= 0.75, $\lambda_{max,abs.}$ = 405 nm, $\lambda_{max,\ em.}$ = 450 nm).[18,19] When the brightness of these two fluorophores was compared, defined as the product of the quantum yield and extinction coefficient, AKTIV was 260-fold less bright than Pacific Blue ($\varepsilon_{405\ nm}$ = 30,000 $M^{-1}\,cm^{-1}$).[19] However, the relatively close match of the maximal excitation wavelength (388 nm) of AKTIV to the 405 nm laser line of many confocal laser scanning microscopes and flow cytometers led us to conclude that the intrinsic fluorescence of this compound might enable imaging and analysis of its subcellular distribution in living mammalian cells.

2.3 Confocal Laser Scanning Microscopy of Cells Treated With AKTIV

To investigate the utility of AKTIV as a fluorescent probe, HeLa cervical carcinoma cells were briefly treated (5 min, no wash step) with a low concentration (1 μM) of this compound. Imaging by confocal laser scanning microscopy, with excitation at 405 nm, revealed fluorescence in defined subcellular structures of treated cells (Figure 2.2, panel A). These structures exhibited a tubular morphology and were identified as mitochondria by co-staining with the spectrally orthogonal probe MitoTracker DeepRed. To examine if autofluorescence of NADH[20] in these organelles contributed to this signal, control experiments in the absence of AKTIV were used to

verify that the fluorescence observed in mitochondria upon excitation at 405 nm was exclusively derived from this compound (Figure 2.2, panel B). Because of its low quantum yield, the visualization of AKTIV in mitochondria of treated HeLa cells suggested that this compound accumulates to high levels in these organelles.

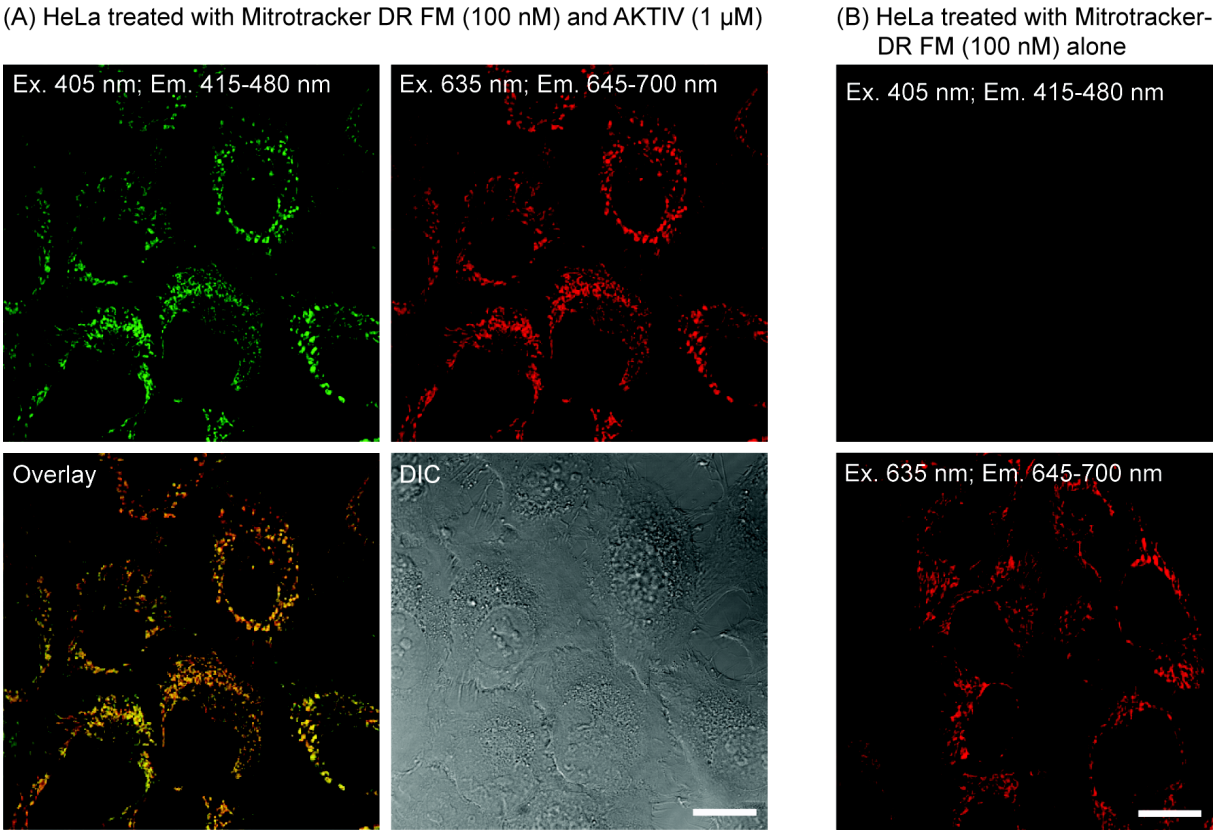

Figure 2.2. Confocal laser scanning and differential interference contrast (DIC) micrographs of living HeLa cells. Cells in Panel A were treated with MitoTracker DR (100 nM) and AKTIV (1 μM) for 5 min. Cells in Panel B were treated with MitoTracker DR (100 nM, 5 min) alone to confirm the absence of autofluorescence. Scale bar = 20 μm.

2.4 Quantification of AKTIV in Mitochondria

As shown in Figure 2.3, AKTIV shows structural similarities to MitoTracker Deep Red-FM,[21] JC-1,[22] rhodamine 123,[23], MKT-007,[24-25] and F16.[26] These types of lipophilic delocalized cations are known to accumulate in mitochondria[27-28] and are driven into this organelle by the high negative electrochemical potential that exists across the inner mitochondrial membrane (typically –120 to –180 mV, depending on cell type).[29-32]

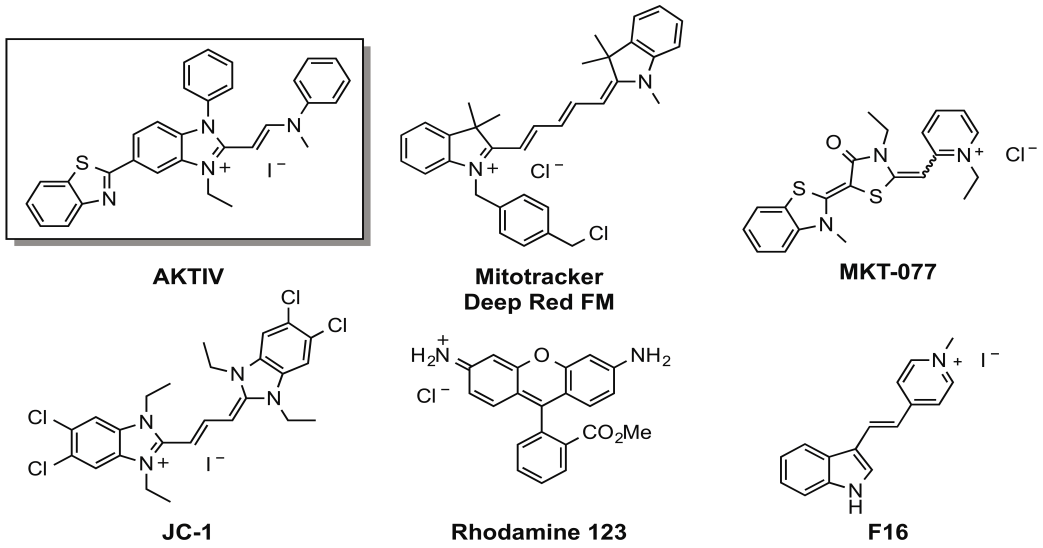

Figure 2.3. Comparison of the structure of AKTIV with other small molecules that selectively accumulate in mitochondria of mammalian cells.

To quantify the extent of bioaccumulation of small molecules in mitochondria, we initially analyzed the fluorescence of bead standards upon excitation at 405 nm and 488 nm. This allowed standard curves of molecular equivalents of the fluorophores Cascade Blue (for AKTIV) and fluorescein (for rhodamine 123) to be constructed. Human Jurkat cells were briefly treated with AKTIV or rhodamine 123 for 15 min, subjected to flow cytometry under the same conditions, and the number of fluorophores per cell was calculated based on the brightness of Cascade Blue (Φ= 0.54, $\varepsilon_{399\ nm}$ = 28,000 $M^{-1}\,cm^{-1}$)[33] and fluorescein ($\Phi_{pH\ 9}$ = 0.93, $\varepsilon_{490\ nm}$ = 76,900 $M^{-1}\,cm^{-1}$).[34] As shown in Figure 2.4,

based on the published[35] average cell volume (663.7 μm^3) and mitochondrial volume (33.4 μm^3) of Jurkat lymphocytes, concentrations of rhodamine 123 and AKTIV in mitochondria were determined. These studies revealed that after treatment of cells with culture media containing 0.05 to 5 μM of these compounds, rhodamine 123 reached concentrations of 1–548 μM in mitochondria. Under the same conditions, AKTIV accumulated to 17–1,435 μM in these organelles. Correspondingly, when 1 μM of AKTIV was added to cells for 15 minutes, over 250-fold bioaccumulation in mitochondria was observed. A 250-fold accumulation represents a ΔE ~147 mV (Nerst equation), which is similar to typical resting mitochondrial membrane potentials. This level of mitochondrial accumulation is consistent with data on other lipophilic cations.[36-37] This rapid, selective, and massive accumulation in mitochondria provides strong evidence that these organelles may be a major and direct target of the biological effects of this small molecule.

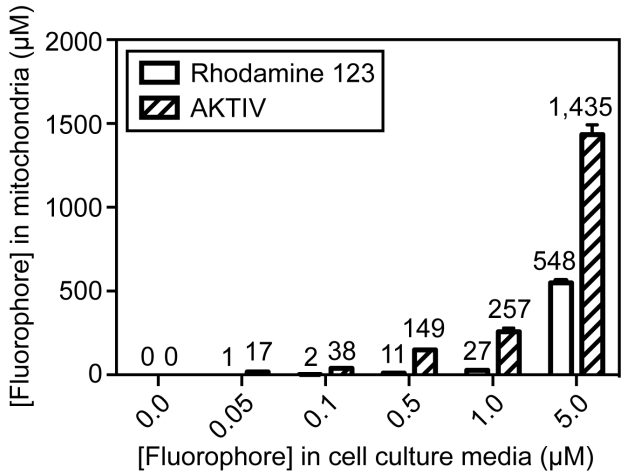

Figure 2.4. Concentrations of rhodamine 123 and AKTIV in mitochondria of Jurkat lymphocytes after treatment for 15 minutes at 37 °C. Treated cells were analyzed by flow cytometry with excitation at 488 nm (rhodamine 123) or 405 nm (AKTIV). Cellular fluorescence was converted to concentration using a standard curve constructed with

SpheroTech Rainbow Ultra beads and a ratio of mitochondrial volume to total cell volume of 0.053. Error bars represent the standard deviation.

2.5 Changes in Mitochondrial Morphology upon Treatment with AKTIV

To probe the effects of AKTIV on mitochondria, we examined the morphology of these organelles in HeLa cells by confocal laser scanning microscopy. In living cells, mitochondria constantly undergo fusion and fission events on the timescale of several minutes, and these dynamic processes play key roles in mitochondrial biogenesis, cellular energetics, apoptosis, and mitochondrial morphology.[38-39] Compared to the vehicle (0.1% DMSO) control, when HeLa cells were treated with AKTIV (1 μM) for 20 min, rapid and extensive swelling of the normally tubular mitochondria was observed (Figure 2.5, compare panel D-F). This swelling was followed by similarly rapid disintegration of these organelles into smaller structures. As a positive control, hydrogen peroxide was used to induce oxidative stress and disrupt the mitochondrial network.[40] In HeLa cells treated with H_2O_2 (1 mM) for 20–40 minutes, fragmentation of the mitochondrial network was observed, but this treatment did not cause the swelling or disintegration associated with AKTIV (Figure 2.5). These results indicate that AKTIV profoundly disrupts the morphology of mitochondria of HeLa cells, inducing distinctive phenotype of swelling followed by disintegration of these organelles.

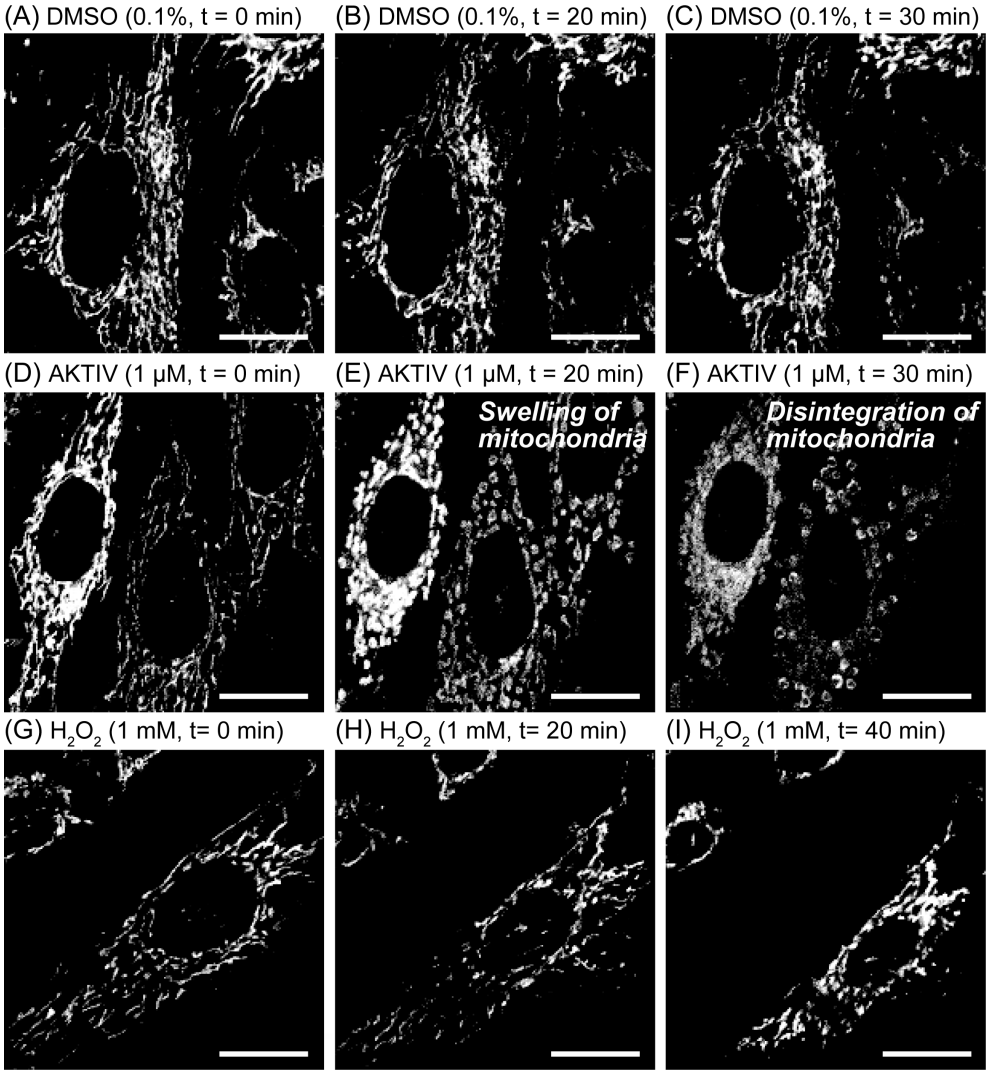

Figure 2.5. Confocal laser scanning micrographs of living HeLa cells treated with Mitotracker Deep Red FM (100 nM). Cells were further treated with DMSO (0.1%, Panels A–C), AKTIV (1 μM, Panels D–F), or hydrogen peroxide (1 mM, panels G–I) at 37 °C. The same field of cells was imaged at the three times shown. Scale bar = 20 μm.

2.6 Cellular Toxicity Induced by AKTIV

Elevated mitochondrial membrane potential is a hallmark of cancer.[30, 41-42] To examine the effect of AKTIV on cell lines that differ in mitochondrial membrane potential, we compared the toxicity of this compound with an uncharged desethyl analogue (DEAKTIV)[13] towards two cancer cell lines (HeLa and Jurkat) and the normal

monkey kidney cell line CV-1. The DEAKTIV analogue was chosen as a control because it lacks the fixed positive charge needed to drive accumulation into mitochondria. DEAKTIV is weakly basic (calculated pKa = 4.5) relative to the more basic environment of the mitochondrial lumen (~pH 8.0). As shown in Figure 2.6 (Panel A), AKTIV was highly toxic towards HeLa (IC_{50} = 320 ± 30 nM) and Jurkat (IC_{50} = 340 ± 30 nM) cells, but this compound was less toxic towards normal CV-1 cells (IC_{50}= 870 ± 90 nM), which have been shown to exhibit a lower inherent mitochondrial membrane potential.[43] The uncharged but structurally similar DEAKTIV analogue was not toxic to any of these cell lines (IC_{50} > 10 μM), providing evidence that the positive charge of AKTIV drives this compound into mitochondria.

2.7 Depolarization of the Mitochondrial Electrochemical Gradient by AKTIV

To examine the functional consequences of treatment with AKTIV, the fluorescent probe JC-1 (Figure 2.3) was used to measure effects on the membrane potential of mitochondria. This probe undergoes a shift in fluorescence emission from green to red as it accumulates in mitochondria, and by analysis of this red/green ratio, one can quantify the extent of mitochondrial depolarization. As shown in Figure 2.6 (Panel B), treatment with AKTIV for 2 h depolarized mitochondria of HeLa cells (IC_{50}= 920 ± 30 nM) and Jurkat cells (IC_{50}= 750 ± 30 nM) at submicromolar concentrations, whereas treatment with DEAKTIV was inconsequential.

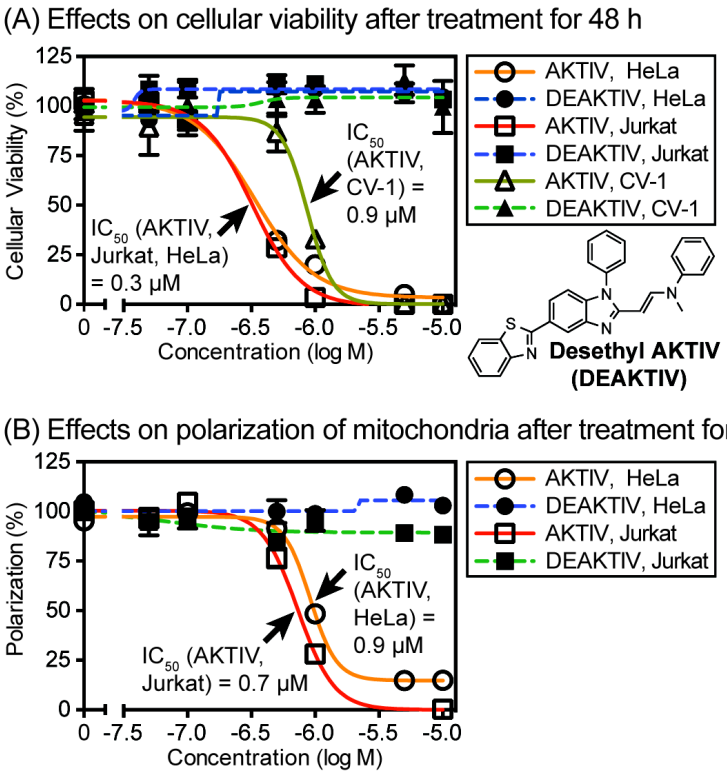

Figure 2.6. Panel A: Cytotoxicity of AKTIV and the uncharged DEAKTIV analogue towards two cancer cell lines (HeLa, Jurkat) and a normal cell line (CV-1) after 48 h. Panel B: Effect of these compounds on the polarization of mitochondria as assayed with the ratiometric fluorescent probe JC-1 (1 µM).

2.8 Inhibition of Cellular Respiration by AKTIV

Mitochondria predominantly produce cellular ATP during aerobic respiration.[30] To determine whether AKTIV inhibits this process, we used a MitoXpress Xtra-HS assay (Luxcel) to measure the consumption of oxygen by mitochondria in HeLa cells (Figure 2.7, panel A). This commercial assay uses an immobilized platinum-containing porphyrin fluorophore that is quenched upon binding oxygen, allowing monitoring of changes in extracellular oxygen over time.[44] Consistent with previous studies,[45] carbonyl cyanide 3-chlorophenylhydrazine (CCCP), an uncoupling agent that disrupts mitochondrial electron transport chain activity by bypassing efflux of protons through the ATP synthase complex, accelerated consumption of O_2 compared to vehicle control. In

contrast, AKTIV (2 μM) completely blocked consumption of O_2 over the 90-minute time course of the experiment. This inhibition was comparable to treatment with 10 μM of the mitochondrial complex I inhibitor rotenone.[45] Addition of LY294002 (10 μM), a well-characterized inhibitor of PI3K/Akt pathway,[46] showed no effect on O_2 consumption, demonstrating that blocking this pathway under these conditions does not affect mitochondrial respiration. This control experiment provides evidence that the inhibition of mitochondrial respiration by AKTIV is upstream of the PI3K/Akt pathway.

2.9 Induction of Reactive Oxygen Species by AKTIV

Reactive oxygen species (ROS) are byproducts of the mitochondrial electron transport chain.[47] Premature leakage of electrons from OXPHOS complexes can lead to production of superoxide (O_3^-) by one-electron reduction of molecular oxygen.[48-49] Superoxide is typically transformed into two molecules of hydrogen peroxide by superoxide dismutase, which can be further transformed by catalase into molecular oxygen and water.[50] However, superoxide or hydrogen peroxide that escapes this detoxification pathway can lead to direct damage of proteins, lipids, and DNA.[48-49, 51] High levels of ROS indicate mitochondrial dysfunction and can induce apoptosis.[51] To investigate whether treatment with AKTIV induces changes in cellular ROS, which could link mitochondrial dysfunction to downstream redox-sensitive biological effects such as activation of Akt,[52] we assayed levels of ROS in Jurkat lymphocytes with the fluorescent probe H_2DCFDA. As shown in Figure 2.7 (Panel B), treatment of Jurkat cells with AKTIV (30 min) increased cellular ROS in a dose-dependent manner by up to 59-fold at 2 μM compared with the vehicle control. Treatment with hydrogen peroxide (30 min) as a

positive control increased ROS by 24-fold at 1 μM and 93-fold at 10 μM. Higher concentrations of hydrogen peroxide (50 μM) showed reduced effects that were associated with cytotoxicity. As another control, treatment with rotenone (30 min), an agent previously shown to elevate cellular ROS in HepG2 cells,[53] increased ROS in a dose-dependent manner by up to 16-fold at 50 μM. Given that phosphorylation of Akt is redox-sensitive,[52] and can be activated by treatment of cells with hydrogen peroxide, these results suggest that the mitochondrial dysfunction and production of ROS by AKTIV may be mechanistically linked to the previously reported[10] activation of Akt.

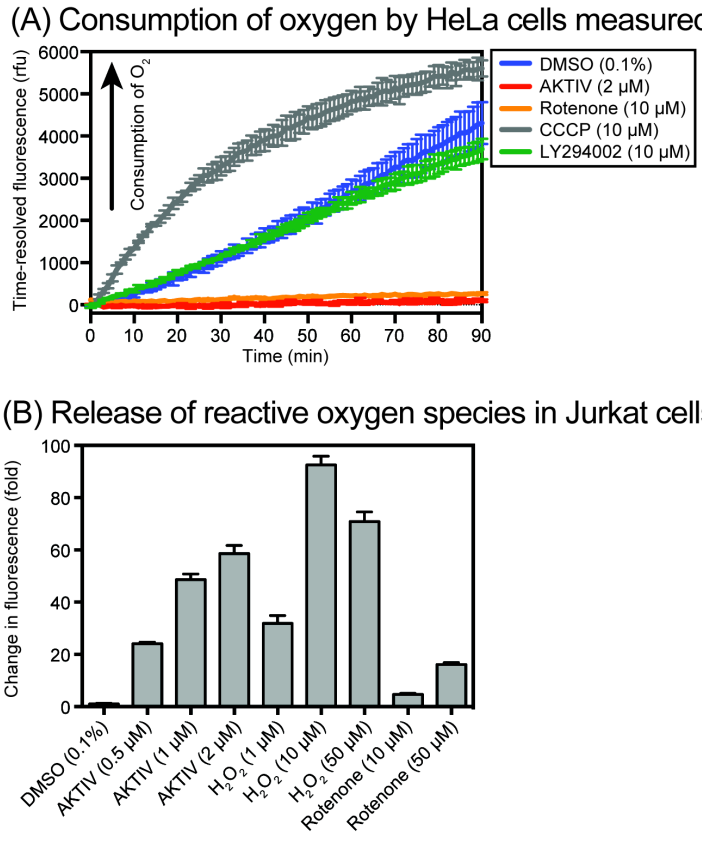

Figure 2.7. Panel A: Consumption of oxygen by HeLa cells over a 90-minute period quantified by time-resolved fluorescence with a MitOXpress XS assay. Panel B: Fluorescence of the ROS sensor H2DCFDA (2 μM) in Jurkat cells. Cells were treated for 30 minutes followed by analysis by flow cytometry. Error bars represent standard errors of the mean.

2.10 Conclusions

Based on its effects on the nuclear export of FOXO1a, AKTIV was initially proposed[1] to function as an inhibitor of the PI3K/Akt pathway. However, a more recent investigation by Connor[10] concluded that this compound does not inhibit any known kinases in this signaling pathway; moreover, AKTIV increases phosphorylation of Akt kinase when added to BHK-21 cells at concentrations that elicit major biological effects. To investigate its mechanism of action, we used intrinsic fluorescence to examine the subcellular localization of AKTIV. Imaging of treated HeLa cells by confocal microscopy with excitation at 405 nm revealed mitochondria as a major target of this potent anticancer/antiviral agent. When cancer cell lines were treated with 0.5 μM of this compound, AKTIV rapidly accumulated by over 250-fold in these organelles compared to media concentrations within 15 minutes (Figure 2.4) and caused profound mitochondrial dysfunction. Low concentrations of AKTIV triggered swelling, disintegration, and depolarization of mitochondria, elevation of ROS, and essentially complete inhibition of cellular consumption of oxygen. This rapid elevation of ROS provides a potential mechanistic link between mitochondrial dysfunction induced by AKTIV and increased phosphorylation[10] of the redox-sensitive[52] Akt kinase observed at low concentrations. These studies revealed a potentially novel mechanism of action of AKTIV that may provide a new rationale for its anticancer and broad-spectrum antiviral activities.

Because of altered glucose metabolism, cancer cells commonly exhibit elevated mitochondrial membrane potentials of at least 60 mV (negative inside) compared with normal cells.[30, 41-42] By accumulating in hyperpolarized mitochondria, delocalized

lipophilic cations such as rhodamine 123,[23, 43] dequinalinium,[54] F16,[26] MKT-077[24-25] rosamines,[55] and others[27, 56-57-58] can exhibit selective anticancer activity.[59-60] These types of compounds can affect a number of different mitochondrial targets involved in cellular proliferation including mitochondrial polarization,[26] the NADH-ubiquinone reductase,[61] the F_0F_1 ATPase,[27] and pro-apoptotic signals such as Bcl-2 family members.[62] Consequently, the selective anticancer activity of AKTIV is consistent with its profound effects on hyperpolarized mitochondria in the absence of downstream effects on the PI3K/Akt pathway.

Inhibitors of mitochondrial respiration suppress the *de novo* synthesis of pyrimidines.[63] This mechanism of action was recently reported[64] to be responsible for the broad spectrum antiviral activity of the natural product antimycin A, a mitochondrial complex III inhibitor, against RNA viruses. This antiviral activity of antimycin A and analogues was observed at nanomolar concentrations that are not toxic to mammalian host cells. Other compounds similarly shown to exhibit antiviral activity by promoting mitochondrial dysfunction include the complex III inhibitor myxothiazole, the complex I inhibitor rotenone, the proton ionophore CCCP, and the ATP synthase inhibitor oligomycin.[64] Some of these mitochondrial electron transport chain inhibitors exhibit antiviral activity under conditions where ATP production is not supressed.[64] Based on this precedent, we conclude that the broad spectrum antiviral activity of AKTIV relates to its immediate and direct effects on mitochondria either through suppression of de novo synthesis of pyrimidines, the generation of mitochondrial ROS, and/or depletion of cellular ATP. Consequently, the discovery that mitochondria, a major target of AKTIV, are profoundly affected within minutes of treatment of cells at concentrations of 1 μM or

less, provides a unifying explanation for many of the diverse biological activities of this potent small molecule. Future work to indentify a specific molecular target(s) of AKTIV in mitochondria would be of interest to define the profound cellular effects observed. In future work, forward and reverse genetics, as well as proteomic studies, could be explored to better explain the mechanism of this potent small molecule.

2.11 Experimental Methods

2.11.1 Spectroscopy. AKTIV and DEAKTIV were prepared as previously reported.[65] Samples were analyzed in a quartz SUPRASIL Macro/Semi Micro cuvette (PerkinElmer, B0631132). Absorbance measurements employed an Agilent 8453 UV-Vis instrument and are baseline corrected. Emission spectra were acquired with a PerkinElmer LS 55 Fluorescence Spectrometer. Extinction coefficients (ε) were determined using Beer's law plots of absorbance as a function of concentration in PBS (pH 7.4) containing Triton-X 100 (1%). Linear regression (GraphPad Prism 5.0) provided the molecular absorptivity (M^{-1} cm^{-1}) using the equation: Absorbance = ε[concentration (M)]L, where L is the path length in cm. Relative quantum yields (Φ) were determined as previously described.[18] Briefly, the integrated fluorescence emission (410-700 nm) of both AKTIV and Pacific Blue were plotted as a function of A_{390}. The ratio of the slopes from the resulting linear regression (GraphPad Prism 5.0), and the published quantum yield of Pacific Blue (0.75),[66] was used to determine $\Phi_{AKTIV\ Ex.\ 390\ nm}$ as $slope_A/slope_B = \Phi_A/\Phi_B$. Measurements were in triplicate.

2.11.2 Cell Culture. Jurkat (TIB-152), HeLa (CCL-2), and CV-1 (CCL-70) cell lines were obtained from ATCC and cultured in a humidified CO_2 (5%) incubator at 37 °C. Dulbecco's Modified Eagle Medium (DMEM, Sigma D5796) and RPMI-1640 (Sigma R8758) were supplemented with FBS (10%, Sigma F0926), penicillin (100 units/L), and streptomycin (100 µg/L, Sigma P4333).

2.11.3 Microscopy. Prior to treatment with compounds, adherent cells in DMEM were added to an 8-well cover glass slide (Idibi µ-Slide, 200 µL, 20,000 cells/well) and allowed to proliferate for 24 h. Compounds in concentrated DMSO stock solutions were diluted 1000-fold with complete media prior to addition to cells. Cells labeled with MitoTracker Deep Red FM (MTDR, Life Technologies) were treated with this fluorophore (100 nM, 15 min), washed with complete media, and subsequently treated with AKTIV (1 µM, 5 min) without further washing. Cells were imaged using a Leica SPE2 confocal laser-scanning microscope fitted with a 63X objective. AKTIV was excited with a 405 nm laser and emitted photons were collected from 415 nm to 480 nm. MTDR was excited with a 635 nm laser and emitted photons were collected from 645 nm to 700 nm. For the time-lapse experiments shown in Figure 2.5 and the supporting videos, a 635 nm laser was exclusively used for excitation, and images of the same field of cells were generated every minute for 30 to 40 min. In figures with multiple panels of images, the microscope settings and image processing parameters for each panel were identical.

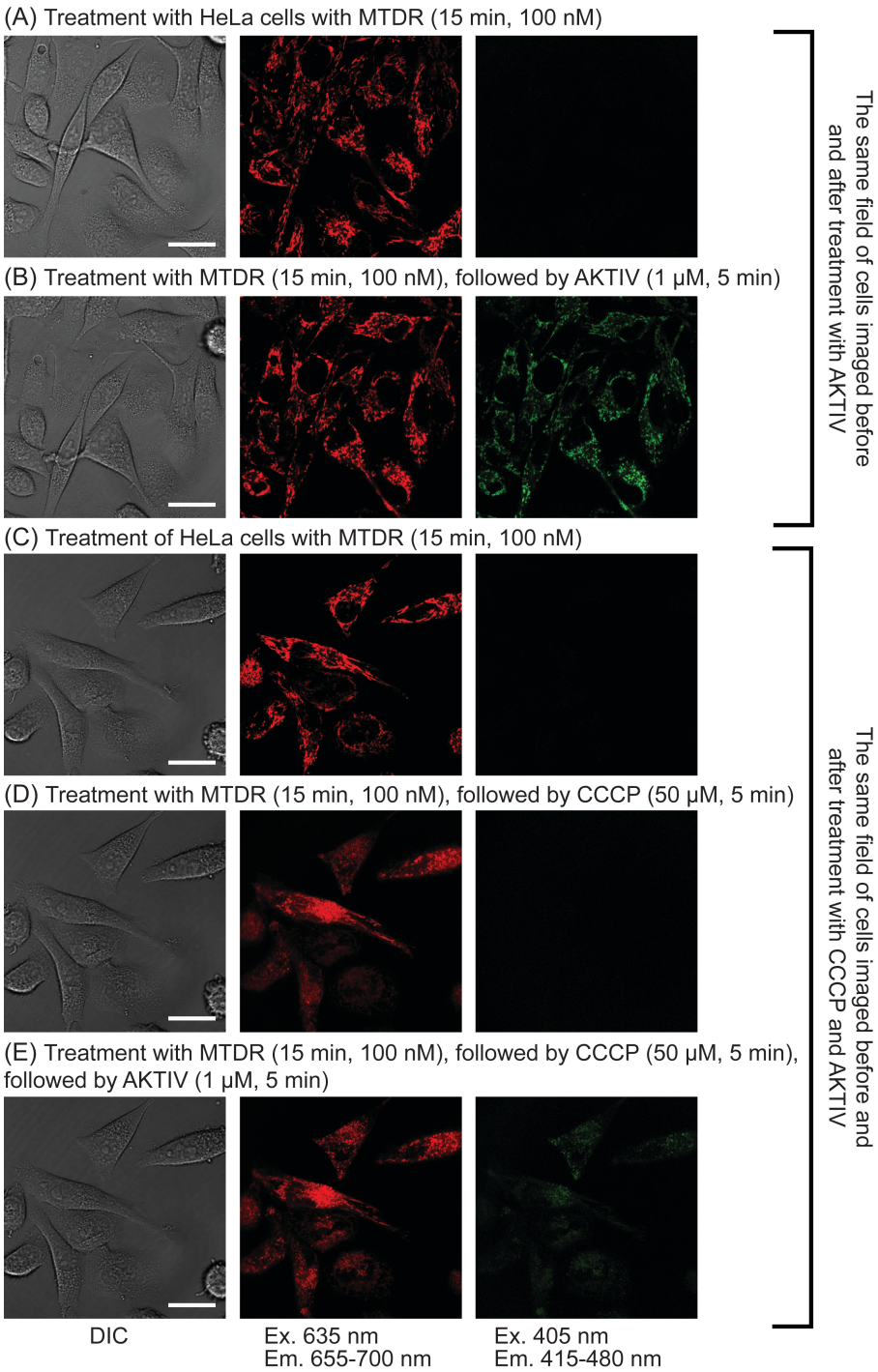

Figure 2.8. Confocal laser scanning and DIC micrographs of HeLa cells treated with MitoTracker Deep Red FM (MTDR), CCCP, and AKTIV. Compounds were added to living cells on a cover glass on the inverted microscope. The before and after images of the same field of cells validate the specific fluorescent signals are not due to differences in the field of cells selected. Rapid depolarization of mitochondria by CCCP inhibits cellular uptake of AKTIV (compare panels B with E). Scale bar = 25 μm.

2.11.4 Quantification of Accumulation of Small Molecules in Mitochondria. Jurkat cells (1 mL, 250,000 cells) were treated in duplicate with complete RMPI medium containing AKTIV or rhodamine 123 (0.1% DMSO) for 15 minutes at 37 °C. Cells were washed with Hank's Balanced Salt Solution (HBSS, Mediatech Inc). Jurkat cells treated with rhodamine 123 were analyzed with an Accuri C6 flow cytometer (488 nm excitation, 530 ± 15 nm emission). Jurkat cells treated with AKTIV were analyzed with a BD LSR II flow cytometer (405 nm excitation, 450 ± 25 nm emission). Standard curves for molecular equivalents of fluorescein (MEFL) and cascade blue (MECSB) were created using 6-peak Ultra Rainbow Calibration Beads (Spherotech). Molecular equivalents of AKTIV (MEAKTIV) were obtained by multiplying MECSB values by 257 to correct for the relative brightness (ε*Φ) of AKTIV (ε_{390}= 54,000 $M^{-1}cm^{-1}$, Φ= 0.0016, A_{405}/A_{390} = 0.68) compared with Cascade Blue (ε_{399}= 28,000 $M^{-1}cm^{-1}$, Φ= 0.54). The emission of AKTIV and Cascade Blue was very similar under these conditions.[33] MEFL values from cells treated with rhodamine 123 were converted into molecular equivalents of rhodamine 123 (MERho123) by mulitiplication by 1.03 to correct for differences in relative brightness of these fluorophores. This MEFL/MERho123 correction factor (1.03) was obtained by integration (515-545 nm) of the emission spectra of solutions of both fluorescein and rhodamine 123 (25 nM) in PBS (pH = 7.4) upon irradiation at 488 nm, using excitation and emission windows that match the flow cytometer. MEAKTIV and MERho123 values were converted into concentration in mitochondria by conversion to moles (molecular equivalents/Avogadro's number) and published[35] values for the average volume of a Jurkat cell (663.7 μm^3) and the ratio (0.053) of mitochondrial volume to total cell volume. To account for quenching of fluorophores at high

concentrations in mitochondria, as shown in Figure S1, multiplication factors were generated based on differences between plots of linear and exponential functions at different fluorophore concentrations. These factors were used to correct the measured concentrations of AKTIV and rhodamine 123 in mitochondria due to fluorescence quenching. Untreated cells were used for baseline corrections to eliminate any potential contributions from autofluorescence.

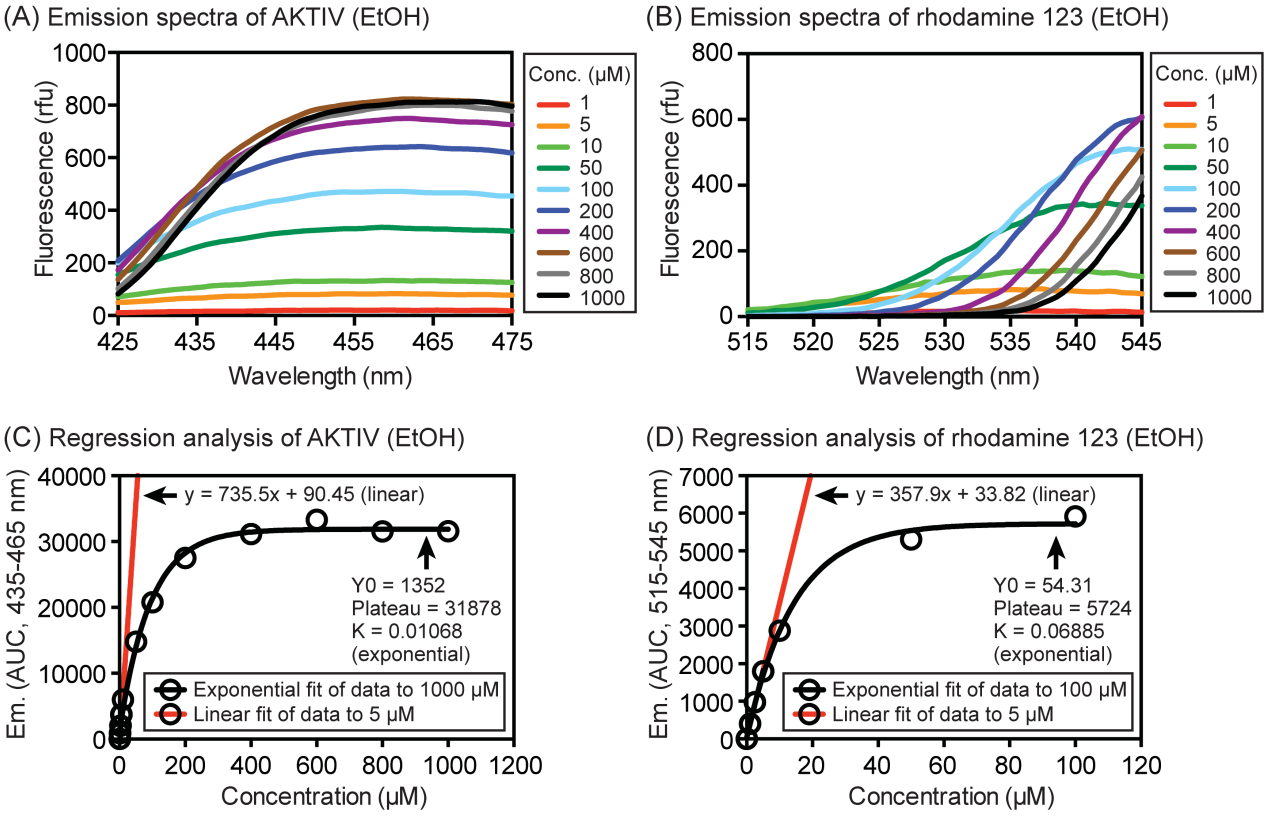

Figure 2.9. Concentration-dependent quenching of the fluorescence emission of AKTIV and rhodamine 123 in ethanol. The fluorophores were excited at 405 nm (AKTIV) or 488 nm (rhodamine 123) to match the laser lines used in flow cytometry studies of living cells. Emission spectra, at wavelengths analyzed by flow cytometry, were generated as shown in Panels A and B (a 1% transmission attenuator was used to filter the emission of rhodamine 123). These emission windows were integrated and the areas under the curve (AUC) were plotted as shown in Panels C and D. Linear regression was used to fit the data for concentrations of 5 μM and lower, where fluorescence quenching was not observed, whereas quenching of the fluorescence observed at higher concentrations was fit to a one-phase exponential association model (R^2>0.99, GraphPad Prism 6

software). Differences between these functions were used to correct for quenching of fluorophores at elevated concentrations in mitochondria.

2.11.5 Cytotoxicity Assays. HeLa and CV-1 cells (150 µL, 4,000 cells) in complete DMEM were added to a 96-well plate (CytoOne, CC7682-7596) and allowed to proliferate for 24 h. This medium was replaced with complete DMEM containing AKTIV or DEAKTIV (0.1% DMSO). Jurkat cells (150 µL, 4,000 cells) were suspended in complete RPMI medium containing AKTIV or DEAKTIV (0.1% DMSO) on a 96-well plate. These plates were incubated for 48 h at 37 °C. Following incubation, HeLa and CV-1 wells were washed with PBS (200 µL), treated with trypsin (50 µL) for 5 min, followed by DMEM (100 µL) containing propidium iodide (3 µM, PI). Cellular viability was measured with an Accuri C6 flow cytometer by analysis of light scattering and cellular uptake of PI. Jurkat cells were pelleted in eppendorf tubes (0.5 mL), the supernatant was removed, and the media was replaced with fresh RMPI containing PI (2 µM) prior to analysis by flow cytometry. Total cell counts were normalized between 0 and the average of the vehicle-treated (0.1% DMSO) samples. IC_{50} values were calculated using non-linear regression (GraphPad Prism 6.0 with a four-parameter model). The calculated pKa for DEAKTIV was done calculated with ChemAxon MarvinView 6.2.

2.11.6 Analysis of Effects on Polarization of Mitochondria. The ratiometric JC-1 fluorophore (Life Technologies) was used to determine effects on mitochondrial membrane potential. HeLa cells were plated 24 h in advance on a 24-well plate (1 mL of complete DMEM, 200,000 cells). Jurkat cells (1 mL of complete RPMI, 250,000 cells)

were plated immediately prior to the assay. JC-1 (1 μM, 0.1% DMSO) was added and cells were incubated at 37 °C for 30 min. Jurkat cells were pelleted and washed with fresh medium. HeLa cells were washed with PBS (200 μL), treated with trypsin (0.25%, 200 μL) for 5 min at 37 °C, followed by addition of complete DMEM (800 μL) to create a cell suspension. Cell solutions were analyzed by flow cytometry (Accuri C6) with excitation at 488 nm. Analysis of light scattering was used to eliminate cell debris. Mitochondrial polarization was measured as the red-to-green ratio of cellular fluorescence calculated for each treatment. Ratios were normalized between the vehicle control (0.1% DMSO) and CCCP (50 μM) as a positive control. IC_{50} values were calculated by non-linear regression (GraphPad Prism 6.0 using a four parameter model).

2.11.7 Analysis of Oxygen Consumption by Mitochondria. MitoXpress-Xtra HS (Luxcel) was used to assay cellular consumption of O_2. HeLa cells were treated with trypsin-EDTA (3 mL, 0.25%) for 5 min at 37 °C to create a suspension. Complete DMEM (12 mL) was added. The cells were pelleted (2000 rpm, 2 min), the supernatant was removed, and the cells were re-suspended at 5000 cells / μL of media. This suspension of HeLa cells (50 μL, 250,000 cells) was added to each well of a black, clear-bottomed 96-well plate. A stock solution of the Pt-porphyrin probe MitoXpress-Xtra HS in water (10 μL, 1 μM) was added to each well. Concentrated (1.5 X) solutions of compounds in complete DMEM were added to achieve the desired concentrations in each well. To each well, the compound in complete DMEM (0.1 mL) was added. Each well was sealed with MitoXpress HS mineral oil (80 μL), the plate was transferred to a

pre-warmed (37 °C) plate reader (SpectraMax M5, Molecular Devices), and incubated for 30 min. Time-resolved fluorescence readings were obtained using excitation at 380 nm, emission at 650 nm, and a 630 nm long pass filter. Time-resolved parameters were set at a 50 μs delay and a 100 μs integration gate. Measurements were taken every minute for 90 min. Compounds were evaluated in duplicate. Results were plotted (GraphPad Prism 6.0) and were baseline corrected using the average of the first three data points for each well.

2.11.8 Measurement of Reactive Oxygen Species. Jurkat lymphocytes in HBSS (480,000 cells/mL) were treated with freshly prepared H2DCFDA (2 μM, 0.1% DMSO) at 37 °C for 30 min. These cells were pelleted, washed with complete RPMI medium, and treated with compounds (120 μL of complete RPMI, 50,000 cells) in duplicate. Cellular fluorescence was measured with an Accuri C6 flow cytometer after 30 min. Median fluorescence values were plotted with GraphPad Prism 6.0.

2.12 References

1. Kau, T. R.; Schroeder, F.; Ramaswamy, S.; Wojciechowski, C. L.; Zhao, J. J.; Roberts, T. M.; Clardy, J.; Sellers, W. R.; Silver, P. A., A chemical genetic screen identifies inhibitors of regulated nuclear export of a Forkhead transcription factor in PTEN-deficient tumor cells. *Cancer cell* **2003,** *4* (6), 463-476.

2. Koeller, K. M.; Haggarty, S. J.; Perkins, B. D.; Leykin, I.; Wong, J. C.; Kao, M. C.; Schreiber, S. L., Chemical genetic modifier screens: small molecule trichostatin

suppressors as probes of intracellular histone and tubulin acetylation. *Chem. Biol.* **2003,** *10* (5), 397-410.

3. Margalit, D. N.; Romberg, L.; Mets, R. B.; Hebert, A. M.; Mitchison, T. J.; Kirschner, M. W.; RayChaudhuri, D., Targeting cell division: small-molecule inhibitors of FtsZ GTPase perturb cytokinetic ring assembly and induce bacterial lethality. *Proc. Natl. Acad. Sci. U.S.A.* **2004,** *101* (32), 11821-11826.

4. Koomoa, D. L.; Yco, L. P.; Borsics, T.; Wallick, C. J.; Bachmann, A. S., Ornithine decarboxylase inhibition by alpha-difluoromethylornithine activates opposing signaling pathways via phosphorylation of both Akt/protein kinase B and p27Kip1 in neuroblastoma. *Cancer. Res.* **2008,** *68* (23), 9825-9831.

5. Hu, C.; Solomon, V. R.; Ulibarri, G.; Lee, H., The efficacy and selectivity of tumor cell killing by Akt inhibitors are substantially increased by chloroquine. *Bioorg. Med. Chem.* **2008,** *16* (17), 7888-7893.

6. Conley-LaComb, M. K.; Saliganan, A.; Kandagatla, P.; Chen, Y. Q.; Cher, M. L.; Chinni, S. R., PTEN loss mediated Akt activation promotes prostate tumor growth and metastasis via CXCL12/CXCR4 signaling. *Mol. Cancer* **2013,** *12* (1), 85.

7. Takamatsu, R.; Takeshima, E.; Ishikawa, C.; Yamamoto, K.; Teruya, H.; Heuner, K.; Higa, F.; Fujita, J.; Mori, N., Inhibition of Akt/GSK3beta signalling pathway by Legionella pneumophila is involved in induction of T-cell apoptosis. *Biochem. J.* **2010,** *427* (1), 57-67.

8. Fruman, D. A.; Rommel, C., PI3K and cancer: lessons, challenges and opportunities. *Nat. Rev. Drug Discov.* **2014,** *13* (2), 140-156.

9. Garcia-Echeverria, C.; Sellers, W. R., Drug discovery approaches targeting the PI3K/Akt pathway in cancer. *Oncogene* **2008,** *27* (41), 5511-5526.

10. Dunn, E. F.; Fearns, R.; Connor, J. H., Akt inhibitor Akt-IV blocks virus replication through an Akt-independent mechanism. *J. Virol.* **2009,** *83* (22), 11665-11672.

11. Blaustein, M.; Perez-Munizaga, D.; Sanchez, M. A.; Urrutia, C.; Grande, A.; Risso, G.; Srebrow, A.; Alfaro, J.; Colman-Lerner, A., Modulation of the Akt pathway reveals a novel link with PERK/eIF2alpha, which is relevant during hypoxia. *PLoS One* **2013,** *8* (7), e69668.

12. Sun, M.; Fuentes, S. M.; Timani, K.; Sun, D.; Murphy, C.; Lin, Y.; August, A.; Teng, M. N.; He, B., Akt plays a critical role in replication of nonsegmented negative-stranded RNA viruses. *J. Virol.* **2008,** *82* (1), 105-114.

13. Sun, Q.; Wu, R.; Cai, S.; Lin, Y.; Sellers, L.; Sakamoto, K.; He, B.; Peterson, B. R., Synthesis and biological evaluation of analogues of AKT (protein kinase B) inhibitor-IV. *J Med Chem* **2011,** *54* (5), 1126-39.

14. Luthra, P.; Sun, D.; Wolfgang, M.; He, B., AKT1-dependent activation of NF-kappaB by the L protein of parainfluenza virus 5. *J. Virol.* **2008,** *82* (21), 10887-10895.

15. Lavis, L. D.; Raines, R. T., Bright building blocks for chemical biology. *ACS chemical biology* **2014,** *9* (4), 855-866.

16. Lavis, L. D.; Raines, R. T., Bright ideas for chemical biology. *ACS chemical biology* **2008,** *3* (3), 142-155.

17. Loving, G. S.; Sainlos, M.; Imperiali, B., Monitoring protein interactions and dynamics with solvatochromic fluorophores. *Trends Biotechnol.* **2010,** *28* (2), 73-83.

18. Williams, A. T.; Winfield, S. A., Relative Fluorescence Quantum Yields Using a Computer-controlled Luminescence Spectrometer. *Analyst* **1983,** *108*, 1067-1071.

19. Sun, W. C.; Gee, K. R.; Haugland, R. P., Synthesis of novel fluorinated coumarins: excellent UV-light excitable fluorescent dyes. *Bioorg. Med. Chem. Lett.* **1998,** *8* (22), 3107-3110.

20. Rodrigues, R. M.; Macko, P.; Palosaari, T.; Whelan, M. P., Autofluorescence microscopy: a non-destructive tool to monitor mitochondrial toxicity. *Toxicol. Lett.* **2011,** *206* (3), 281-288.

21. Shim, S. H.; Xia, C.; Zhong, G.; Babcock, H. P.; Vaughan, J. C.; Huang, B.; Wang, X.; Xu, C.; Bi, G. Q.; Zhuang, X., Super-resolution fluorescence imaging of organelles in live cells with photoswitchable membrane probes. *Proc. Natl. Acad. Sci. U.S.A.* **2012,** *109* (35), 13978-13983.

22. Liu, T.; Hannafon, B.; Gill, L.; Kelly, W.; Benbrook, D., Flex-Hets differentially induce apoptosis in cancer over normal cells by directly targeting mitochondria. *Mol. Cancer Ther.* **2007,** *6* (6), 1814-1822.

23. Modica-Napolitano, J. S.; Aprille, J. R., Basis for the Selective Cytotoxicity of Rhodamine 123. *Cancer Res.* **1987,** *47* (16), 4361-4365.

24. Modica-Napolitano, J. S.; Koya, K.; Weisberg, E.; Brunelli, B. T.; Li, Y.; Chen, L. B., Selective Damage to Carcinoma Mitochondria by the Rhodacyanine MKT-077. *Cancer Res.* **1996,** *56* (3), 544-550.

25. Wadhwa, R.; Sugihara, T.; Yoshida, A.; Nomura, H.; Reddel, R. R.; Simpson, R.; Maruta, H.; Kaul, S. C., Selective Toxicity of MKT-077 to Cancer Cells Is Mediated by

Its Binding to the hsp70 Family Protein mot-2 and Reactivation of p53 Function. *Cancer Res.* **2000,** *60* (24), 6818-6821.

26. Fantin, V. R.; Berardi, M. J.; Scorrano, L.; Korsmeyer, S. J.; Leder, P., A novel mitochondriotoxic small molecule that selectively inhibits tumor cell growth. *Cancer cell* **2002,** *2* (1), 29-42.

27. Modica-Napolitano, J. S.; Aprille, J. R., Delocalized lipophilic cations selectively target the mitochondria of carcinoma cells. *Adv. Drug Del. Rev.* **2001,** *49* (1-2), 63-70.

28. Rin Jean, S.; Tulumello, D. V.; Wisnovsky, S. P.; Lei, E. K.; Pereira, M. P.; Kelley, S. O., Molecular vehicles for mitochondrial chemical biology and drug delivery. *ACS chemical biology* **2014,** *9* (2), 323-333.

29. Nicholls, D. G., The influence of respiration and ATP hydrolysis on the proton-electrochemical gradient across the inner membrane of rat-liver mitochondria as determined by ion distribution. *Eur. J. Biochem.* **1974,** *50* (1), 305-315.

30. Chen, L. B., Mitochondrial membrane potential in living cells. *Ann. Rev. Cell Biol.* **1988,** *4*, 155-181.

31. Perry, S. W.; Norman, J. P.; Barbieri, J.; Brown, E. B.; Gelbard, H. A., Mitochondrial membrane potential probes and the proton gradient: a practical usage guide. *Biotechniques* **2011,** *50* (2), 98-115.

32. Belostotsky, I.; da Silva, S. M.; Paez, M. G.; Indig, G. L., Mitochondrial targeting for photochemotherapy. Can selective tumor cell killing be predicted based on n-octanol/water distribution coefficients? *Biotechnic. Histochem.* **2011,** *86* (5), 302-314.

33. Whitaker, J. E.; Haugland, R. P.; Moore, P. L.; Hewitt, P. C.; Reese, M.; Haugland, R. P., Cascade Blue derivatives: Water soluble, reactive, Blue emission dyes evaluated as fluorescent labels and tracers. *Anal. Biochem.* **1991,** *198* (1), 119-130.

34. Sjoback, R.; Nygren, J.; Kubista, M., Absorption and Fluorescence Properties of Fluorescein. *Spectrochim. Acta A* **1995,** *51* (6), L7-L21.

35. Feng, Y.; Zhang, N.; Jacobs, K. M.; Jiang, W.; Yang, L. V.; Li, Z.; Zhang, J.; Lu, J. Q.; Hu, X.-H., Polarization imaging and classification of Jurkat T and Ramos B cells using a flow cytometer. *Cytometry Part A* **2014,** *85* (9), 817-826.

36. Smith, R. A. J.; Porteous, C. M.; Gane, A. M.; Murphy, M. P., Delivery of bioactive molecules to mitochondria in vivo. *Proc. Natl. Acad. Sci. U. S. A.* **2003,** *100* (9), 5407-5412.

37. Murphy, M. P., Targeting lipophilic cations to mitochondria. *Biochim. Biophys. Acta* **2008,** *1777* (7–8), 1028-1031.

38. Westermann, B., Mitochondrial fusion and fission in cell life and death. *Nat. Rev. Mol. Cell Biol.* **2010,** *11* (12), 872-884.

39. Karbowski, M.; Youle, R. J., Dynamics of mitochondrial morphology in healthy cells and during apoptosis. *Cell Death Differ.* **2003,** *10* (8), 870-880.

40. Fan, X.; Hussien, R.; Brooks, G. A., H2O2-induced mitochondrial fragmentation in C2C12 myocytes. *Free Radic. Biol. Med.* **2010,** *49* (11), 1646-1654.

41. Kadenbach, B., Intrinsic and extrinsic uncoupling of oxidative phosphorylation. *Biochim. Biophys. Acta* **2003,** *1604* (2), 77-94.

42. Wallace, D. C., Mitochondria and cancer. *Nat. Rev. Cancer* **2012,** *12* (10), 685-698.

43. Lampidis, T. J.; Bernal, S. D.; Summerhayes, I. C.; Chen, L. B., Selective Toxicity of Rhodamine 123 in Carcinoma Cells in Vitro. *Cancer Res.* **1983,** *43* (2), 716-720.

44. Hynes, J.; Hill, R.; Papkovsky, D. B., The use of a fluorescence-based oxygen uptake assay in the analysis of cytotoxicity. *Toxicol. In Vitro* **2006,** *20* (5), 785-792.

45. Marroquin, L. D.; Hynes, J.; Dykens, J. A.; Jamieson, J. D.; Will, Y., Circumventing the crabtree effect: Replacing media glucose with galactose increases susceptibility of HepG2 cells to mitochondrial toxicants. *Toxicol. Sci.* **2007,** *97* (2), 539-547.

46. Vlahos, C. J.; Matter, W. F.; Hui, K. Y.; Brown, R. F., A specific inhibitor of phosphatidylinositol 3-kinase, 2-(4-morpholinyl)-8-phenyl-4H-1-benzopyran-4-one (LY294002). *J. Biol. Chem.* **1994,** *269* (7), 5241-5248.

47. Sena, L. A.; Chandel, N. S., Physiological roles of mitochondrial reactive oxygen species. *Molecular cell* **2012,** *48* (2), 158-167.

48. Brand, M. D.; Affourtit, C.; Esteves, T. C.; Green, K.; Lambert, A. J.; Miwa, S.; Pakay, J. L.; Parker, N., Mitochondrial superoxide: production, biological effects, and activation of uncoupling proteins. *Free Radic. Biol. Med.* **2004,** *37* (6), 755-767.

49. Murphy, M. P., How mitochondria produce reactive oxygen species. *Biochem. J.* **2009,** *417*, 1-13.

50. Muller, F., The nature and mechanism of superoxide production by the electron transport chain: Its relevance to aging. *Journal of the American Aging Association* **2000,** *23* (4), 227-253.

51. Fleury, C.; Mignotte, B.; Vayssière, J.-L., Mitochondrial reactive oxygen species in cell death signaling. *Biochimie* **2002,** *84* (2–3), 131-141.

52. Ushio-Fukai, M.; Alexander, R. W.; Akers, M.; Yin, Q.; Fujio, Y.; Walsh, K.; Griendling, K. K., Reactive oxygen species mediate the activation of Akt/protein kinase B by angiotensin II in vascular smooth muscle cells. *J. Biol. Chem.* **1999,** *274* (32), 22699-22704.

53. Siddiqui, M. A.; Ahmad, J.; Farshori, N. N.; Saquib, Q.; Jahan, S.; Kashyap, M. P.; Ahamed, M.; Musarrat, J.; Al-Khedhairy, A. A., Rotenone-induced oxidative stress and apoptosis in human liver HepG2 cells. *Mol. Cell. Biochem.* **2013,** *384* (1-2), 59-69.

54. Weiss, M. J.; Wong, J. R.; Ha, C. S.; Bleday, R.; Salem, R. R.; Steele, G. D., Jr.; Chen, L. B., Dequalinium, a topical antimicrobial agent, displays anticarcinoma activity based on selective mitochondrial accumulation. *Proc. Natl. Acad. Sci. U.S.A.* **1987,** *84* (15), 5444-5448.

55. Lim, S. H.; Wu, L.; Burgess, K.; Lee, H. B., New cytotoxic rosamine derivatives selectively accumulate in the mitochondria of cancer cells. *Anticancer Drugs* **2009,** *20* (6), 461-8.

56. Fonseca, S. B.; Pereira, M. P.; Mourtada, R.; Gronda, M.; Horton, K. L.; Hurren, R.; Minden, M. D.; Schimmer, A. D.; Kelley, S. O., Rerouting chlorambucil to mitochondria combats drug deactivation and resistance in cancer cells. *Chem. Biol.* **2011,** *18* (4), 445-453.

57. Horton, K. L.; Stewart, K. M.; Fonseca, S. B.; Guo, Q.; Kelley, S. O., Mitochondria-penetrating peptides. *Chem. Biol.* **2008,** *15* (4), 375-382.

58. Modica-Napolitano, J. S.; Aprille, J. R., Delocalized lipophilic cations selectively target the mitochondria of carcinoma cells. *Adv. Drug Del. Rev.* **2001,** *49* (1–2), 63-70.

59. Smith, R. A.; Hartley, R. C.; Murphy, M. P., Mitochondria-targeted small molecule therapeutics and probes. *Antioxid. Redox Sign.* **2011,** *15* (12), 3021-3038.

60. Wang, F.; Ogasawara, M. A.; Huang, P., Small mitochondria-targeting molecules as anti-cancer agents. *Mol. Asp. Med.* **2010,** *31* (1), 75-92.

61. Anderson, W. M.; Patheja, H. S.; Delinck, D. L.; Baldwin, W. W.; Smiley, S. T.; Chen, L. B., Inhibition of bovine heart mitochondrial and Paracoccus denitrificans NADH----ubiquinone reductase by dequalinium chloride and three structurally related quinolinium compounds. *Biochem Int.* **1989,** *19* (4), 673-685.

62. Fantin, V. R.; Leder, P., Mitochondriotoxic compounds for cancer therapy. *Oncogene* **2006,** *25* (34), 4787-4797.

63. Loffler, M.; Jockel, J.; Schuster, G.; Becker, C., Dihydroorotate-ubiquinone oxidoreductase links mitochondria in the biosynthesis of pyrimidine nucleotides. *Mol. Cell. Biochem.* **1997,** *174* (1-2), 125-129.

64. Raveh, A.; Delekta, P. C.; Dobry, C. J.; Peng, W.; Schultz, P. J.; Blakely, P. K.; Tai, A. W.; Matainaho, T.; Irani, D. N.; Sherman, D. H.; Miller, D. J., Discovery of potent broad spectrum antivirals derived from marine actinobacteria. *PLoS One* **2013,** *8* (12), e82318.

65. Sun, Q.; Wu, R.; Cai, S.; Lin, Y.; Sellers, L.; Sakamoto, K.; He, B.; Peterson, B. R., Synthesis and biological evaluation of analogues of AKT (protein kinase B) inhibitor-IV. *J. Med. Chem.* **2011,** *54* (5), 1126-1139.

66. Sun, W.-C.; Gee, K. R.; Haugland, R. P., Synthesis of novel fluorinated coumarins: Excellent UV-light excitable fluorescent dyes. *Bioorg. Med. Chem. Lett.* **1998,** *8* (22), 3107-3110.

Chapter 3

Synthesis of Fluorophores that Target Small Molecules to the Endoplasmic Reticulum of Living Mammalian Cells

3.1 Introduction

The endoplasmic reticulum (ER), an organelle found in all eukaryotic cells, generally contains at least half of all the membranes found in animal cells. The ER is spread throughout the cytosol to define a network of tubes and sacs that enclose a single internal space termed the lumen. Numerous processes essential for cellular maintenance and survival occur on and in the ER. The external surface of the ER captures ribosomes involved in translation of membrane-bound and secreted proteins, whereas the lumen stores intracellular calcium, regulates folding and posttranslational processing of proteins in the secretory pathway, and is a major site of cellular lipid biosynthesis.[1]

Stressful conditions can cause unfolded proteins to accumulate in the ER.[2] These stressors include changes in redox status due to hypoxia, oxidants or reductants, glucose deprivation, altered calcium regulation, viral infection and expression of aberrant proteins. This triggers an unfolded protein response (UPR) in the ER that initiates complex signaling pathways. These pathways either promote adaptive responses such as upregulation of protective proteins, or cellular death through apoptosis or even necrosis when stress is excessive.[3] Numerous pathologies are

associated with ER stress including neurodegenerative disease, stroke, heart disease, diabetes, and cancer.[4-7]

Because of the importance of the ER in disease, modulators of targets in this organelle are of substantial interest as potential therapeutics and probes. Small molecules that promote ER stress and trigger apoptosis have potential as anticancer agents, and may exhibit a unique cytotoxic mechanism of action that avoids mutagenic damage to DNA.[4] Small molecules known to induce ER stress include tunicamycin,[8-9] brefeldin A,[10-12] versipelostatin,[13-15] bortezomib (Velcade),[16-17] and eeyarestatin I.[18-24]

Some small molecules accumulate selectively in the ER. These compounds are generally amphipathic and moderately lipophilic.[25] Structures of highly fluorescent[26] molecular probes that allow selective imaging of this organelle by microscopy, including ER Tracker Blue-White DPX[27] and BODIPY Nile Red,[28] are shown in Figure 3.1. The selectivity of these compounds for the ER has been proposed[25, 29] to involve association with lipids comprising the cholesterol-poor ER membranes.[30] Despite the ER membrane having a surface area comparable to or greater than the plasma membrane, only 0.5-1% of the total cellular cholesterol is contained in the ER verses the 30-40% of the total cellular cholesterol contained in the plasma membrane.[31-32] Cholesterol content of other organelles (Golgi, mitochondria, lysosomes, etc) is intermediate between these two extremes.[33] Other fluorescent ER probes, such as ER Tracker Green and ER Tracker Red (Figure 3.1), link the BODIPY fluorophore to glibenclamide. This compound binds to sulphonylurea receptors of ATP-sensitive potassium channels that are abundant on the cytosolic face of ER membranes.[34] However, binding to these channels can alter ER

function by perturbing calcium homeostasis,[35] and probes of the ER that do not bind potassium channels may be advantageous for imaging and delivery applications.

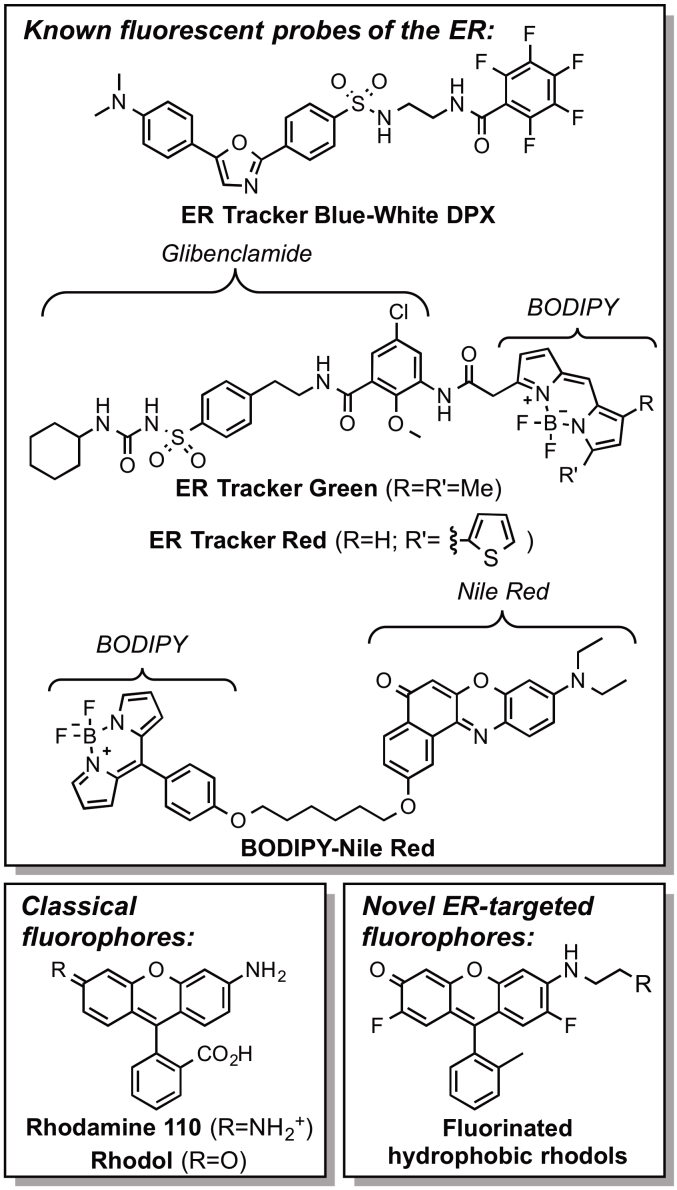

Figure 3.1. Structures of known fluorescent probes of the ER (top), the classical fluorophores rhodamine 110 and rhodol (bottom left), and novel fluorinated hydrophobic rhodols (bottom right).

Here, we report the synthesis of a new class of fluorinated hydrophobic rhodols (Figure 3.1). These highly fluorescent compounds are structurally related to the

fluorophores rhodol and rhodamine 110 (Figure 3.1). However, these rhodol analogues are distinct from other rhodols and rhodamines in that they selectively accumulate in the ER of living mammalian cells. To explore the utility of this unique biological activity, we coupled a fluorinated hydrophobic rhodol to (2*E*)-3-(5-nitro-2-furanyl)-2-propenal. This nitrofuran, present as the hydrazone derivative in the ER-targeted agent eeyarestatin I, inhibits the protein p97[22] to block the ubiquitin-proteasome system (UPS). We demonstrate that an analogous ER-targeted rhodol-nitrofuran enhances cytotoxicity in HeLa cells compared to an nitrofuran derivative that is not targeted to the ER, and blocks the UPS, offering a specific mechanism of cytotoxicity against a cancer cell line. These compounds represent a novel fluorescent chemotype for the targeting of pathways that are specifically localized in the ER of living mammalian cells.

3.2 Synthesis of Hydrophobic Fluorinated Rhodols

Our laboratory recently reported improved methodology[36-37] for the synthesis of 2,7-difluoro-3,6-dihydroxyxanthene-9-one (**1**, Figure 3.2). This xanthone building block was used to prepare multigram quantities of the fluorinated fluorophore Pennsylvania Green (**2**)[38-39] via a previously published method.[37, 39] At neutral pH, Pennsylvania Green (**2**) is anionic (bearing a delocalized phenolate, pKa = 4.8), hydrophobic ($cLogD_{pH7.4}$ = 2.5), and cell-permeable.[38] To investigate the properties of derivatives that replace the hydroxyl group of **2** with secondary amines, we transformed **2** into iodoarene **3**, followed by conversion to rhodol **4** under Buchwald-Hartwig cross-coupling conditions with microwave irradiation (Figure 3.2). This approach is similar to methods used to prepare other rhodols[40] and rhodamines.[41] Consistent with other reports,[42-43]

microwave irradiation was found to accelerate the reaction compared with conventional heating, and the iodoarene **3** proved to be a more stable intermediate compared to the corresponding phenolic triflate ester. Rhodol **4** represents a unique fluorinated hydrophobic (cLogP = 3.9) analogue of other previously reported[40, 44-48] rhodol fluorophores that are typically negatively charged at physiological pH (typical cLogP < 1, see structures of Figure 3.3D).

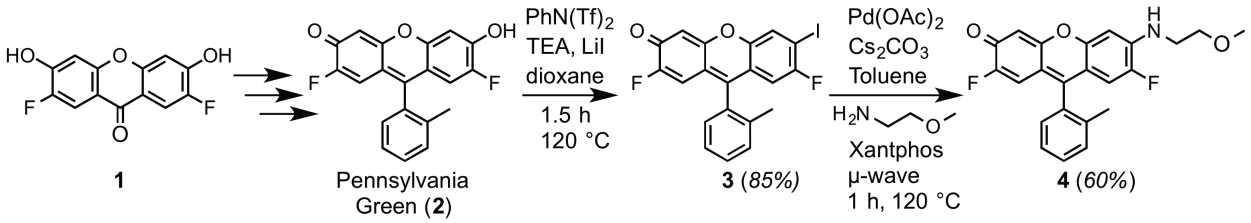

Figure 3.2. Synthesis of the fluorinated rhodol **4**.

3.3 Photophysical Properties of Hydrophobic Fluorinated Rhodols

Rhodols are generally fluorescent in a wide variety of solvents.[40, 44] To examine the photophysical properties of rhodol **4**, we obtained absorbance and fluorescence emission spectra of this compound in PBS, ethanol, and octanol. We further measured the quantum yield of **4** in PBS and ethanol, relative[49] to rhodamine 6G, and the extinction coefficient in EtOH and PBS (Figure 3.3). As shown in Figure 3.3, **4** exhibited spectral properties (Abs. λ_{max} = 512 nm; Ex. λ_{max} = 532 nm, ε = 73,500 M^{-1} cm^{-1}, Φ (EtOH) = 0.84) between fluorescein (Abs. λ_{max} = 490 nm, Em. λ_{max} = 517 nm, ε = 76,900–87,600 M^{-1} cm^{-1}, Φ (aqueous, pH > 8) = 0.92-0.95)[50-52] and rhodamine 6G (Abs. λ_{max} = 530 nm, Em. λ_{max} = 552 nm, ε = 116,000 M^{-1} cm^{-1}, Φ (EtOH) = 0.95).[52-53] These

properties enable convenient excitation of **4** with either the 488 nm or 532 nm laser lines commonly found on many confocal laser scanning microscopes. Because this compound is substantially brighter than structurally similar rhodols bearing tertiary amines,[48] and based on other published studies of rhodols bearing secondary amines,[45, 54] the secondary amine substituent of **4** undoubtedly contributes to its high quantum yield (see comparison of Figure 3.3D).

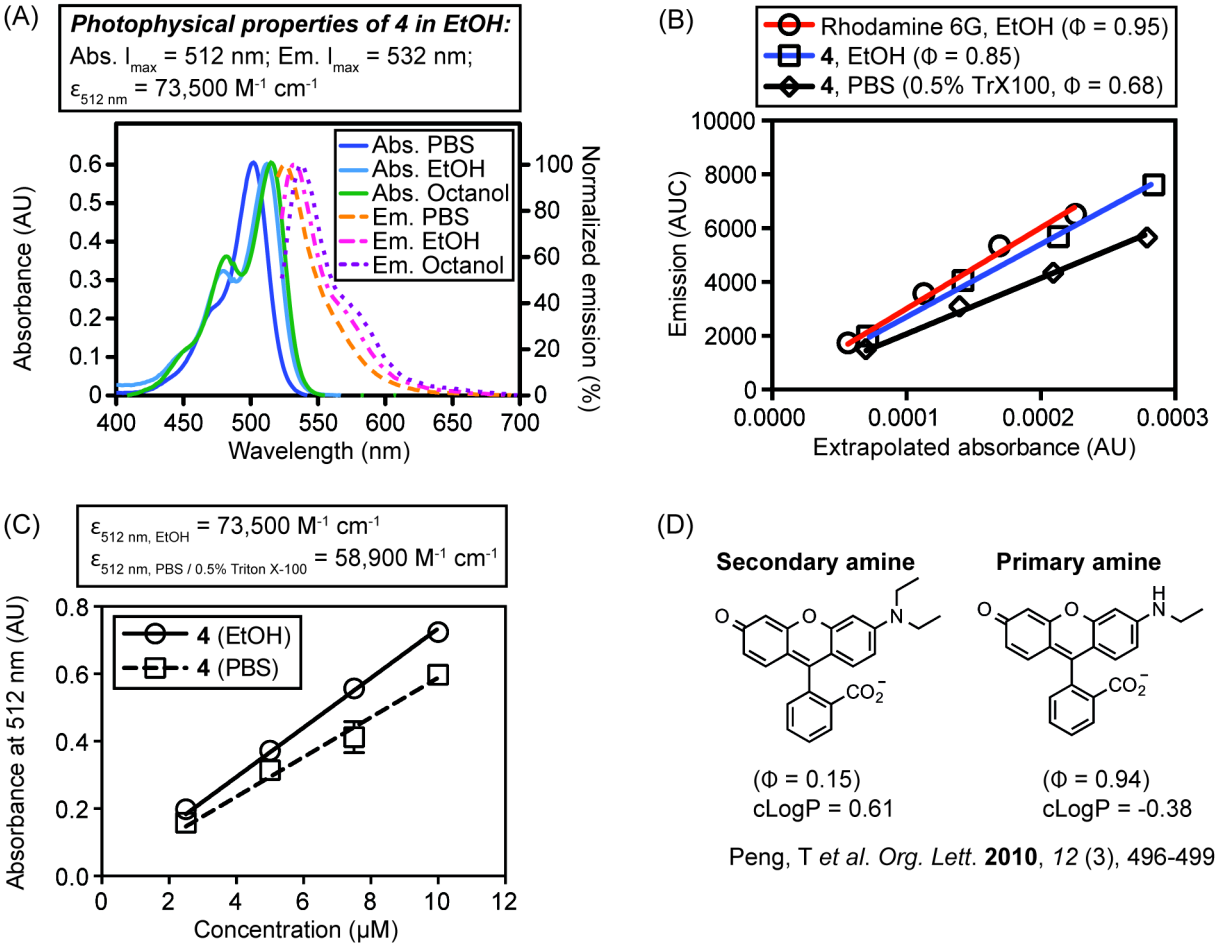

Figure 3.3. Photophysical properties of rhodol **4**. Panel A: Absorbance (Abs.) and normalized fluorescence emission (Em.) spectra in aqueous buffer (PBS, phosphate buffered saline, pH 7.4), absolute ethanol, and *n*-octanol. Absorbance spectra were acquired at a concentration of 10 μM. Emission spectra, acquired at a concentration of 10 nM, were obtained by excitation at 500 nm. Fluorescence emission intensities were normalized to 100% of Abs. l_{max}. Panel B: Determination of quantum yields of **4** in ethanol and PBS (pH 7.4, 0.5% Triton X-100) relative to rhodamine 6G in ethanol. Panel

C: Data and linear regression used to determine molar extinction coefficients of **4** in ethanol and PBS (pH 7.4) containing Triton X-100 (0.5%). Panel D: Structures of previously reported[55] rhodamines containing diethylamine and monoethylamine sidechains. The differences in quantum yield (Φ) are shown. cLogP values were calculated for the ionized form using ChemAxon Marvin Sketch 6.2.

3.4 Confocal Laser Scanning Microscopy of HeLa Cells Treated with Hydrophobic Fluorinated Rhodols

To examine the subcellular distribution of rhodol **4**, human HeLa cervical carcinoma cells were treated this compound and imaged by confocal laser scanning microscopy. As shown in Figure 3.4, these experiments revealed accumulation of **4** in distinct tubular structures. These structures were identified as the ER by colocalization with the spectrally orthogonal organelle marker ER Tracker Blue-White (Figure 3.4). Although the mechanism of the selectivity of fluorophores such as ER-Tracker Blue-White or **4** for the ER is not completely understood, QSAR[25, 56] and microscopy[29] studies of related probes suggest that these types of hydrophobic amphipathic compounds preferentially associate with the unique cholesterol-poor composition of ER membranes.[57]

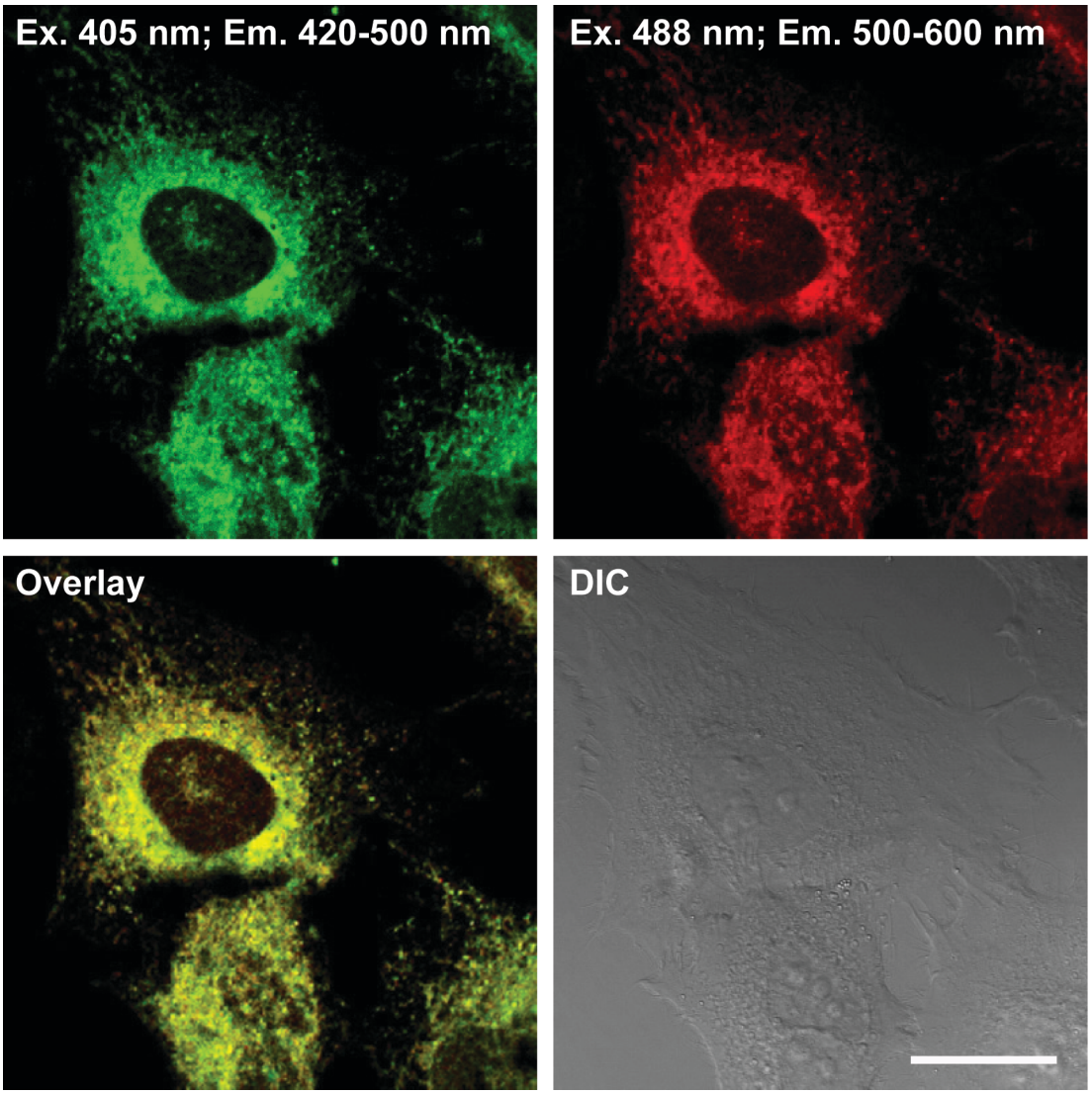

Figure 3.4. Confocal laser scanning and DIC micrographs of living HeLa cells treated with ER-tracker Blue-White DPX (0.1 μM, 0.5 h) and 4 (0.5 μM, 0.5 h). The fluorescence emission of ER-tracker Blue-White DPX can be observed in the upper left panel and the fluorescence emission of the spectrally orthogonal **4** can be observed in the upper right panel. Colocalization of these two fluorophores is shown in yellow in the lower left panel. Scale bar = 25 microns.

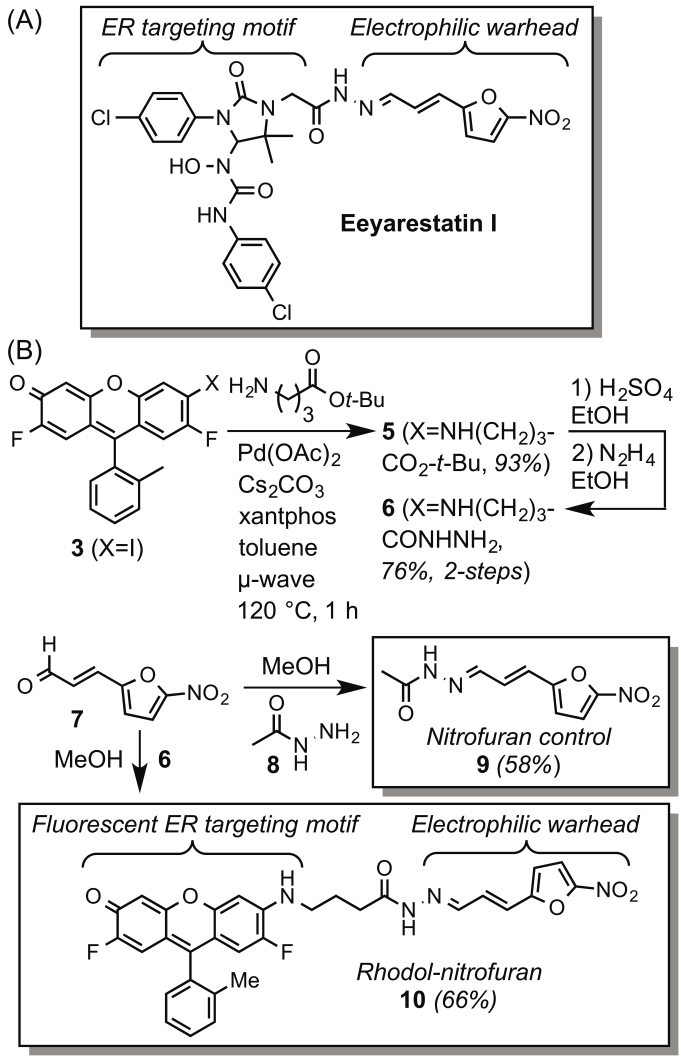

Figure 3.5. Panel A: Structure of eeyarestatin I. Panel B: Synthesis of the nitrofuran control **9** and the fluorinated rhodol-nitrofuran **10**.

3.5 Targeting the ERAD pathway with Fluorinated Hydrophobic Rhodols

Eeyarestatin I (Figure 3.5) exhibits cytotoxic activity by inhibiting the protein p97 in the ER. This agent was initially identified in a high throughput screen for compounds that interfere with the turnover of a MHC heavy chain protein fused to green fluorescent protein, a process that involves degradation of this protein by the proteasome.[18]

However, eeyarestatin I does not directly inhibit the proteasome, but instead blocks the upstream p97 complex of ER membranes.[19, 22] Eeyarestatin I was shown to directly interact with p97 through surface plasma resonance (SPR) studies, although the specific binding site on p97 remains unclear.[22] This complex translocates misfolded polypeptides from the ER to the cytosol for eventual degradation by the proteasome. Although its mechanism of action is not completely understood, eeyarestatin I is known to inhibit the deubiquitinating activity of p97-associated enzyme ataxin-3 (atx3),[19] block Sec61-mediated protein translocation at the ER,[21] affect vesicular transport,[23] activate of the UPR caused by accumulation of ubiquitinated poylpeptides,[58] and trigger ER-stress due to a build-up of misfolded proteins, thereby inducing apoptosis in some cancer cell lines.[20, 59] Previous structure-activity relationship studies of eeyarestatin I using SPR[22] demonstrated that the 5-nitrofuran-2-acrylaldehyde hydrazone functions as a warhead that physically interacts with the p97 complex, whereas the aryl urea moiety principally localizes this nitrofuran warhead to ER membranes to gain selectivity for ER-membrane-bound p97 over the cytosolic form of this protein. (2*E*)-3-(5-nitro-2-furanyl)-2-propenal and related compounds are electrophilic can be further bioactivated to form mutagenic reactive species.[56,57] Consequently, targeting of this group to the ER could potentially reduce its mutagenicity.

To investigate whether fluorinated hydrophobic rhodols might provide a platform for delivery of stress-inducing cargo to the ER, we designed compound **10** (Figure 3.5). This compound links the ER-targeting rhodol to the (2*E*)-3-(5-nitro-2-furanyl)-2-propenal hydrazone warhead found in eeyarestatin I. The nitrofuran derivative **9** was designed as an untargeted control. As shown in Figure 3.5, ester **5** was synthesized from iodoarene

3 and γ-aminobutyric acid *t*-butyl ester using Buchwald-Hartwig cross-coupling. This resulting ester was deprotected and converted to hydrazide **6**. Hydrazides **6** and **8** were subsequently condensed with aldehyde **7** to afford the nitrofuran derivatives **9** and **10**. To ensure that the ER-targeting ability of the rhodol was unaffected by attachment of the warhead, HeLa cells were treated with **10** and ER-Tracker Blue-White and analyzed by confocal laser scanning microscopy. Cellular imaging demonstrated that addition of the nitrofuran moiety did not affect localization of the rhodol to the ER (Figure 3.6). To compare the cytotoxicities of eeyarestatin I, **6**, **9** and **10**, HeLa cells were treated with these compounds for 48 h. The rhodol-nitrofuran **10** (IC_{50}= 2.7 μM) and eeyarestatin I (IC_{50} = 2.0 μM) were found to be similar in potency, indicating that the ER-targeting motifs of both of these compounds are effective at delivering the nitrofuran warhead to this organelle (Figure 3.7). As controls, hydrazide **6**, lacking the cytotoxic warhead, showed no appreciable toxicity (IC_{50} > 50 μM), whereas the nitrofuran warhead **9** alone was substantially less toxic (IC_{50} = 13 μM) than the ER-targeted compounds.

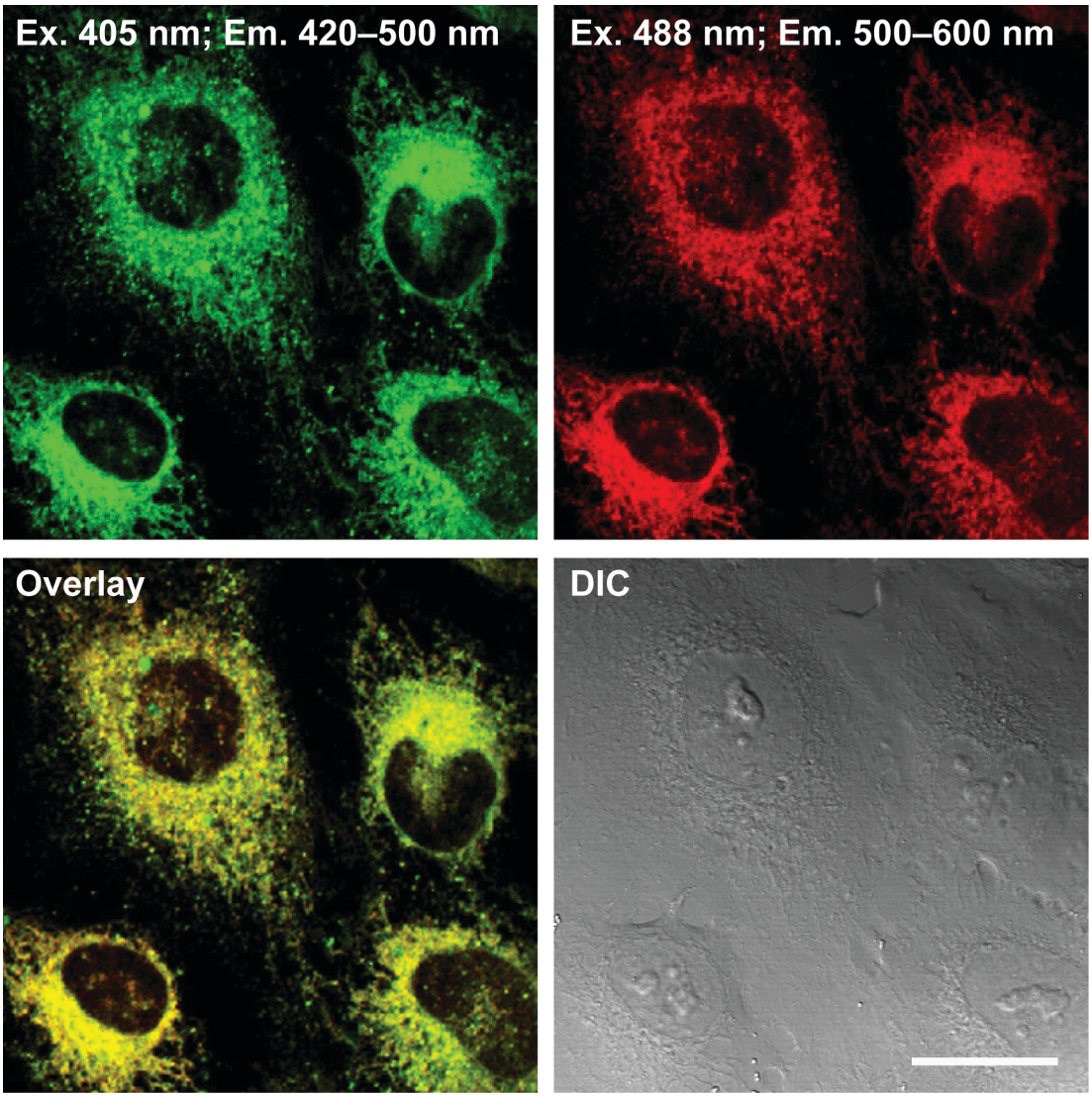

Figure 3.6. Confocal laser scanning and DIC micrographs of living HeLa cells treated with **10** (0.5 μM, 0.5 h) and ER-tracker Blue-White (0.1 μM, 0.5 h). The fluorescence emission of ER-tracker Blue-White DPX can be observed in the upper left panel, the fluorescence emission of **10** can be observed in the upper right panel. Colocalization of the two fluorophores is shown in yellow on the bottom left. Scale bar = 25 microns.

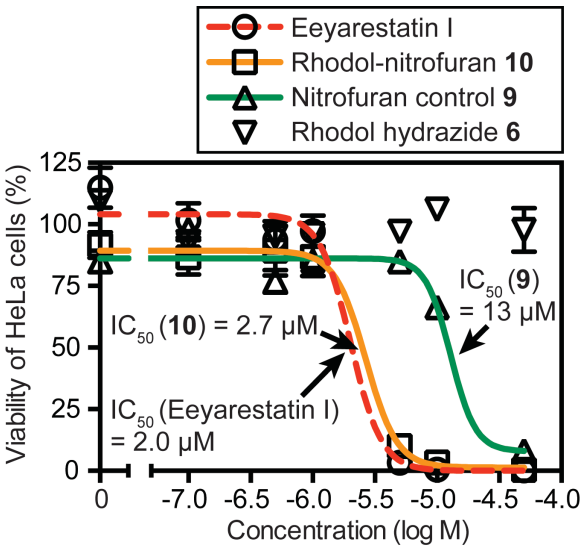

Figure 3.7. Cytotoxicity of eeyarestatin I, the ER-targeted rhodol-nitrofuran **10**, the nontargeted nitrofuran **9**, and the rhodol hydrazide **6** towards HeLa cells after 48 h in culture. Cellular viability was measured by flow cytometry using P.I. exclusion and light-scattering.

Eeyarestatin I blocks the UPS by inhibiting the p97 protein on ER membranes. This protein is required for maturation of the transcription factor Nrf1, which activates genes that encode subunits of the proteasome.[60] To characterize inhibitors of the UPS, cells are typically transfected with green or yellow fluorescent proteins fused to a ubiquitin degradation signal.[61-62] These proteins function as reporters because the fused ubiquitin results in trafficking to the proteasome, where they are rapidly degraded.[63] Pharmacological inhibitors of the proteasome such as MG132,[61, 64] bortezomib,[65] and epoxomicin[62] have been shown to prevent degradation of these reporter proteins and restore cellular fluorescence. Similarly, inhibition of the upstream ER-associated p97 protein by DBeQ,[66] eeyarestatin I,[66] and ML240/ML241[67] prevents their downstream degradation, thereby allowing their accumulation to observable levels.

To examine whether rhodol **10** inhibits the same pathway targeted by eeyarestatin I, we constructed a new fluorescent reporter. This reporter comprises a

G76V mutant of ubiquitin (Ub^{G76V})[61, 68] fused to the cyan fluorescent protein cerulean. The cyan fluorescence of this protein was chosen to provide spectral orthogonality to the yellow fluorescent rhodols. To validate this reporter, HeLa cells were transiently transfected with cerulean as a positive control (Figure 3.8, panel A) and Ub^{G76V}-cerulean as a reporter of UPS function (Figure 5, panels B-E). In the absence of inhibitors, cells transfected with the Ub^{G76V}-cerulean reporter showed no appreciable cellular fluorescence, consistent with rapid degradation of this protein by the proteasome (Figure 3.8). However, when these cells were treated for 12 h with the proteasome inhibitor bortezomib or the p97 inhibitor eeyarestatin I, the transfected cells became highly cyan fluorescent. Correspondingly, when treated with rhodol **10**, cerulean was highly expressed at levels essentially identical to cells treated with eeyarestatin I, demonstrating that **10** specifically inhibits the UPS. Importantly, when the untargeted nitrofuran control **9** was examined (Figure 3.8, Panel F), no appreciable fluorescence was observed suggesting the targeting motif of **10** is critical for activity. Based on its selective localization in the ER, and prior studies of the same warhead in eeyarestatin I, the effects of **10** on cellular proliferation and the UPS likely result from direct inhibition of p97.

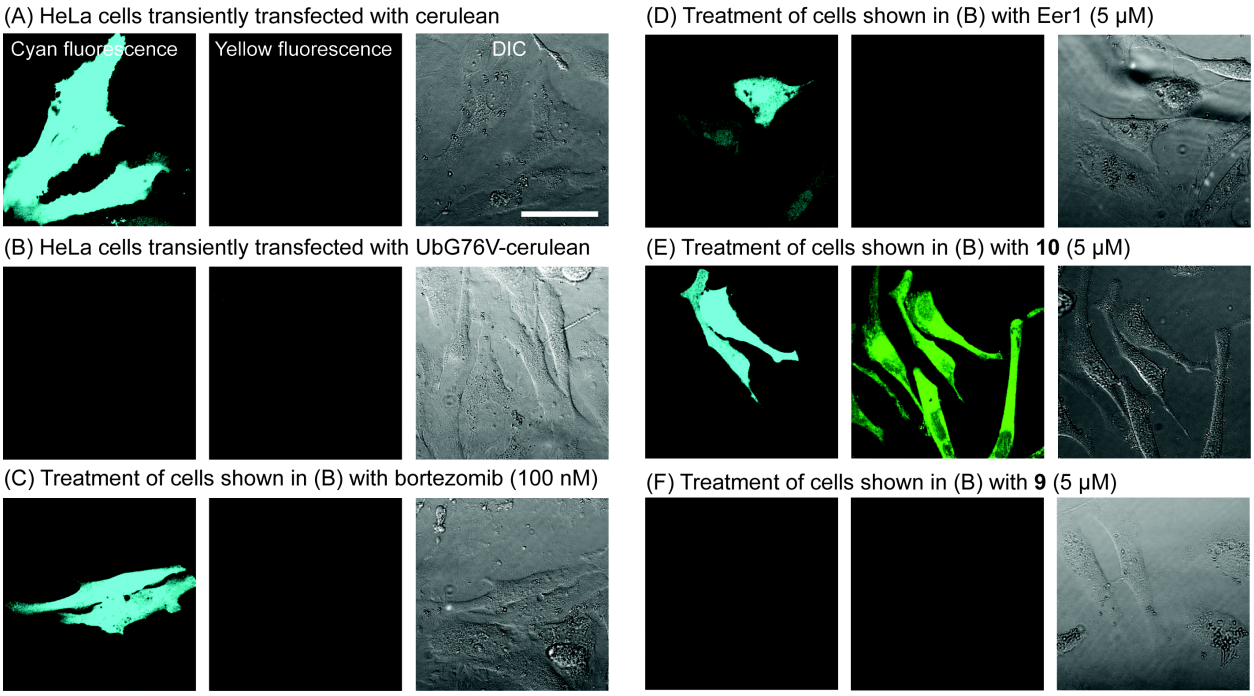

Figure 3.8. Confocal laser scanning and differential interference contrast (DIC) micrographs of living HeLa cells transiently transfected with the cyan fluorescent protein cerulean (panel A) as a positive control or Ub^{G76V}-cerulean (panels B-E) as a reporter of inhibition of the ubiquitin-proteasome system. Inhibition of the UPS prevents degradation of Ub^{G76V}-cerulean, resulting in cells expressing this cyan fluorescent protein. The fluorescence of cerulean can be observed in the cyan (left) channel and the spectrally orthogonal rhodol **10** can be observed in the yellow (middle) channel. The cyan fluorescence was generated by excitation with a 405 nm laser, and the yellow fluorescence was generated by excitation with a 532 nm laser. Cells were treated with vehicle (DMSO, 0.1%, panel B), bortezomib (100 nM), Eer1 (5 μM), **10** (5 μM), or **9** (5 μM) for 12 h prior to imaging by microscopy. Scale bar = 50 microns.

3.6 Conclusion

The results presented here demonstrate that a fluorinated hydrophobic rhodol can be used to selectively deliver biologically active cargo to the ER. When the cargo is a 5-nitrofuran warhead, delivery to the ER resulted in inhibition of the UPR, with concomitant effects on cellular proliferation. Given the widespread interest in targeting of ER-associated proteins for potential treatment of cancer[4, 69] neurodegeneration,[70] and other diseases,[71] these compounds may provide useful tools for the delivery of agents

designed to selectively modulate diverse biological pathways associated with this critical organelle.

3.7 Experimental Section

3.7.1 General. ^{1}H NMR and ^{13}C NMR spectra were acquired on Bruker DRX-400 or Avance AVIII 500 MHz instruments. Chemical shifts (d) are reported in ppm referenced to $CDCl_3$. ^{1}H coupling constants (J_{HH}, Hz) are reported as follows: chemical shift, multiplicity (br = broad, s = singlet, d = doublet, t = triplet, q = quartet, m = multiplet, dt = doublet of triplets, dt = doublet of quartets, dd = doublet of doublets), coupling constant, and integration. ^{13}C coupling constants (J_{CF}, Hz) are reported as follows: chemical shift, multiplicity (s = singlet, d = doublet, dd= doublet of doublet). Consistent with previously published studies of related compounds,[72-73] E/Z rotamers of hydrazones **9** and **10** were observed in ^{1}H and ^{13}C NMR spectra. Peaks from the major rotamer are reported in the characterization data. Infrared spectra (IR) were recorded with a Perkin-Elmer Spectrum 100 FT-IR spectrophotometer. Absorbance spectra were obtained using semimicro (1.5 mL) methacrylate cuvettes on an Aligent 8452A diode array spectrometer. Fluorescence spectra were acquired using semimicro (1.5 mL) methacrylate cuvettes and a Perkin-Elmer LS55 Fluorescence Spectrometer (10 nm excitation slit width). High Resolution mass spectra were obtained at the Mass Spectrometry Laboratory at the University of Kansas on a Micromass LCT Premier. Elemental analysis was performed by Midwest MicroLabs. Thin layer chromatography (TLC) was performed using EMD aluminum-backed (0.20 mm) silica plates (60 F-254), and flash chromatography used ICN silica

gel (200-400 mesh). TLC plates were visualized by UV lamp or staining with ceric sulfate/molybdic acid. All non-aqueous reactions were carried out using flame- or oven-dried glassware under an atmosphere of dry argon or nitrogen. Tetrahydrofuran (THF), dichloromethane (CH_2Cl_2), *N*,*N*-dimethylformamide (DMF), methanol (MeOH), ether (Et_2O), and triethylamine (TEA) were purified via filtration through two columns of activated basic alumina under an atmosphere of Ar using a solvent purification system from Pure Process Technology (GlassContour). Other commercial reagents were used as received unless otherwise noted. Eeyarestatin I was obtained from Tocris or Cayman Chemicals. Measurements for molar extinction coefficients and relative quantum yield were preformed using a SUPRASIL macro/semi micro quartz cuvette (PerkinElmer, B0631132). Molar extinction coefficients (ε) were calculated from Beer's Law plots of absorbance l_{max} versus concentration as shown in Figure S1. Linear least squares fitting of the data (including a zero intercept) was used to determine the slope (corresponding to ε). Values (M^{-1} cm^{-1}) were calculated as follows: Absorbance = ε [concentration (M)] L, where L = 1 cm. Relative quantum yields (Φ) in ethanol were determined by the method of Williams.[49] Fluorophores were excited at 488 nm and the integrated fluorescence emission (500 nm to 800 nm) was quantified (concentrations of 3.3 nM to 16.7 nM). Rhodamine 6G (Φ = 0.95 in ethanol) provided the standard.[74-76] The integrated fluorescence emission at a given concentration was plotted against the maximum absorbance of the sample at that concentration determined by extrapolation based on absorbance measurements at higher concentrations. Linear least squares fitting of the data (including a zero intercept) was used to calculate the slope, which is proportional to the quantum yield. Quantum yields were calculated as follows: Φ_x =

$\Phi_{st}(Grad_x/Grad_{st})(\eta^2_x/\eta^2_{st})$, where Φ_{st} represents the quantum yield of the standard, Φ_x represents the quantum yield of the unknown, *Grad* is the slope of the best linear fit, and η is the refractive index of the solvent used.

3.7.2 Cell Culture The HeLa (CCL-2) cell line was obtained from ATCC. Dulbecco's Modified Eagle Medium (DMEM, Sigma D5796) was supplemented with FBS (10%, Sigma F0926), penicillin (100 units/L), and streptomycin (100 µg/L, Sigma P4333).

3.7.3 Plasmids The plasmid encoding Ub^{G76V}-YFP was a gift from Nico Dantuma (Addgene plasmid # 11949).[62] The plasmid encoding cerulean-N1 was a gift from Michael Davidson & Dave Piston (Addgene plasmid # 54742). The open-reading frame encoding YFP in Ub^{G76V}-YFP was replaced with the open-reading frame of cerulean-N1 by digestion of both vectors with *NotI* and *AgeI* and subcloning to afford Ub^{G76V}-cerulean in the EGFP-N1 (Clontech) vector backbone bearing a kanamycin bacterial resistance marker.

3.7.4 Cellular Toxicity: HeLa cells were seeded on a 96-well plate in complete DMEM at 4000 cells / 100 µL / well 24 h prior to treatments. All compounds were serial diluted in DMSO and added to media to achieve a 1:1000 dilution factor (0.1% DMSO in each well). The original media was removed from all wells by aspiration and replaced with treatment media (150 µL) at the concentrations indicated. Plates were incubated for 48 h at 37 °C and cells were analyzed in triplicate. Following this incubation period, the

media was aspirated and wells were washed with PBS (phosphate-buffered saline, pH 7.4). Wells were further treated with trypsin EDTA solution (50 μL) at 37 °C for 5 min followed by complete DMEM (100 μL) containing propidium iodide (P.I., 4.5 μM). The total cell count for each well was determined by flow cytometry (Accuri C6 instrument) using light scattering and P.I.-negative gates to identify populations of live cells. Counts of viable cells for each treatment were used to generate dose-response curves that were fitted by non-linear regression (GraphPad Prism 6 software) to determine IC_{50} values.

3.7.5 Confocal Microscopy of Cells Treated with ER-Tracker Blue-White DPX: Prior to treatment with compounds, HeLa cells in DMEM were added to an 8-well cover glass slide (Idibi μ-Slide, 200 μL, 20,000 cells/well) and allowed to proliferate for 24 h. Compounds in DMSO stock solutions were diluted 1000-fold with complete media prior to addition to cells. Cells were imaged using a Leica SPE2 confocal laser-scanning microscope fitted with a 63X objective. Cells were treated (15 min, 37 °C) with ER-Tracker Blue-White DPX (500 nM) and rhodol fluorophores (500 nM). Cells were imaged without any additional washing steps. ER-Tracker Blue-White DPX was excited with a 405 nm laser and emitted photons were collected from 415 nm to 500 nm. Hydrophobic fluorinated rhodols were excited with a 488 nm laser and emitted photons were collected from 500 nm to 600 nm.

3.7.6 Ubiquitin Degradation Assays by Confocal Microscopy: HeLa cells in DMEM were added to an 8-well cover glass slide (Idibi μ-Slide, 200 μL, 10,000 cells/well) and

allowed to attach for 12 h. Cells were treated with X-tremeGene HP (Roche) according to the protocol of the manufacturer (30 µL of complex solution/well) for transient transfection of the plasmid Ub^{G76V}-cerulean as a reporter for protein degradation. Cerulean-N1 provided a positive control, and adjacent untransfected cells provided a negative control, for these experiments. After 24 h, the media was replaced with DMEM containing either vehicle or inhibitors (DMSO final concentration = 0.1%). Wells were incubated (12 hours, 37 °C) followed by washing with DMEM. Cells were imaged using a Leica SPE2 confocal laser-scanning microscope fitted with a 40X objective. Expressed cerulean was visualized by excitation with a 405 nm laser with emitted photons collected between 425 nm to 500 nm. Rhodol fluorphores were excited a 532 nm laser with emitted photons collected between 550 nm to 700 nm. Figure 5 shows representative fields of cells for each treatment.

3.7.7 Synthetic Procedures and Compound Characterization Data

2,7-Difluoro-6-iodo-9-(*o*-tolyl)-3*H*-xanthen-3-one (3). To a dry, argon-flushed round-bottomed flask was added Pennsylvania Green[37, 39] (**2**, 1000 mg, 2.95 mmol, 1.0 equiv) and *N*,*N*-bis(trifluoromethylsulfonyl)aniline. Anhydrous 1,4-dioxane (Sigma) was added (20 mL), followed by triethylamine (490 µL, 3.55 mmol, 1.2 eq). The flask was heated under Ar to 60 °C for 1 h. Conversion to the intermediate triflate was observed by TLC (eluent: MeOH/CH_2Cl_2, 1:20). The flask was removed from the oil bath and lithium iodide (1.184 g, 8.99 mmol, 3 eq) and a reflux condenser were added. The solution was refluxed for 4 h. The flask was cooled to room temperature (22 °C), aqueous NaOH (2 N,

5 mL) was added, and the solution was stirred 1 h. Water (60 mL) was added, giving rise to a product slurry that was stirred for 1 h. This slurry was chilled to 4 °C, filtered, and the product cake washed with cold water (3 x 20 mL) to give **7** containing residual 1,4-dioxane. This product cake was treated with diethyl ether (5 mL), stirred vigorously for 1 min, and hexanes (5 mL) were added. The resulting slurry was filtered and the product cake extensively dried under high vacuum to provide **7** (1.123 g, 85%) as an orange solid. ^{1}H NMR (400 MHz, $CDCl_3$) δ 7.97 (d, *J* = 5.1 Hz, 1H), 7.52 (td, *J* = 7.6, 1.4 Hz, 1H), 7.42 (dd, *J* = 14.9, 7.4 Hz, 2H), 7.14 (dd, *J* = 7.6, 1.4 Hz, 1H), 6.69 (d, *J* = 7.8 Hz, 1H), 6.65 – 6.52 (m, 2H), 2.08 (s, 3H). ^{13}C NMR (126 MHz, $CDCl_3$) δ 176.75 (d, *J* = 21.1 Hz), 159.21, 157.80, 157.27, 156.79 (d, *J* = 1.8 Hz), 155.65, 147.94, 136.01 , 131.24 , 131.08 , 130.28 , 128.89 , 127.87 , 127.85 , 126.66 , 121.28 (dd, *J* = 48.3, 8.1 Hz), 110.94 (dd, *J* = 308.0, 27.7 Hz), 107.02 , 87.75 (d, *J* = 30.5 Hz), 19.64 . IR n_{max}: 3030, 1647, 1620, 1561, 1477, 1407, 1362, 1165, 1010, 751. HRMS (ESI) for $C_{20}H_{11}F_2IO_2$ ($M+H^+$): calcd 448.9845, Found: 448.9855.

2,7-Difluoro-6-((2-methoxyethyl)amino)-9-(*o*-tolyl)-3*H*-xanthen-3-one (4). An oven-dried microwave vial (10 mL) was charged with **3** (100 mg, 0.22 mmol, 1 eq), 2-methoxyethylamine (0.34 mmol, 1.5 eq), $Pd(OAc)_2$ (5 mg, 0.02 mmol, 0.1 eq), xantphos (19 mg, 0.03 mmol, 0.15 equiv) and Cs_2CO_3 (219 mg, 0.42 mmol, 2 eq). The vial was slowly flushed with argon after which anhydrous, degassed toluene (5 mL) was added. The vial was sealed and heated to 120 °C in a microwave reactor for 1 h. The reaction tube was cooled to room temperature and diluted with CH_2Cl_2 (25 mL). Water (15 mL) was added, and the organic layer was separated. The aqueous portion was extracted (2

x 15 mL) with CH_2Cl_2 and the organic layers combined and dried over anhydrous Na_2SO_4. The organic solvents were removed under reduced pressure, and the crude product was purified by silica gel column chromatography (eluent: CH_2Cl_2 to MeOH/CH_2Cl_2, 1:20) to afford **4** as a red solid (93 mg, 78% yield). ^{1}H NMR (500 MHz, $CDCl_3$) δ 7.47 (td, *J* = 7.6, 1.4 Hz, 1H), 7.45 – 7.34 (m, 2H), 7.13 (dd, *J* = 7.6, 1.5 Hz, 1H), 6.73 (d, *J* = 7.0 Hz, 1H), 6.68 – 6.56 (m, 3H), 5.19 (q, *J* = 5.0 Hz, 1H), 3.69 (dd, *J* = 5.6, 4.6 Hz, 2H), 3.47 (q, *J* = 5.2 Hz, 3H), 3.42 (s, 3H), 2.06 (s, 3H). ^{13}C NMR (126 MHz, $CDCl_3$) δ 175.58 (d, *J* = 19.9 Hz), 157.44 (d, *J* = 263.7 Hz), 156.33 (d, *J* = 262.5 Hz), 155.29, 151.84, 150.73 (d, *J* = 12.0 Hz), 149.47, 147.55, 142.75 (d, *J* = 14.4 Hz), 135.90, 132.34, 130.76, 129.75, 128.81, 126.28, 112.66 (dd, *J* = 652.32, 8.4 Hz), 111.26 (d, *J* = 21.5 Hz), 109.93 (d, *J* = 22.2 Hz), 106.24 (d, *J* = 5.4 Hz), 97.35 (d, *J* = 3.5 Hz), 70.01, 59.03, 42.83, 19.57. IR n_{max}: 3279, 2933, 1729, 1655, 1613, 1597, 1543, 1501, 1485, 1452, 1366, 1301, 1178, 1104, 751. HRMS (ESI) for $C_{23}H_{19}F_2NO_3$ ($M+H^+$): calcd 396.1406, Found: 396.1390.

***tert*-Butyl 4-((2,7-difluoro-3-oxo-9-(*o*-tolyl)-3*H*-xanthen-6-yl)amino)butanoate (5**). An oven-dried microwave vial (10 mL) was charged with **3** (100 mg, 0.22 mmol, 1 eq), γ-aminobutyric acid *t*-butyl ester hydrochloride (0.34 mmol, 1.5 eq), $Pd(OAc)_2$ (5 mg, 0.02 mmol, 0.1 eq), xantphos (19 mg, 0.03 mmol, 0.15 equiv) and Cs_2CO_3 (329 mg, 0.63 mmol, 3 eq). The vial was slowly flushed with argon after which anhydrous, degassed toluene (5 mL) was added. The vial was sealed and heated to 120 °C in a microwave reactor for 1 h. The reaction tube was cooled to room temperature and diluted with CH_2Cl_2 (25 mL). Water (15 mL) was added and the organic layer was

separated. The aqueous portion was extracted (2 x 15 mL) with CH_2Cl_2, and the organic layers were combined and dried over anhydrous Na_2SO_4. The organic solvents were removed under reduced pressure, and the crude product was purified by silica gel column chromatography (eluent: CH_2Cl_2 to MeOH:CH_2Cl_2, 1:20) to provide **5** as a red solid (99 mg, 93%). ^{1}H NMR (500 MHz, $CDCl_3$) δ 7.40 (td, *J* = 7.6, 1.2 Hz, 1H), 7.36 – 7.28 (m, 2H), 7.06 (d, *J* = 7.4 Hz, 1H), 6.66 (d, *J* = 7.1 Hz, 1H), 6.59 – 6.47 (m, 3H), 5.23 – 5.18 (1H), 3.30 (q, *J* = 6.7 Hz, 2H), 2.34 (t, *J* = 6.8 Hz, 2H), 2.03 – 1.90 (m, 2H), 1.99 (s, 3H), 1.40 (s, 9H). ^{13}C NMR (126 MHz, $CDCl_3$) δ 172.58, 175.53 (d, *J* = 19.9 Hz), 157.41, 156.32 (d, *J* = 262.2 Hz), 151.99, 150.79 (d, *J* = 8.6 Hz), 149.40, 147.48, 142.84 (d, *J* = 14.3 Hz), 135.89, 132.36, 130.75, 129.73, 128.80, 126.27, 112.55 (dd, *J* = 666.38, 8.33 Hz), 110.58 (dd, *J* = 155.58, 21.49 Hz), 106.22 (d, *J* = 5.4 Hz), 97.02 (d, *J* = 3.4 Hz), 81.15, 42.93, 32.88, 28.09, 23.73, 19.56. IR n_{max}: 3223, 2927, 1725, 1649, 1609, 1543, 1483, 1361, 1303, 1146, 1050, 835, 756. HRMS (ESI) for $C_{28}H_{27}F_2NO_4$ ($M+H^+$): calcd 480.1981, Found: 480.1963.

4-((2,7-Difluoro-3-oxo-9-(*o*-tolyl)-3*H*-xanthen-6-yl)amino)butanehydrazide (6). To a dry flask containing 5 (73 mg, 0.15 mmol), was added absolute ethanol (1.5 mL). Catalytic sulfuric acid (1 drop) was added to the homogeneous solution, and the flask was refluxed overnight (16 h). The flask was cooled to room temperature and the excess ethanol removed under reduced pressure. The crude reaction mixture was passed through a plug of silica with MeOH;CH_2Cl_2 (1:20) as the eluent. The resulting solution was concentrated under reduced pressure and dried under high vacuum to give the corresponding ethyl ester (68 mg, 99%). HRMS (ESI) for $C_{26}H_{23}F_2NO_4$ ($M+H^+$):

calcd 452.1668, Found: 452.1686. This product carried on to the subsequent step without further purification. To a dry flask containing the intermediate ethyl ester (62 mg, 0.14 mmol, 1 eq), absolute ethanol (0.5 mL) was added. Hydrazine monohydrate (41 mg, 0.83 mmol, 6 eq) was added to the solution and the flask sealed under nitrogen. The reaction was stirred overnight (16 h) at which point complete conversion of the ester to the hydrazide was observed by TLC (eluent: MeOH/CH_2Cl_2, 1:9). The product was purified by silica chromatography, eluting with MeOH/CH_2Cl_2 (1:9), to afford compound 6 as a dark red solid (46 mg, 0.11 mmol, 77%). ^{1}H NMR (400 MHz, $CDCl_3$) δ 7.49 – 7.40 (m, 1H), 7.40 – 7.32 (m, 2H), 7.08 (d, *J* = 7.4 Hz, 1H), 6.70 (d, *J* = 7.0 Hz, 1H), 6.65 – 6.55 (m, 3H), 3.32 (t, *J* = 6.7 Hz, 2H), 2.31 (t, *J* = 6.8 Hz, 2H), 2.02 (m, *J* = 7.6 Hz, 5H). ^{13}C NMR (126 MHz, 9:1 $CDCl_3$ / CD_3OD) δ 175.21 (d, *J* = 19.9 Hz), 173.39, 157.54, 156.10 (d, *J* = 260.4 Hz), 152.59, 148.74 (d, *J*= 243.18 Hz), 143.72 (d, *J* = 14.6 Hz), 145.78, 132.17, 130.76, 129.84, 127.46 (d, J= 307.44 Hz), 114.44 (d, *J* = 8.3 Hz), 111.10 (d, *J* = 21.4 Hz), 110.31 (d, *J* = 22.2 Hz), 110.02 (d, *J* = 8.4 Hz), 105.86 (d, *J* = 5.2 Hz), 96.63 (d, *J* = 4.0 Hz), 42.69, 31.29, 23.81, 19.49. IR n_{max}: 3246, 2927, 1651, 1610, 1610, 1540, 1485, 1335, 1303, 1179, 960, 751. HRMS (ESI) for $C_{24}H_{21}F_2N_3O_3$ ($M+H^+$): calcd 438.1624, Found: 438.1621

(2*E*)-3-(5-nitro-2-furanyl)-2-propenal **(7).** This known[77] compound was prepared by refluxing (triphenylphosphoranylidene)acetylaldehyde (1186 mg, 3.89 mmol, 1.1 eq) and 5-nitrofurylaldehyde (500 mg, 3.54 mmol, 1 eq) in dry toluene (10 mL) under argon for 6 h. During the course of the reaction, ^{1}H NMR spectra of crude reaction mixtures in $CDCl_3$ were used to monitor enrichment of the E isomer (10.5 ppm) over the Z isomer

(9.7 ppm) over time. The reaction was cooled to room temperature and diluted with CH_2Cl_2 (50 mL) and water (30 mL). The organic layer was separated and the aqueous layer was extracted with CH_2Cl_2 (2 x 50 mL). The organic layers were pooled, dried over anhydrous Na_2SO_4, and concentrated under reduced pressure. The product was purified by silica chromatography (eluent: EtOAc/hexane, 1:4) to give 7 as a light brown solid (554 mg, 93%). ^{1}H NMR (400 MHz, $CDCl_3$) δ 9.69 (d, *J* = 7.4 Hz, 1H), 7.37 (d, *J* = 3.8 Hz, 1H), 7.26 (d, *J* = 16.0 Hz, 1H), 6.93 (d, *J* = 3.8 Hz, 1H), 6.80 (dd, *J* = 16.0, 7.4 Hz, 1H). ^{13}C NMR (126 MHz, CDCl3) δ 191.72, 152.73, 151.86, 134.50, 130.90, 116.59, 112.93. IR n_{max}: 3152, 1671, 1630, 1518, 1470, 1348, 1237, 1109, 979, 812, 737. Anal. Calcd for $C_7H_5NO_4$: C, 50.31; H, 3.02; N, 8.38. Found C, 50.41; H, 2.96; N, 8.29.

***N*'-((1*E*,2*E*)-3-(5-Nitrofuran-2-yl)allylidene)acetohydrazide (9).** Compound **7** (50 mg, 0.30 mmol, 1 eq) and acetic hydrazide (28.8 mg, 0.39 mmol, 1.3 eq) were charged into a dry flask. The solids were treated with methanol (1 mL) and stirred for 1 h, after which the crude product precipitated as a yellow solid. The reaction mixture is filtered and the crude solid product was further purified by silica gel chromatography (eluent: MeOH/CH_2Cl_2, 1:20). The product was dried under high vacuum to give **7** (35 mg, 58%) as a yellow solid. ^{1}H NMR (500 MHz, 9:1 $CDCl_3$: CD_3OD) δ 7.52 (d, *J* = 9.5 Hz, 1H), 7.30 (m, 1H), 7.10 – 6.98 (m, 1H), 6.64 – 6.51 (m, 2H), 2.23 (s, 3H). ^{13}C NMR (126 MHz, 9:1 $CDCl_3$: CD_3OD) δ 174.06, 154.26, 146.36, 143.39, 130.09, 122.67, 113.77, 112.35, 20.20. IR n_{max}: 3110, 2972, 1672, 1506, 1464, 1387, 1334, 1258, 1141, 1025, 959, 736. HRMS (ESI) for $C_9H_9N_3O_4$ 246.0491 Found 246.0467

4-((2,7-Difluoro-3-oxo-9-(*o*-tolyl)-3*H*-xanthen-6-yl)amino)-*N*'-((1*E*,2*E*)-3-(5-nitrofuran-2-yl)allylidene)butanehydrazide (10). Hydrazide **6** (30 mg, 0.07 mmol) and aldehyde **7** (13 mg, 0.75 mmol) were placed in a dry flask. Dry methanol (0.5 mL) was added and reaction stirred at room temperature for 1 h. Formation of the product and consumption of the hydrazide, was observed by TLC (eluent: MeOH:CH_2Cl_2, 1:19). Excess methanol was removed under reduced pressure and the crude mixture purified with a silica column (eluent: MeOH/CH_2Cl_2, 1:19). The product was dried under high vacuum to afford **9** as a red solid (26 mg, 66%). ^{1}H NMR (500 MHz, 9:1 $CDCl_3$: CD_3OD) δ 7.57 (d, *J* = 9.5 Hz, 1H), 7.42 (t, *J* = 7.5 Hz, 1H), 7.36 – 7.27 (m, 3H), 7.03 (tdd, *J* = 25.5, 15.0, 9.6 Hz, 5H), 6.72 (dd, *J* = 11.7, 7.0 Hz, 1H), 6.59 (ddd, *J* = 21.7, 12.2, 6.3 Hz, 11H), 3.36 – 3.28 (m, 14H), 2.79 (q, *J* = 9.0, 6.3 Hz, 1H), 2.41 (t, *J* = 6.7 Hz, 1H), 2.09 – 2.02 (m, 2H), 1.97 (s, 3H). ^{13}C NMR (126 MHz, 9:1 $CDCl_3$: CD_3OD) δ 175.42, 175.00 (d, *J* = 19.0 Hz), 157.55, 157.00 (d, *J* = 260.9 Hz), 155.97 (d, *J* = 260.9 Hz), 154.09, 152.75, 151.73, 148.80 (d, *J* = 247.4 Hz), 144.10, 135.69, 132.04, 130.73, 129.85, 129.74, 128.59, 126.20, 122.96, 113.83, 112.69, 111.11 (dd, *J* = 89.4, 21.5 Hz), 112.14 (dd, *J* = 518.3, 8.5 Hz), 110.74 (dd, *J* = 89.4, 21.5 Hz), 105.68 (d, *J* = 5.1 Hz), 96.63, 96.43, 42.62, 31.75, 23.81, 19.40. IR n_{max}: 2931, 1675, 1651, 1611, 1541, 1484, 1461, 1335, 1299, 1178, 1125, 1105, 959, 735. HRMS (ESI) for $C_{31}H_{25}F_2N_4O_6$ ($M+H^+$): calcd 587.1737, Found: 587.1724.

3.8 References

1. Vance, J. E., Phospholipid Synthesis and Transport in Mammalian Cells. *Traffic* **2015,** *16* (1), 1-18.

2. Sovolyova, N.; Healy, S.; Samali, A.; Logue, S. E., Stressed to death--mechanisms of ER stress-induced cell death. *Biol. Chem.* **2014,** *395* (1), 1-13.

3. Tabas, I.; Ron, D., Integrating the mechanisms of apoptosis induced by endoplasmic reticulum stress. *Nat. Cell Biol.* **2011,** *13* (3), 184-190.

4. Deshaies, R. J., Proteotoxic crisis, the ubiquitin-proteasome system, and cancer therapy. *BMC Biol.* **2014,** *12*, 94.

5. Shore, G. C.; Papa, F. R.; Oakes, S. A., Signaling cell death from the endoplasmic reticulum stress response. *Current opinion in cell biology* **2011,** *23* (2), 143-149.

6. Kim, I.; Xu, W.; Reed, J. C., Cell death and endoplasmic reticulum stress: disease relevance and therapeutic opportunities. *Nat. Rev. Drug Disc.* **2008,** *7* (12), 1013-1030.

7. Lin, J. H.; Walter, P.; Yen, T. S., Endoplasmic reticulum stress in disease pathogenesis. *Ann. Rev. Pathol.* **2008,** *3*, 399-425.

8. Banerjee, A.; Lang, J. Y.; Hung, M. C.; Sengupta, K.; Banerjee, S. K.; Baksi, K.; Banerjee, D. K., Unfolded Protein Response Is Required in nu/nu Mice Microvasculature for Treating Breast Tumor with Tunicamycin. *J. Biol. Chem.* **2011,** *286* (33), 29127-29138.

9. Shiraishi, T.; Yoshida, T.; Nakata, S.; Horinaka, M.; Wakada, N.; Mizutani, Y.; Miki, T.; Sakai, T., Tunicamycin enhances tumor necrosis factor-related apoptosis-inducing ligand-induced apoptosis in human prostate cancer. *Cancer Res.* **2005,** *65* (14), 6364-6370.

10. Shao, R. G.; Shimizu, T.; Pommier, Y., Brefeldin A is a potent inducer of apoptosis in human cancer cells independently of p53. *Exp. Cell. Res.* **1996,** *227* (2), 190-196.

11. Chapman, J. R.; Tazaki, H.; Mallouh, C.; Konno, S., Brefeldin A induced apoptosis in prostatic cancer DU-145 cells: a possible p53-independent death pathway. *BJU Int* **1999,** *83* (6), 703-708.

12. Lin, W. C.; Chuang, Y. C.; Chang, Y. S.; Lai, M. D.; Teng, Y. N.; Su, I. J.; Wang, C. C. C.; Lee, K. H.; Hung, J. H., Endoplasmic Reticulum Stress Stimulates p53 Expression through NF-kappa B Activation. *PLoS ONE* **2012,** *7* (7), e39120.

13. Park, H. R.; Furihata, K.; Hayakawa, Y.; Shin-ya, K., Versipelostatin, a novel GRP78/Bip molecular chaperone down-regulator of microbial origin. *Tetrahedron Lett.* **2002,** *43* (39), 6941-6945.

14. Saito, S.; Tomida, A., Use of Chemical Genomics in Assessment of the UPR. *Methods Enzymol.* **2011,** *491*, 327-341.

15. Park, H. R.; Tomida, A.; Sato, S.; Tsukumo, Y.; Yun, J.; Yamori, T.; Hayakawa, Y.; Tsuruo, T.; Shin-Ya, K., Effect on tumor cells of blocking survival response to glucose deprivation. *J. Natl. Cancer Inst.* **2004,** *96* (17), 1300-1310.

16. Fels, D. R.; Ye, J.; Segan, A. T.; Kridel, S. J.; Spiotto, M.; Olson, M.; Koong, A. C.; Koumenis, C., Preferential cytotoxicity of bortezomib toward hypoxic tumor cells via overactivation of endoplasmic reticulum stress pathways. *Cancer. Res.* **2008,** *68* (22), 9323-9230.

17. Obeng, E. A.; Carlson, L. M.; Gutman, D. M.; Harrington, W. J., Jr.; Lee, K. P.; Boise, L. H., Proteasome inhibitors induce a terminal unfolded protein response in multiple myeloma cells. *Blood* **2006,** *107* (12), 4907-4916.

18. Fiebiger, E.; Hirsch, C.; Vyas, J. M.; Gordon, E.; Ploegh, H. L.; Tortorella, D., Dissection of the dislocation pathway for type I membrane proteins with a new small molecule inhibitor, eeyarestatin. *Mol. Biol. Cell* **2004,** *15* (4), 1635-1646.

19. Wang, Q.; Li, L.; Ye, Y., Inhibition of p97-dependent Protein Degradation by Eeyarestatin I. *J. Biol. Chem.* **2008,** *283* (12), 7445-7454.

20. Wang, Q.; Mora-Jensen, H.; Weniger, M. A.; Perez-Galan, P.; Wolford, C.; Hai, T.; Ron, D.; Chen, W.; Trenkle, W.; Wiestner, A.; Ye, Y., ERAD inhibitors integrate ER stress with an epigenetic mechanism to activate BH3-only protein NOXA in cancer cells. *Proc. Natl. Acad. Sci. U.S.A.* **2009,** *106* (7), 2200-2205.

21. Cross, B. C.; McKibbin, C.; Callan, A. C.; Roboti, P.; Piacenti, M.; Rabu, C.; Wilson, C. M.; Whitehead, R.; Flitsch, S. L.; Pool, M. R.; High, S.; Swanton, E., Eeyarestatin I inhibits Sec61-mediated protein translocation at the endoplasmic reticulum. *J. Cell Sci.* **2009,** *122* (Pt 23), 4393-4400.

22. Wang, Q.; Shinkre, B. A.; Lee, J.-g.; Weniger, M. A.; Liu, Y.; Chen, W.; Wiestner, A.; Trenkle, W. C.; Ye, Y., The ERAD Inhibitor Eeyarestatin I Is a Bifunctional Compound with a Membrane-Binding Domain and a p97/VCP Inhibitory Group. *PLoS ONE* **2010,** *5* (11), e15479.

23. Aletrari, M. O.; McKibbin, C.; Williams, H.; Pawar, V.; Pietroni, P.; Lord, J. M.; Flitsch, S. L.; Whitehead, R.; Swanton, E.; High, S.; Spooner, R. A., Eeyarestatin 1 interferes with both retrograde and anterograde intracellular trafficking pathways. *PLoS One* **2011,** *6* (7), e22713.

24. Brem, G. J.; Mylonas, I.; Bruning, A., Eeyarestatin causes cervical cancer cell sensitization to bortezomib treatment by augmenting ER stress and CHOP expression. *Gynecologic oncology* **2013,** *128* (2), 383-390.

25. Colston, J.; Horobin, R.; Rashid-Doubell, F.; Pediani, J.; Johal, K. K., Why fluorescent probes for endoplasmic reticulum are selective: an experimental and QSAR-modelling study. *Biotechnic Histochem.* **2003,** *78* (6), 323-332.

26. Lavis, L. D.; Raines, R. T., Bright building blocks for chemical biology. *ACS chemical biology* **2014,** *9* (4), 855-866.

27. Cole, L.; Davies, D.; Hyde, J.; Ashford, A. E., ER-Tracker dye and BODIPY-brefeldin A differentiate the endoplasmic reticulum and Golgi bodies from the tubular-vacuole system in living hyphae of Pisolithus tinctorius. *J. Microscopy* **2000,** *197* (3), 239-249.

28. Yang, Z.; He, Y.; Lee, J. H.; Chae, W.-S.; Ren, W. X.; Lee, J. H.; Kang, C.; Kim, J. S., A Nile Red/BODIPY-based bimodal probe sensitive to changes in the micropolarity and microviscosity of the endoplasmic reticulum. *Chem. Commun.* **2014,** *50* (79), 11672-11675.

29. Terasaki, M.; Song, J.; Wong, J. R.; Weiss, M. J.; Chen, L. B., Localization of endoplasmic reticulum in living and glutaraldehyde-fixed cells with fluorescent dyes. *Cell* **1984,** *38* (1), 101-108.

30. van Meer, G.; de Kroon, A. I. P. M., Lipid map of the mammalian cell. *J. Cell. Sci.* **2011,** *124* (1), 5-8.

31. Lange, Y.; Ye, J.; Rigney, M.; Steck, T. L., Regulation of endoplasmic reticulum cholesterol by plasma membrane cholesterol. *J. Lipid Res.* **1999,** *40* (12), 2264-2270.

32. Maxfield, F. R.; Mesmin, B.; Pipalia, N.; Lamlal, T.; Eliezer, D., Intracellular cholesterol transport. *FASEB J.* **2011,** *25*.

33. van Meer, G.; de Kroon, A. I. P. M., Lipid map of the mammalian cell. *J. Cell Sci.* **2011,** *124* (1), 5-8.

34. Zhou, M.; He, H.-J.; Suzuki, R.; Liu, K.-X.; Tanaka, O.; Sekiguchi, M.; Itoh, H.; Kawahara, K.; Abe, H., Localization of Sulfonylurea Receptor Subunits, SUR2A and SUR2B, in Rat Heart. *J. Histochem. Cytochem.* **2007,** *55* (8), 795-804.

35. Nelson, T. Y.; Gaines, K. L.; Rajan, A. S.; Berg, M.; Boyd, A. E., Increased cytosolic calcium. A signal for sulfonylurea-stimulated insulin release from beta cells. *J. Biol. Chem.* **1987,** *262* (6), 2608-2612.

36. Woydziak, Z. R.; Fu, L.; Peterson, B. R., Synthesis of fluorinated benzophenones, xanthones, acridones, and thioxanthones by iterative nucleophilic aromatic substitution. *J. Org. Chem.* **2012,** *77* (1), 473-481.

37. Woydziak, Z. R.; Fu, L.; Peterson, B. R., Efficient and Scalable Synthesis of 4-Carboxy-Pennsylvania Green Methyl Ester: A Hydrophobic Building Block for Fluorescent Molecular Probes *Synthesis-Stuttgart* **2014,** *46*, 158-164.

38. Mottram, L. F.; Maddox, E.; Schwab, M.; Beaufils, F.; Peterson, B. R., A concise synthesis of the Pennsylvania Green fluorophore and labeling of intracellular targets with O6-benzylguanine derivatives. *Org. Lett.* **2007,** *9* (19), 3741-3744.

39. Mottram, L. F.; Boonyarattanakalin, S.; Kovel, R. E.; Peterson, B. R., The Pennsylvania Green Fluorophore: A Hybrid of Oregon Green and Tokyo Green for the Construction of Hydrophobic and pH-Insensitive Molecular Probes. *Org. Lett.* **2006,** *8* (4), 581-584.

40. Peng, T.; Yang, D., Construction of a library of rhodol fluorophores for developing new fluorescent probes. *Org. Lett.* **2010,** *12* (3), 496-499.

41. Grimm, J. B.; Lavis, L. D., Synthesis of Rhodamines from Fluoresceins Using Pd-Catalyzed C–N Cross-Coupling. *Org. Lett.* **2011,** *13* (24), 6354-6357.

42. Wang, T.; Magnin, D. R.; Hamann, L. G., Palladium-catalyzed microwave-assisted amination of 1-bromonaphthalenes and 5- and 8-bromoquinolines. *Org. Lett.* **2003,** *5* (6), 897-900.

43. Jensen, T. A.; Liang, X. F.; Tanner, D.; Skjaerbaek, N., Rapid and efficient microwave-assisted synthesis of aryl aminobenzophenones using Pd-catalyzed Amination. *J. Org. Chem.* **2004,** *69* (15), 4936-4947.

44. Whitaker, J. E.; Haugland, R. P.; Ryan, D.; Hewitt, P. C.; Prendergast, F. G., Fluorescent rhodol derivatives: versatile, photostable labels and tracers. *Anal. Biochem.* **1992,** *207* (2), 267-279.

45. Peng, T.; Yang, D., HKGreen-3: a rhodol-based fluorescent probe for peroxynitrite. *Org. Lett.* **2010,** *12* (21), 4932-4935.

46. Li, J.; Yao, S. Q., "Singapore Green": a new fluorescent dye for microarray and bioimaging applications. *Org. Lett.* **2009,** *11* (2), 405-408.

47. Komatsu, H.; Harada, H.; Tanabe, K.; Hiraoka, M.; Nishimoto, S., Indolequinone-rhodol conjugate as a fluorescent probe for hypoxic cells: enzymatic activation and fluorescence properties. *Medchemcomm* **2010,** *1* (1), 50-53.

48. Dodani, S. C.; Firl, A.; Chan, J.; Nam, C. I.; Aron, A. T.; Onak, C. S.; Ramos-Torres, K. M.; Paek, J.; Webster, C. M.; Feller, M. B.; Chang, C. J., Copper is an endogenous

modulator of neural circuit spontaneous activity. *Proc. Natl. Acad. Sci. U.S.A.* **2014,** *111* (46), 16280-16285.

49. Williams, A. T.; Winfield, S. A., Relative Fluorescence Quantum Yields Using a Computer-controlled Luminescence Spectrometer. *Analyst* **1983,** *108*, 1067-1071.

50. Sjoback, R.; Nygren, J.; Kubista, M., Absorption and Fluorescence Properties of Fluorescein. *Spectrochim. Acta A* **1995,** *51* (6), L7-L21.

51. Lavis, L. D.; Rutkoski, T. J.; Raines, R. T., Tuning the pK(a) of fluorescein to optimize binding assays. *Anal. Chem.* **2007,** *79* (17), 6775-6782.

52. Magde, D.; Wong, R.; Seybold, P. G., Fluorescence quantum yields and their relation to lifetimes of rhodamine 6G and fluorescein in nine solvents: improved absolute standards for quantum yields. *Photochem. Photobiol.* **2002,** *75* (4), 327-334.

53. Zehentbauer, F. M.; Moretto, C.; Stephen, R.; Thevar, T.; Gilchrist, J. R.; Pokrajac, D.; Richard, K. L.; Kiefer, J., Fluorescence spectroscopy of Rhodamine 6G: concentration and solvent effects. *Spectrochimica acta. Part A, Molecular and biomolecular spectroscopy* **2014,** *121*, 147-151.

54. Dickinson, B. C.; Tang, Y.; Chang, Z.; Chang, C. J., A nuclear-localized fluorescent hydrogen peroxide probe for monitoring sirtuin-mediated oxidative stress responses in vivo. *Chem. Biol.* **2011,** *18* (8), 943-948.

55. Peng, T.; Yang, D., Construction of a Library of Rhodol Fluorophores for Developing New Fluorescent Probes. *Org. Lett.* **2010,** *12* (3), 496-499.

56. Horobin, R.; Stockert, J.; Rashid-Doubell, F., Uptake and localisation of small-molecule fluorescent probes in living cells: a critical appraisal of QSAR models and a

case study concerning probes for DNA and RNA. *Histochem. Cell Biol.* **2013,** *139* (5), 623-637.

57. van Meer, G.; Voelker, D. R.; Feigenson, G. W., Membrane lipids: where they are and how they behave. *Nat. Rev. Mol. Cell Biol.* **2008,** *9* (2), 112-124.

58. McKibbin, C.; Mares, A.; Piacenti, M.; Williams, H.; Roboti, P.; Puumalainen, M.; Callan, A. C.; Lesiak-Mieczkowska, K.; Linder, S.; Harant, H.; High, S.; Flitsch, S. L.; Whitehead, R. C.; Swanton, E., Inhibition of protein translocation at the endoplasmic reticulum promotes activation of the unfolded protein response. *Biochem. J.* **2012,** *442*, 639-648.

59. Auner, H. W.; Moody, A. M.; Ward, T. H.; Kraus, M.; Milan, E.; May, P.; Chaidos, A.; Driessen, C.; Cenci, S.; Dazzi, F.; Rahemtulla, A.; Apperley, J. F.; Karadimitris, A.; Dillon, N., Combined Inhibition of p97 and the Proteasome Causes Lethal Disruption of the Secretory Apparatus in Multiple Myeloma Cells. *PLoS ONE* **2013,** *8* (9), e74415.

60. Steffen, J.; Seeger, M.; Koch, A.; Krüger, E., Proteasomal Degradation Is Transcriptionally Controlled by TCF11 via an ERAD-Dependent Feedback Loop. *Mol. Cell* **2010,** *40* (1), 147-158.

61. Dantuma, N. P.; Lindsten, K.; Glas, R.; Jellne, M.; Masucci, M. G., Short-lived green fluorescent proteins for quantifying ubiquitin/proteasome-dependent proteolysis in living cells. *Nat Biotech* **2000,** *18* (5), 538-543.

62. Menéndez-Benito, V.; Verhoef, L. G. G. C.; Masucci, M. G.; Dantuma, N. P., Endoplasmic reticulum stress compromises the ubiquitin–proteasome system. *Hum. Mol. Genet.* **2005,** *14* (19), 2787-2799.

63. Johnson, E. S.; Ma, P. C. M.; Ota, I. M.; Varshavsky, A., A Proteolytic Pathway That Recognizes Ubiquitin as a Degradation Signal. *J. Biol. Chem.* **1995,** *270* (29), 17442-17456.

64. Chou, T.-F.; Deshaies, R. J., Quantitative Cell-based Protein Degradation Assays to Identify and Classify Drugs That Target the Ubiquitin-Proteasome System. *J. Biol. Chem.* **2011,** *286* (19), 16546-16554.

65. Momose, I.; Tatsuda, D.; Ohba, S.-i.; Masuda, T.; Ikeda, D.; Nomoto, A., In vivo imaging of proteasome inhibition using a proteasome-sensitive fluorescent reporter. *Cancer Sci.* **2012,** *103* (9), 1730-1736.

66. Chou, T.-F.; Brown, S. J.; Minond, D.; Nordin, B. E.; Li, K.; Jones, A. C.; Chase, P.; Porubsky, P. R.; Stoltz, B. M.; Schoenen, F. J.; Patricelli, M. P.; Hodder, P.; Rosen, H.; Deshaies, R. J., Reversible inhibitor of p97, DBeQ, impairs both ubiquitin-dependent and autophagic protein clearance pathways. *Proc. Natl. Acad. Sci. U.S.A.* **2011,** *108* (12), 4834-4839.

67. Chou, T.-F.; Li, K.; Frankowski, K. J.; Schoenen, F. J.; Deshaies, R. J., Structure–Activity Relationship Study Reveals ML240 and ML241 as Potent and Selective Inhibitors of p97 ATPase. *ChemMedChem* **2013,** *8* (2), 297-312.

68. Menéndez-Benito, V.; Verhoef, L. G. G. C.; Masucci, M. G.; Dantuma, N. P., Endoplasmic reticulum stress compromises the ubiquitin–proteasome system. *Hum. Mol. Genet.* **2005,** *14* (19), 2787-2799.

69. Boelens, J.; Lust, S.; Offner, F.; Bracke, M. E.; Vanhoecke, B. W., Review. The endoplasmic reticulum: a target for new anticancer drugs. *In vivo* **2007,** *21* (2), 215-226.

70. Halliday, M.; Mallucci, G. R., Targeting the unfolded protein response in neurodegeneration: A new approach to therapy. *Neuropharmacology* **2014,** *76 Pt A*, 169-174.

71. Lin, J. H.; Walter, P.; Yen, T. S., Endoplasmic reticulum stress in disease pathogenesis. *Annu. Rev. Pathol.* **2008,** *3*, 399-425.

72. Le Grel, P.; Salaün, A.; Mocquet, C.; Le Grel, B.; Roisnel, T.; Potel, M., Z/E Isomerism in Nα-Nα-Disubstituted Hydrazides and the Amidoxy Bond: Application to the Conformational Analysis of Pseudopeptides Built of Hydrazinoacids and α-Aminoxyacids. *J. Org. Chem.* **2011,** *76* (21), 8756-8767.

73. Syakaev, V. V.; Podyachev, S. N.; Buzykin, B. I.; Latypov, S. K.; Habicher, W. D.; Konovalov, A. I., NMR study of conformation and isomerization of aryl- and heteroarylaldehyde 4-tert-butylphenoxyacetylhydrazones. *J. Mol. Struct.* **2006,** *788* (1–3), 55-62.

74. Velapoldi, R. A.; Tonnesen, H. H., Corrected Emission Spectra and Quantum Yields for a Series of Fluorescent Compounds in the Visible Spectral Region. *J. Fluorescence* **2004,** *14* (4), 465-472.

75. Kubin, R. F.; Fletcher, A. N., Fluorescence Quantum Yields of Some Rhodamine Dyes. *J. Luminescence* **1982,** *27* (4), 455-462.

76. Snare, M. J.; Treloar, F. E.; Ghiggino, K. P.; Thistlethwaite, P. J., The Photophysics of Rhodamine-B. *J. Photochem.* **1982,** *18* (4), 335-346.

77. Saikachi, H.; Ogawa, H., Synthesis of Furan Derivatives .15. 5-Nitrofuryl Polyene Aldehydes. *J. Am. Chem. Soc.* **1958,** *80* (14), 3642-3645.

Chapter 4

Phenotypic Screening of Fluorophores Against Zebrafish Embryos

4.1 Introduction

The zebrafish (*Danio rerio*) is an emerging model organism for studies of vertebrate biology.[1-2] As phenotypic small-molecule screens gain additional popularity, the zebrafish offers a model well suited for high-throughput screens of small-molecules.[3] Compared with mammals such as mice, zebrafish have inherent advantages to lend themselves to early *in vivo* screening. Adult zebrafish are fairly small (< 3 cm) and fertilized embryos are small enough (1 mm) for use in 96- and 384-well plates (Figure 4.1).[4] Zebrafish embryos can be easily produced on a large scale, and development occurs *ex vivo*, whereas mammals develop *in utero* and are typically cost-prohibitive to generate for large-scale screening. Zebrafish embryos naturally develop inside the chorion, a protective non-cellular membrane composed of glycoproteins.[5] Because the chorion can act as a barrier that limits compound exposure, embryos can be dechorionated mechanically or by proteinase treatments to allow for more uniform drug exposure.[6] Zebrafish embryos are transparent, allowing for development to be monitored using optical microscopy, and induced defects detected in a medium- to high-throughput manner. Additionally, the zebrafish genome has been completely sequenced, with 70% of genes having human orthologs.[7] These advantages make zebrafish embryos suitable for low cost *in vivo* investigation and large-scale phenotypic screening of small-molecules.

(A) Zygote immediately post-fertilization

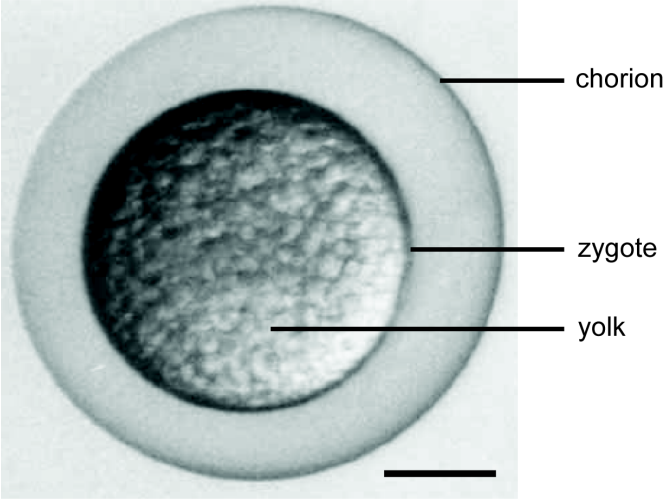

(B) Embyro 36 hours post fertilization

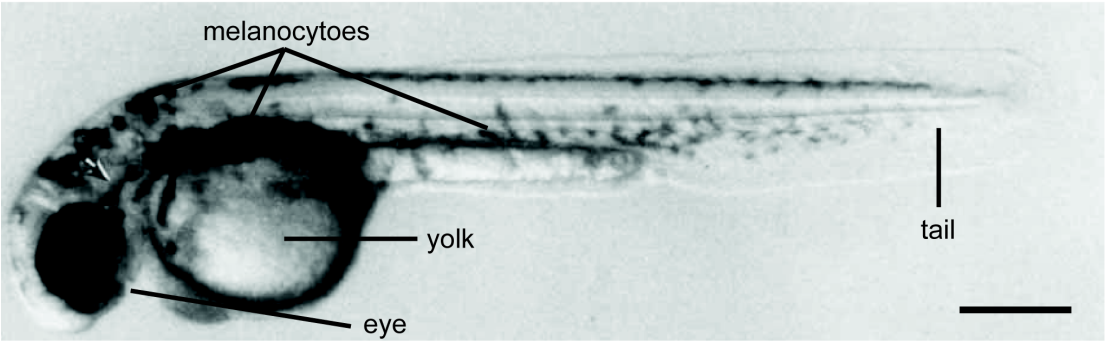

Figure 4.1. Panel A: A micrograph of a zebrafish zygote immediately following fertilization in a yolk-up orientation. The chorion surrounds the dividing cells of the zygote. Scale bar is 250 μm. Panel B: A micrograph of a zebrafish embryo without a chorion at 36 hours post fertilization (hpf). Tissues, organ systems, and anatomical features are becoming apparent and wild-type embryos begin developing strong pigmentation in the skin. Scale bar is 250 μm. Images were adapted with permission from Kimmel, C. B. *et al*. *Dev. Dyn.* **1995,** *203* (3), 253-310.

Although zebrafish embryos are well suited for fluorescence microscopy due to their relative transparency, the effects of small-molecule fluorophores on this organism has not been thoroughly investigated. More commonly, modern advances in genomic editing such CRISPR/Cas9 techniques are used to

generate fluorescent transgenic zebrafish.[8-10] Transgenic fish expressing fluorescent proteins using tissue[9] or organelle[11] specific promoters have been successfully used to study models of disease in real time *in vivo*. We are interested in the development of small-molecule fluorescent probes for studies of disease models in zebrafish embryos. This approach could be advantageous for several reasons. First, small-molecule probes can be easily administered in food or directly into the system water for absorption through multiple routes. Second, treatment with and removal of small-molecule probes can be executed with temporal control to mimic dosing of other vertebrates with drugs. Small-molecule probes further allow researchers to tailor spectral or chemical properties to investigate effects on ADME-Tox (Absorption, distribution, metabolism, excretion, toxicology) and other parameters of synthetic compounds.

Considering how little is understood about how small-molecule fluorophores interact with the zebrafish model, we sought to leverage the numerous small-molecule fluorescent probes developed in the Peterson laboratory to screen for novel phenotypes by confocal laser-scanning microscopy. To this end, living zebrafish embryos were treated with a number of probes created by members of the Peterson group and examined by looking for novel phenotypes. This chapter describes several “hits” from these studies and potential applications of this phenotypic discovery approach.

4.2 Hydrophobic Rhodamines for Visualization of Mitochondria *in vivo*

As discussed in Chapter 2, mitochondria normally exist as an extended tubular network and constantly undergo fission and fusion. This dynamic process is critical for maintenance of normal mitochondrial function by allowing renewal of mitochondrial DNA and proteins.[12,13] Irregularity in mitochondrial fission and fusion has been implicated in a number of diseases[14,15] such as neurodegeneration, aging, and cancer. The ability to observe the morphology of mitochondria in model organisms is a crucial step in monitoring the progression of certain models of disease.[16] Although a number of useful fluorescent probes are known to accumulate in polarized mitochondria in cell culture, to our knowledge the general translation of these probes to living zebrafish has not been previously explored.

Previous members of the Peterson laboratory developed the hydrophobic rhodamine analogues HR101 and HRB (Figure 4.2, panel A).[17] These probes, based on the fluorophores rhodamine 101 and rhodamine B, have been used to observe mitochondrial fission and fusion events in the nematode model organism *C. elegans*.[17] HR101 and HRB share the high lipophilicity and permanent positive charge that is common in other mitochondrial probes such as Rhodamine 123 and MitoTracker Deep Red (Figure 4.2, panel A). Imaging by confocal microscopy revealed that all of these probes readily accumulate in the mitochondria of HeLa cervical carcinoma cells in culture (Figure 4.2, panel B). To examine their accumulation in mitochondria of zebrafish, we directly compared HR101 and HRB with MitoTracker Deep Red and Rhodamine 123 in zebrafish

embryos at 72 hours post fertilization (hpf). Interestingly, when added at the same concentration (1 μM), HR101 was the only probe to strongly accumulate *in vivo* under these conditions (Figure 4.2, panel C). At this relatively low concentration, HR101 clearly stained all the cells in the optical plane, whereas HRB, MitoTracker Deep Red, and Rhodamine 123 showed little to no fluorescence under the same conditions (Figure 4.2, panel C). We reasoned that because HR101 is highly absorbed and relatively uniform in its distribution around peripheral tissues, it may have applications as a novel counter stain for studies of development. To explore this idea, as shown in Figure 4.2 Panel D, we imaged the eye of a living dechorionated 36 hpf embryonic zebrafish with a confocal microscopy Z-stack, and reconstructed the image in three dimensions. The development of the lens is useful model for several disease states and will be discussed more thoroughly later in this chapter. Observation of the epithelial layers around the eye as well as the developing lens (highlighted by the arrow) was found to be possible. To our knowledge, this ability to visualize the developing lens of a *living* zebrafish embryo with a small-molecule fluorophore has not been previously reported. In contrast to our observations of living embryos, in chemically fixed (dead) embryos, immunohistochemistry was previously used to observe developmental defects of the lens of these animals following knockdown of Hsp70.[18] In another study, transgenic embryos have been used to image the vasculature of the lens of the developing embryo both *in vivo*[19] and in dissected specimens.[20] In addition to visualizing tissues of the eye, treatment with HR101 allowed individual mitochondria to be visualized in other

cell types including epithelial cells of the tail (Figure 4.2, panel E). Observation over time enabled visualization of mitochondrial fission and fusion events that are crucial for maintenance of mitochondrial health. HR101 appears to be the first small-molecule fluorophore to be identified that allows facile imaging of mitochondria in living zebrafish embryos.

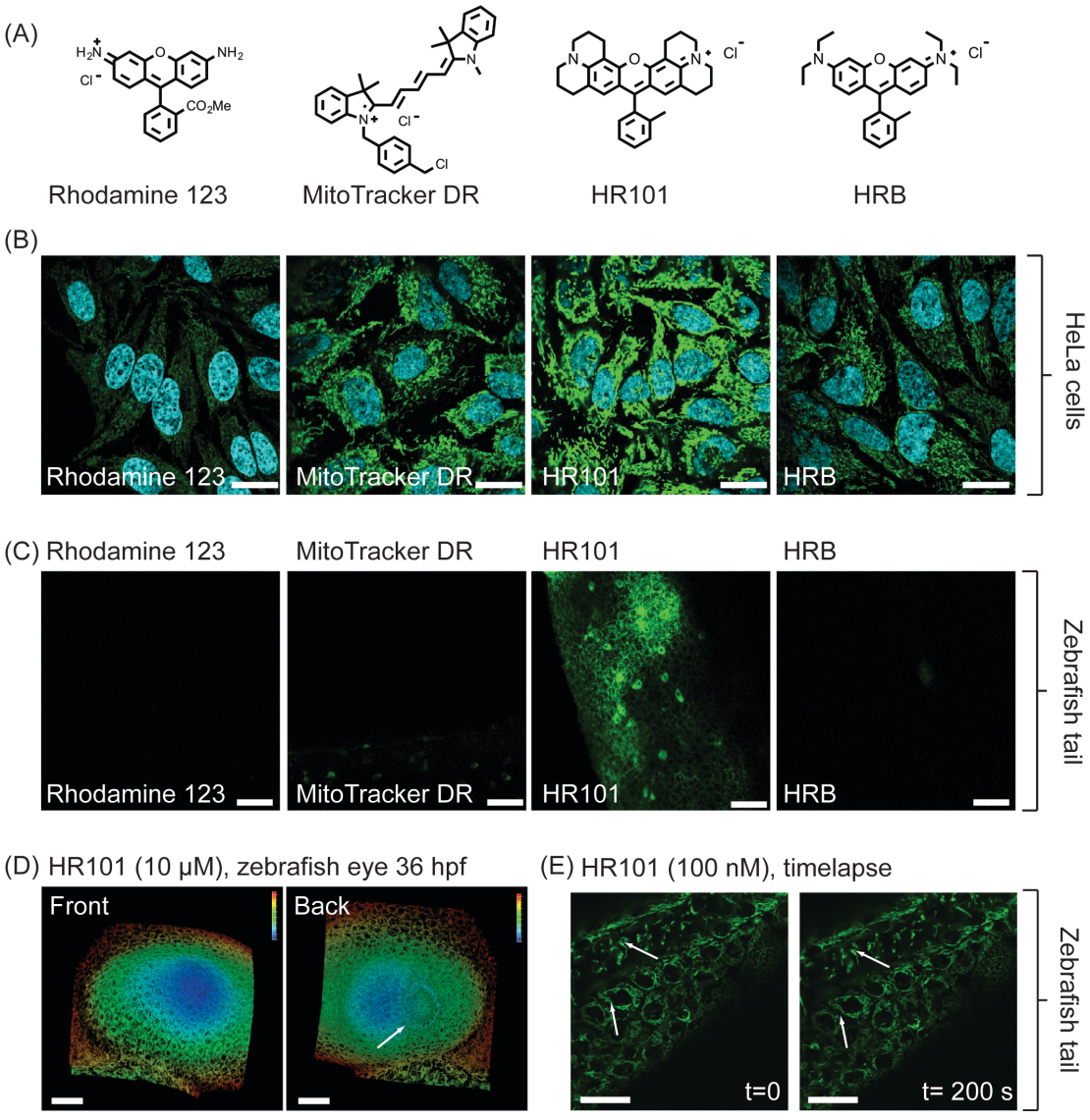

Figure 4.2. Panel A: Structures of the cationic mitochondrial fluorophores Rhodamine 123, MitoTracker Deep Red FM, HR101, and HRB. Panel B:

Confocal microscopy of HeLa cells treated with these compounds (100 nM, green fluorescence) and the nuclear stain Hoechst 33342 (1 μM, cyan fluorescence) for 30 min. The four cationic fluorophores can be observed to readily accumulate in mitochondria. Scale bar = 25 μm. Panel C: Treatment of 72 hpf zebrafish embryos with HR101, HRB, MitoTracker DeepRed, and Rhodamine 123 (1 μm, 1 h). Substantial fluorescence was only observed with HR101. Scale bar = 100 μm Panel D: Confocal Z-stack used to image HR101 in the developing eye of a living dechorinated 36 hpf zebrafish embryo. The arrow points to the developing lens. Scale bar = 50 μm. Z-stacks are colored by depth: blue to red (0–160 μm). Panel E: Confocal imaging of the tail of a living (36 hpf) zebrafish embryo treated with HR101 (100 nM, 8 h). Fusion and fission of mitochondria *in vivo* over time is observed (fission indicated by arrows). Scale bar = 25 μm.

4.3 An Acid-Activated Fluorophore Reveals V-ATPase Activity

The pH of fluids of living animals is a fundamental physicochemical condition that is critically important for cellular homeostasis.[21] Endosomes and lysosomes are two organelles that require low pH for proper function, and this acidity is maintained by pumping of protons into the vesicle lumen by the vacuolar ATPase (V-ATPase). When this process is blocked, failure to acidify endosomes can inhibit receptor trafficking in cell culture.[22] Improper V-ATPase activity has been linked to a number of diseases including X-linked myopathy with excessive autophagy (XMEA)[23] and osteoporosis.[24] Experimentally, the pH of the endosome-lysosome system can be perturbed using small molecule inhibitors. Bafilomycin A1 is a macrolide antibiotic that specific inhibits the proton pumping activity of V-ATPase.[25] Additionally, the anti-malaria drug chloroquine is used in *in vitro* assays to inhibit lysosomal degradation processes by raising lysosomal pH.[26]

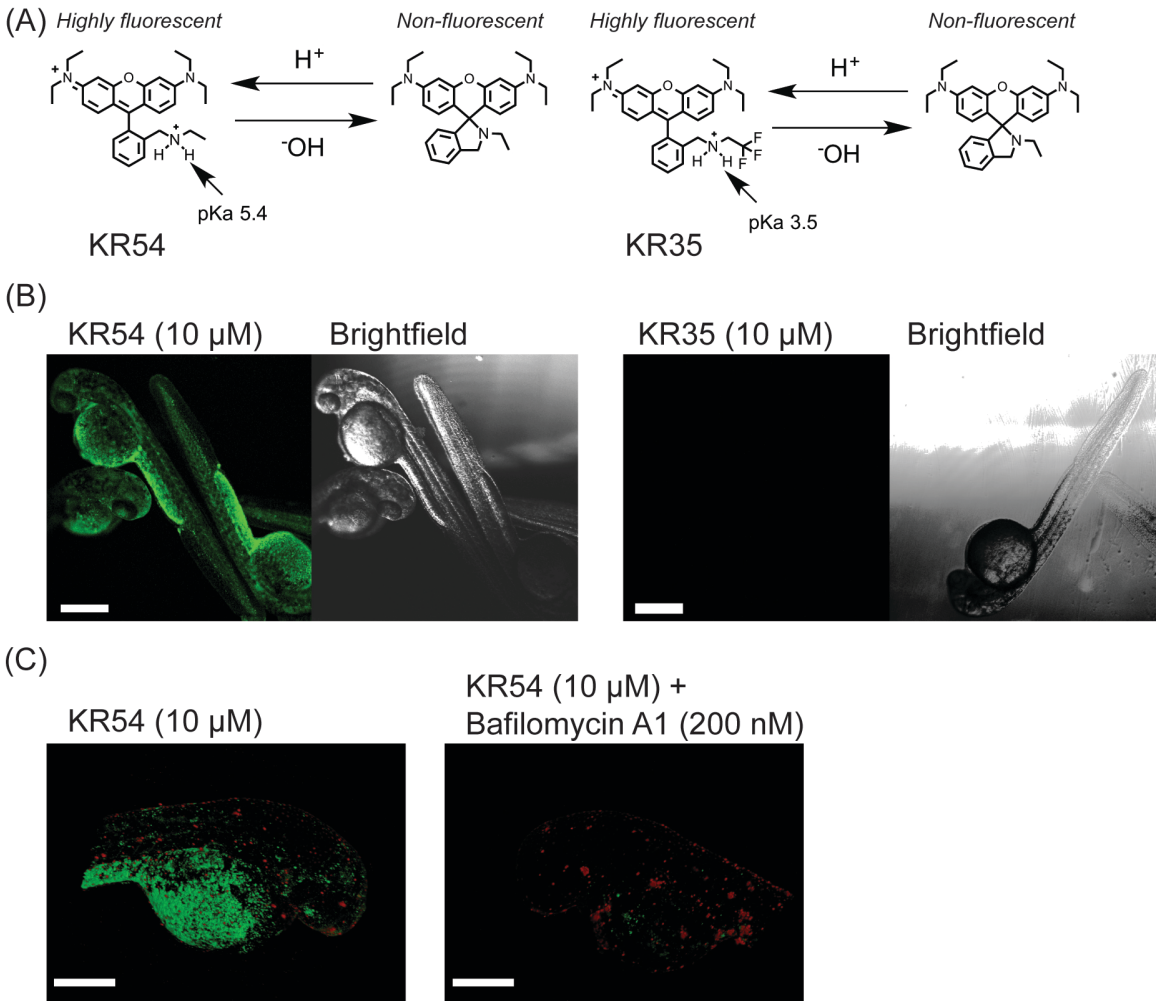

Figure 4.3 Panel A: Structures of the acid-activated fluorophores KR54 and KR35. The equilibrium between the acid-activated, highly fluorescent form, and the ring-closed, non-fluorescent form is shown. Panel B: Fluorescence microscopy of zebrafish embryos (36 hpf) treated with KR54 and KR35 (10 µM, 1 h). Only KR54 showed appreciable fluorescence staining. Scale bar = 2.5 mm. The brightfield images were contrast enhanced for clarity. Panel C: Confocal microscopy of a 36 hpf embryo treated with KR54 (10 µM, 30 min, green fluorescence) and the DNA stain SYBR green (10 µM, red fluorescence). KR54 can be observed primarily around the yolk. Pretreatment of these animals with the V-ATPase inhibitor Bafilomycin A1 (200 nM, 30 min) reduces the acid-activated fluorescence of KR54. Scale bar = 200 µm.

The Peterson laboratory previously published the synthesis of acid-activated fluorophores based on the structure of Rhodamine B (Figure 4.3, panel A).[27] These fluorophores are highly fluorescent under acidic conditions, but revert to a non-fluorescent cyclized form under basic conditions. The pH range of the acid sensitivity was shown to be tunable by addition of electronegative fluorine atoms to either the ethylamine side chain or the bottom ring (i.e. KR54 pKa = 5.4, KR35 pKa = 3.5). These acid-activated fluorophores were previously used to probe dynamic changes in the acidity of the alimentary canal of the nematode *C. elegans*, illustrating the utility of these probes in observing dynamic processes in *in vivo* animal models. Because pH is a fundamental physical chemical condition that plays a prominent role in physiology, we examined the fluorescence of KR54 and KR35 in treated zebrafish embryos.

When dechorionated 36 hpf embryos were treated with KR54 (10 μM in PBS pH 7.4, 1 h), strong fluorescence was observed around the yolk of the embryo (Figure 4.3, panel B). This fluorescence is indicative of an acidic environment around this nutrient-rich tissue. However, when these embryos were treated with the structurally similar compound KR35, no significant fluorescent was observed (Figure 4.3, panel B), suggesting that the acidity around the yolk is likely to be in the range of pH 5–6. The results with KR54 are consistent with other reports[28] that V-ATPase expressing cells surround the yolk of developing zebrafish. These acid-secreting cells are one type of ionocyte that are responsible for maintaining ion homeostasis in the embryonic zebrafish and are functionally homologous to the mammalian kidney.[29] The removal of metabolic

acid by the V-ATPase cells is coupled with sodium ion import by other Na+-pump rich cells.[28] Similar systems of ion balance through skin cells are known in other fish[30] and amphibian species.[31] Consistent with this model, embryos treated with V-ATPase inhibitor bafilomycin A1 showed decreased KR54 fluorescence (Figure 4.3, panel C). KR54 appears to allow visualization of the pH-lowering effect of acid-secretion in this process of ion homeostasis.

4.4 Conclusions

The zebrafish is an important vertebrate model organism that is particularly suited for large-scale, high-throughput studies. By screening this *in vivo* model against fluorophores that we previously reported, we found that the hydrophobic rhodamine HR101 is an effective probe of mitochondria of embryonic zebrafish. This probe appears to be the first small molecule that allows observation of the dynamics of individual mitochondria in this model organism *in vivo*. HR101 further provides a bright counterstain to observe developmental changes over time in specific tissues such as the eye in living embryos. Moreover, mitochondria of zebrafish are of substantial interest as models of human mitochondrial diseases.[32-33] Unique models of neurodegenerative disorders like Parkinson's disease[34-36] and the first animal model of the developmental disease MADD (Multiple Acyl-CoA Dehydrogenase Deficiency)[37] were developed in zebrafish.

Previous efforts to visualize the zebrafish mitochondrial network have primarily used transgenic animals expressing mitochondrial-specific GFP, YFP,

or DsRed fusion proteins.[16] Commercial MitoTracker dyes have been previously reported[28] for use in living zebrafish embryos. However, these MitoTracker dyes were of limited utility since only a subset of cells was labeled. The superiority of HR101 *in vivo* was shown here by direct comparison with other fluorescent mitochondrial probes (Figure 4.2, panel C). As the first mitochondrial dye to efficiently penetrate into diverse tissues of living zebrafish embryos, HR101 could fill a critical role as a rapid-acting, potent, and bright fluorescent mitochondrial probe.

By examining a series of acid-activated fluorophores, KR54 was shown to readily stain the exterior of the embryonic zebrafish yolk. This pattern of fluorescence suggested the presence of an acidic extracellular environment, and based on other reports[28] was proposed to be a downstream effect of cells expressing V-ATPase.[29] Consistent with this proposal, the fluorescence of KR54 was inhibited by treatment with the V-ATPase inhibitor bafilomycin A1. V-ATPase activity has been shown to play important roles in zebrafish models of tissue regeneration,[38] pigmentation,[39] and development.[40] As a novel probe in zebrafish biology, KR54 in zebrafish embryos could provide the basis for a unique and simple assay of V-ATPase activity *in vivo*.

4.5 Future Directions and Applications

The small molecules HR101 and KR54 represent examples of how fluorescent probes can be applied for novel studies of zebrafish embryos *in vivo*. In future studies, these and related compounds could be of significant interest for

high-throughput screening (HTS) and high content screening applications. Fluorophores such as KR54 and HR101 have potential for large-scale phenotypic screens looking directed at the discovery of inhibitors of V-ATPase activity, compounds that promote changes in mitochondria morphology, or agents that affect development.

Phenotypic screens of small-molecule libraries have previously identified novel inhibitors of V-ATPase activity in yeast, and these types of inhibitors are of interest for treatment of a variety of diseases such as cancer and osteoporosis.[41-43] In future studies, treatment of zebrafish embryos with KR54 could serve as the first *in vivo* whole-animal model for screening V-ATPase activity. Since KR54 can be dosed directly into system water containing embryos, the assay could be straightforward to administer. By monitoring the fluorescence of KR54 around the yolk by microscopy, changes in intensity (increases or decreases) and distribution could be possible. As shown in Figure 4.3C, the difference in KR54 fluorescent signal between the DMSO control and the V-ATPase inhibition of bafilomycin A1 is quite substantial and this large difference could lend itself to automated analysis of V-ATPase activity.

As the first small-molecule fluorophore known to accumulate in mitochondria of diverse peripheral issues, HR101 could provide a straightforward *in vivo* assay to identify compounds that perturb mitochondrial morphology. These types of compounds are of interest as probes and potential therapeutics.[44-45] Previous cell-based chemical genetic screens have found several compounds that are cytoprotective through their ability to inhibit

mitochondrial fission[46] or promote mitochondrial fusion,[47] with potential applications as treatments for neurodegeneration. Similar assays in a vertebrate model using HR101 could detect alterations of mitochondrial morphology and concurrent changes in embryonic development. In order to further explore the potential of HR101 in zebrafish embryos, comparative toxicity studies between embryos and cell culture are planned. Combining observations of HR101 in living embryos with known genetic and chemical modulators of mitochondrial function will be critical in establishing the utility of these types of screens. As more small-molecule fluorophores are investigated in this model organism, probes with unique photophysical and physicochemical properties have the potential to allow new discoveries in biology and medicine.

4.6 Experimental

4.6.1 Chemicals and molecular probes. Hydrophobic rhodamines (HR101 and HRB)[17] and acid-activated fluorophores (KR54 and KR35)[27] were prepared as previously described. Rhodamine 123, MitoTracker Deep Red FM, and SybrGreen were purchased from Invitrogen. Hoechst 33342 and Bafilomycin A1 were purchased from Sigma.

4.6.2 Animal Care. All work with zebrafish was approved by the KU IACUC. Wild-type adult zebrafish for breeding were obtained from Carolina Biological Supply Company or the Marine Biological Laboratory and housed in a Pentair Aquatic Habitats ZF0601 system. The system was set at 14 hours “lights-on,” 10

hours “lights-off.” Breeding experiments were done using a Pentair breeding tank and timed to daily “lights-on.” Zebrafish embryos were collected with a mesh strainer and thoroughly washed with E3 media. Dechorionation was done by dissecting microscopy with ultra-fine tweezers. Small-molecules were added in E3 medium or PBS (pH 7.4) as indicated. Compounds were diluted to final indicated concentrations from a 1000x DMSO stock. Embryo count and DMSO concentrations were normalized for all experiments to assure equal exposure.

4.6.3 Cell Line. HeLa (CCL-2) cells were obtained from ATCC and cultured in a humidified CO_2 (5%) incubator at 37 °C. Dulbecco’s Modified Eagle Medium (DMEM, Sigma D5796) was supplemented with FBS (10%, Sigma F0926), penicillin (100 units/L), and streptomycin (100 µg/L, Sigma P4333).

4.6.4 Microscopy. Embryos were imaged in 8-well cover glass slides (Idibi µ-Slide) with a Leica SPE2 confocal laser scanning microscope fitted with either a 10x, 20x, 40x (oil emersion), 40x LWD (long working distance), or 63x objective. HR101, HRB, KR54, KR35 were excited using a 532 nm laser and photons were collected from 550 nm – 650 nm. MitoTracker DeepRed FM (MTDR) was excited using a 635 nm laser and photons were collected from 650 nm – 750 nm. SYBR Green was excited with a 488 nm laser and photons were collected from 500 nm – 520 nm. Hoechst 3342 was excited with a 405 nm laser and photons were collected from 420 nm – 480 nm.

4.7 References

1. Dooley, K.; Zon, L. I., Zebrafish: a model system for the study of human disease. *Curr. Opin. Genet. Dev.* **2000,** *10* (3), 252-256.

2. Briggs, J. P., The zebrafish: a new model organism for integrative physiology. *Am. J. Physiol-Reg. I.* **2002,** *282* (1), R3-R9.

3. MacRae, C. A.; Peterson, R. T., Zebrafish-Based Small Molecule Discovery. *Chem. Biol.* **2003,** *10* (10), 901-908.

4. Kimmel, C. B.; Ballard, W. W.; Kimmel, S. R.; Ullmann, B.; Schilling, T. F., Stages of Embryonic-Development of the Zebrafish. *Dev. Dyn.* **1995,** *203* (3), 253-310.

5. Bonsignorio, D.; Perego, L.; DelGiacco, L.; Cotelli, F., Structure and macromolecular composition of the zebrafish egg chorion. *Zygote* **1996,** *4* (2), 101-108.

6. Mandrell, D.; Truong, L.; Jephson, C.; Sarker, M. R.; Moore, A.; Lang, C.; Simonich, M. T.; Tanguay, R. L., Automated Zebrafish Chorion Removal and Single Embryo Placement: Optimizing Throughput of Zebrafish Developmental Toxicity Screens. *J. Lab. Autom.* **2012,** *17* (1), 66-74.

7. Howe, K.; Clark, M. D.; Torroja, C. F.; Torrance, J.; Berthelot, C.; Muffato, M.; Collins, J. E.; Humphray, S.; McLaren, K.; Matthews, L.; McLaren, S.; Sealy, I.; Caccamo, M.; Churcher, C.; Scott, C.; Barrett, J. C.; Koch, R.; Rauch, G.-J.; White, S.; Chow, W.; Kilian, B.; Quintais, L. T.; Guerra-Assuncao, J. A.; Zhou, Y.; Gu, Y.; Yen, J.; Vogel, J.-H.; Eyre, T.; Redmond, S.; Banerjee, R.; Chi, J.; Fu, B.; Langley, E.; Maguire, S. F.; Laird, G. K.; Lloyd, D.; Kenyon, E.; Donaldson, S.;

Sehra, H.; Almeida-King, J.; Loveland, J.; Trevanion, S.; Jones, M.; Quail, M.; Willey, D.; Hunt, A.; Burton, J.; Sims, S.; McLay, K.; Plumb, B.; Davis, J.; Clee, C.; Oliver, K.; Clark, R.; Riddle, C.; Eliott, D.; Threadgold, G.; Harden, G.; Ware, D.; Mortimer, B.; Kerry, G.; Heath, P.; Phillimore, B.; Tracey, A.; Corby, N.; Dunn, M.; Johnson, C.; Wood, J.; Clark, S.; Pelan, S.; Griffiths, G.; Smith, M.; Glithero, R.; Howden, P.; Barker, N.; Stevens, C.; Harley, J.; Holt, K.; Panagiotidis, G.; Lovell, J.; Beasley, H.; Henderson, C.; Gordon, D.; Auger, K.; Wright, D.; Collins, J.; Raisen, C.; Dyer, L.; Leung, K.; Robertson, L.; Ambridge, K.; Leongamornlert, D.; McGuire, S.; Gilderthorp, R.; Griffiths, C.; Manthravadi, D.; Nichol, S.; Barker, G.; Whitehead, S.; Kay, M.; Brown, J.; Murnane, C.; Gray, E.; Humphries, M.; Sycamore, N.; Barker, D.; Saunders, D.; Wallis, J.; Babbage, A.; Hammond, S.; Mashreghi-Mohammadi, M.; Barr, L.; Martin, S.; Wray, P.; Ellington, A.; Matthews, N.; Ellwood, M.; Woodmansey, R.; Clark, G.; Cooper, J.; Tromans, A.; Grafham, D.; Skuce, C.; Pandian, R.; Andrews, R.; Harrison, E.; Kimberley, A.; Garnett, J.; Fosker, N.; Hall, R.; Garner, P.; Kelly, D.; Bird, C.; Palmer, S.; Gehring, I.; Berger, A.; Dooley, C. M.; Ersan-Urun, Z.; Eser, C.; Geiger, H.; Geisler, M.; Karotki, L.; Kirn, A.; Konantz, J.; Konantz, M.; Oberlander, M.; Rudolph-Geiger, S.; Teucke, M.; Osoegawa, K.; Zhu, B.; Rapp, A.; Widaa, S.; Langford, C.; Yang, F.; Carter, N. P.; Harrow, J.; Ning, Z.; Herrero, J.; Searle, S. M. J.; Enright, A.; Geisler, R.; Plasterk, R. H. A.; Lee, C.; Westerfield, M.; de Jong, P. J.; Zon, L. I.; Postlethwait, J. H.; Nusslein-Volhard, C.; Hubbard, T. J. P.; Crollius, H. R.; Rogers, J.; Stemple, D. L., The zebrafish reference genome

sequence and its relationship to the human genome. *Nature* **2013,** *496* (7446), 498-503.

8. Irion, U.; Krauss, J.; Nüsslein-Volhard, C., Precise and efficient genome editing in zebrafish using the CRISPR/Cas9 system. *Development* **2014,** *141* (24), 4827-4830.

9. Ablain, J.; Durand, Ellen M.; Yang, S.; Zhou, Y.; Zon, Leonard I., A CRISPR/Cas9 Vector System for Tissue-Specific Gene Disruption in Zebrafish. *Dev. Cell* **2015,** *32* (6), 756-764.

10. Shah, A. N.; Davey, C. F.; Whitebirch, A. C.; Miller, A. C.; Moens, C. B., Rapid reverse genetic screening using CRISPR in zebrafish. *Nat. Methods* **2015,** *12* (6), 535-540.

11. Kim, M. J.; Kang, K. H.; Kim, C. H.; Choi, S. Y., Real-time imaging of mitochondria in transgenic zebrafish expressing mitochondrially targeted GFP. *Biotechniques* **2008,** *45* (3), 331-334.

12. Westermann, B., Mitochondrial fusion and fission in cell life and death. *Nat. Rev. Mol. Cell Biol.* **2010,** *11* (12), 872-884.

13. Karbowski, M.; Youle, R. J., Dynamics of mitochondrial morphology in healthy cells and during apoptosis. *Cell Death Differ.* **2003,** *10* (8), 870-880.

14. Chan, D. C., Mitochondria: Dynamic Organelles in Disease, Aging, and Development. *Cell* **2006,** *125* (7), 1241-1252.

15. Corrado, M.; Scorrano, L.; Campello, S., Mitochondrial Dynamics in Cancer and Neurodegenerative and Neuroinflammatory Diseases. *Int. J. of Cell Bio.* **2012,** *2012*, 13.

16. Plucińska, G.; Paquet, D.; Hruscha, A.; Godinho, L.; Haass, C.; Schmid, B.; Misgeld, T., In Vivo Imaging of Disease-Related Mitochondrial Dynamics in a Vertebrate Model System. *J. Neurosci.* **2012,** *32* (46), 16203-16212.

17. Mottram, L. F.; Forbes, S.; Ackley, B. D.; Peterson, B. R., Hydrophobic analogues of rhodamine B and rhodamine 101: potent fluorescent probes of mitochondria in living C. elegans. *Beilstein J. Org. Chem.* **2012,** *8*, 2156-2165.

18. Evans, T. G.; Yamamoto, Y.; Jeffery, W. R.; Krone, P. H., Zebrafish Hsp70 Is Required for Embryonic Lens Formation. *Cell Stress Chaperones* **2005,** *10* (1), 66-78.

19. Hartsock, A.; Lee, C.; Arnold, V.; Gross, J. M., In vivo analysis of hyaloid vasculature morphogenesis in zebrafish: A role for the lens in maturation and maintenance of the hyaloid. *Dev. Biol.* **2014,** *394* (2), 327-339.

20. Alvarez, Y.; Cederlund, M. L.; Cottell, D. C.; Bill, B. R.; Ekker, S. C.; Torres-Vazquez, J.; Weinstein, B. M.; Hyde, D. R.; Vihtelic, T. S.; Kennedy, B. N., Genetic determinants of hyaloid and retinal vasculature in zebrafish. *BMC Dev. Biol.* **2007,** *7*, 114.

21. Demaurex, N., pH Homeostasis of Cellular Organelles. *News Physiol. Sci.* **2002,** *17* (1), 1-5.

22. Johnson, L. S.; Dunn, K. W.; Pytowski, B.; McGraw, T. E., Endosome acidification and receptor trafficking: bafilomycin A1 slows receptor externalization by a mechanism involving the receptor's internalization motif. *Mol. Biol. Cell* **1993,** *4* (12), 1251-1266.

23. Ramachandran, N.; Munteanu, I.; Wang, P.; Ruggieri, A.; Rilstone, J.; Israelian, N.; Naranian, T.; Paroutis, P.; Guo, R.; Ren, Z.-P.; Nishino, I.; Chabrol, B.; Pellissier, J.-F.; Minetti, C.; Udd, B.; Fardeau, M.; Tailor, C.; Mahuran, D.; Kissel, J.; Kalimo, H.; Levy, N.; Manolson, M.; Ackerley, C.; Minassian, B., VMA21 deficiency prevents vacuolar ATPase assembly and causes autophagic vacuolar myopathy. *Acta Neuropathol. (Berl).* **2013,** *125* (3), 439-457.

24. Kartner, N.; Yao, Y.; Li, K.; Crasto, G. J.; Datti, A.; Manolson, M. F., Inhibition of Osteoclast Bone Resorption by Disrupting Vacuolar H+-ATPase a3-B2 Subunit Interaction. *J. Biol. Chem.* **2010,** *285* (48), 37476-37490.

25. Bowman, E. J.; Siebers, A.; Altendorf, K., Bafilomycins: a class of inhibitors of membrane ATPases from microorganisms, animal cells, and plant cells. *Proc. Natl. Acad. Sci. U. S. A.* **1988,** *85* (21), 7972-7976.

26. Wibo, M.; Poole, B., PROTEIN DEGRADATION IN CULTURED CELLS: II. The Uptake of Chloroquine by Rat Fibroblasts and the Inhibition of Cellular Protein Degradation and Cathepsin B1. *J. Cell Biol.* **1974,** *63* (2), 430-440.

27. Bender, A.; Woydziak, Z. R.; Fu, L.; Branden, M.; Zhou, Z.; Ackley, B. D.; Peterson, B. R., Novel Acid-Activated Fluorophores Reveal a Dynamic Wave of Protons in the Intestine of Caenorhabditis elegans. *ACS Chem. Biol.* **2012,** *8* (3), 636-642.

28. Lin, L.-Y.; Horng, J.-L.; Kunkel, J. G.; Hwang, P.-P., Proton pump-rich cell secretes acid in skin of zebrafish larvae. *Am. J. Physiol. Cell Physiol.* **2006,** *290* (2), C371-C378.

29. Hwang, P. P.; Chou, M. Y., Zebrafish as an animal model to study ion homeostasis. *Pflug. Arch. Eur. J. Phy.* **2013,** *465* (9), 1233-1247.

30. Lin, C. C.; Lin, L. Y.; Hsu, H. H.; Thermes, V.; Prunet, P.; Horng, J. L.; Hwang, P. P., Acid secretion by mitochondrion-rich cells of medaka (Oryzias latipes) acclimated to acidic freshwater. *Am. J. Physiol-Reg. I.* **2012,** *302* (2), R283-R291.

31. Ehrenfeld, J.; Klein, U., The key role of the H+ V-ATPase in acid-base balance and Na+ transport processes in frog skin. *J. Exp. Biol.* **1997,** *200* (2), 247-56.

32. Steele, S. L.; Prykhozhij, S. V.; Berman, J. N., Zebrafish as a model system for mitochondrial biology and diseases. *Translational Research* **2014,** *163* (2), 79-98.

33. Pinho, B. R.; Santos, M. M.; Fonseca-Silva, A.; Valentão, P.; Andrade, P. B.; Oliveira, J. M. A., How mitochondrial dysfunction affects zebrafish development and cardiovascular function: an in vivo model for testing mitochondria-targeted drugs. *Br. J. Pharmacol.* **2013,** *169* (5), 1072-1090.

34. Bretaud, S.; Allen, C.; Ingham, P. W.; Bandmann, O., p53-dependent neuronal cell death in a DJ-1-deficient zebrafish model of Parkinson's disease. *J. Neurochem.* **2007,** *100* (6), 1626-1635.

35. Morais, V. A.; Verstreken, P.; Roethig, A.; Smet, J.; Snellinx, A.; Vanbrabant, M.; Haddad, D.; Frezza, C.; Mandemakers, W.; Vogt‐Weisenhorn, D.; Van Coster, R.; Wurst, W.; Scorrano, L.; De Strooper, B., Parkinson's disease

mutations in PINK1 result in decreased Complex I activity and deficient synaptic function. *EMBO Mol. Med.* **2009,** *1* (2), 99-111.

36. Blandini, F.; Armentero, M. T., Animal models of Parkinson's disease. *FEBS J.* **2012,** *279* (7), 1156-66.

37. Kim, S.-H.; Scott, S. A.; Bennett, M. J.; Carson, R. P.; Fessel, J.; Brown, H. A.; Ess, K. C., Multi-organ Abnormalities and mTORC1 Activation in Zebrafish Model of Multiple Acyl-CoA Dehydrogenase Deficiency. *PLoS Genet.* **2013,** *9* (6), e1003563.

38. Monteiro, J.; Aires, R.; Becker, J. D.; Jacinto, A.; Certal, A. C.; Rodríguez-León, J., V-ATPase Proton Pumping Activity Is Required for Adult Zebrafish Appendage Regeneration. *PLoS ONE* **2014,** *9* (3), e92594.

39. Dooley, C. M.; Schwarz, H.; Mueller, K. P.; Mongera, A.; Konantz, M.; Neuhauss, S. C. F.; Nüsslein-Volhard, C.; Geisler, R., Slc45a2 and V-ATPase are regulators of melanosomal pH homeostasis in zebrafish, providing a mechanism for human pigment evolution and disease. *Pigment Cell Melanoma Res.* **2013,** *26* (2), 205-217.

40. Horng, J.-L.; Lin, L.-Y.; Huang, C.-J.; Katoh, F.; Kaneko, T.; Hwang, P.-P., Knockdown of V-ATPase subunit A (atp6v1a) impairs acid secretion and ion balance in zebrafish (Danio rerio). *Am. J. Physiol-Reg. I.* **2007,** *292* (5), R2068-R2076.

41. Stephan, J.; Franke, J.; Ehrenhofer-Murray, A. E., Chemical genetic screen in fission yeast reveals roles for vacuolar acidification, mitochondrial fission, and cellular GMP levels in lifespan extension. *Aging Cell* **2013,** *12* (4), 574-583.

42. Johnson, R. M.; Allen, C.; Melman, S. D.; Waller, A.; Young, S. M.; Sklar, L. A.; Parra, K. J., Identification of inhibitors of vacuolar proton-translocating ATPase pumps in yeast by high-throughput screening flow cytometry. *Anal. Biochem.* **2010,** *398* (2), 203-211.

43. Chan, C.-Y.; Prudom, C.; Raines, S. M.; Charkhzarrin, S.; Melman, S. D.; De Haro, L. P.; Allen, C.; Lee, S. A.; Sklar, L. A.; Parra, K. J., Inhibitors of V-ATPase Proton Transport Reveal Uncoupling Functions of Tether Linking Cytosolic and Membrane Domains of V0 Subunit a (Vph1p). *J. Biol. Chem.* **2012,** *287* (13), 10236-10250.

44. Iannetti, E. F.; Willems, P. H. G. M.; Pellegrini, M.; Beyrath, J.; Smeitink, J. A. M.; Blanchet, L.; Koopman, W. J. H., Toward high-content screening of mitochondrial morphology and membrane potential in living cells. *Int. J. Biochem. Cell Biol.* **2015,** *63*, 66-70.

45. Andreux, P. A.; Houtkooper, R. H.; Auwerx, J., Pharmacological approaches to restore mitochondrial function. *Nat. Rev. Drug Discov.* **2013,** *12* (6), 465-483.

46. Cassidy-Stone, A.; Chipuk, J. E.; Ingerman, E.; Song, C.; Yoo, C.; Kuwana, T.; Kurth, M. J.; Shaw, J. T.; Hinshaw, J. E.; Green, D. R.; Nunnari, J., Chemical Inhibition of the Mitochondrial Division Dynamin Reveals Its Role in Bax/Bak-Dependent Mitochondrial Outer Membrane Permeabilization. *Dev. Cell* **2008,** *14* (2), 193-204.

47. Wang, D.; Wang, J.; Bonamy, G. M. C.; Meeusen, S.; Brusch, R. G.; Turk, C.; Yang, P.; Schultz, P. G., A Small Molecule Promotes Mitochondrial Fusion in Mammalian Cells. *Angew. Chem. Int. Ed.* **2012,** *51* (37), 9302-9305.

Chapter 5

Ethylene glycol-linked Dimers of Cholesterol as Stabilizers of Liposomes

5.1 Introduction

Lipid vesicles (liposomes) have been widely investigated in drug-delivery systems.[1-2] As of early 2015, a number of drugs have been approved as liposomal formulations including doxorubicin,[3-4] vincristine,[5] and morphine.[6] In total, 11 different marketed agents use liposomes, and a number of similar agents are currently in clinical trials.[2] Liposomes can benefit delivery by changing the pharmacokinetic parameters of an agent, including solubility, half-life, or selective distribution into tissues.[7]

Liposomes for drug delivery include phospholipids such as distearoylphosphotidylcholine (DSPC). The choice of these phospholipids can greatly impact the function of a liposome by altering properties of membrane fluidity, charge, and stability.[2] Cholesterol (**11**) is also commonly used in liposome formation as it favorably alters the biophysical properties of the liposome. This sterol (**11**) is a critical component of mammalian cell membrane and accounts for approximately 30 mol% of the lipids of mammalian plasma membranes.[8] When included in liposomes at approximately 30 mol %, cholesterol eliminates the thermotropic phase transition of the phospholipid component[9] and limits membrane permeability.[10] However, cholesterol incorporated into the liposome bilayer can transfer to other biological bilayers or

macromolecules, which can induce premature leakage of encapsulated substances.[7, 11]

Synthetic cholesterol-modified phospholipids have previously been reported to limit extraction of cholesterol from liposomes *in vivo*.[12-13] To this end, Szoka and co-workers prepared cholesterol-modified phospholipid dimers that exhibit higher membrane stability than free cholesterol in biological systems.[13] The most promising compound, DChemsPC (**12**), contains two cholesteryl units at both the *sn*-1 and *sn*-2 positions of phosphatidylcholine connected through succinyl diester linkages. Liposomes that incorporate **12** exhibit favorable properties compared with unmodified cholesterol including eliminating cholesterol exchange, reducing membrane leakage, and efficient delivery of doxorubicin *in vivo* comparable to Doxil.[13]

While the protective affects of **12** were promising, several factors could potentially limit the large scale utility of this agent. Although **12** is commercially available (Avanti), it is expensive at $1,650 per gram. Additionally, the published synthesis of **12** uses a glycerolic phosphocholine starting material of unspecified stereochemistry, leaving the possibility of a diastereomeric mixture of final products.[13] The cholesterol esters and phosphoglycerol esters in this compound also potentially leave liposomes susceptible to endogenous lipases.[14] With these issues in mind, we set out to design and test structurally simplified cholesterol dimers that could retain and potentially improve upon the liposomal stabilization of **12**, but are synthetically more practical for larger scale formulation.

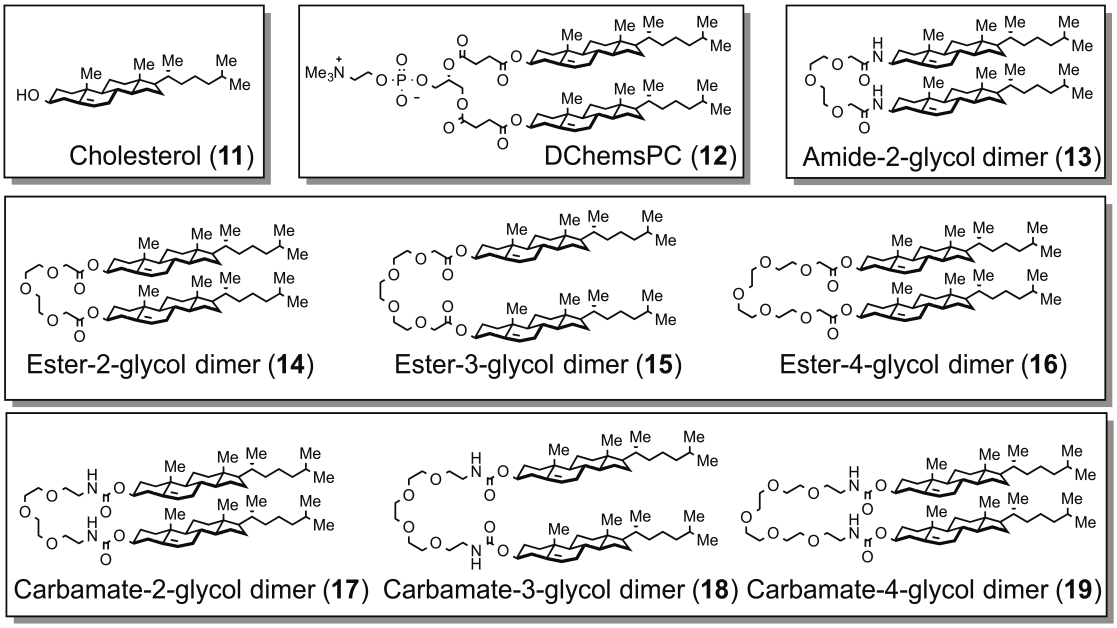

Figure 5.1. Structures of cholesterol (**11**), the previously reported cholesterol-modified phospholipid DChemsPC (**12**), and the novel cholesterol dimers **13**–**19** bearing systematic modifications in linker type and length.

5.2 Synthesis of Novel Ethylene Glycol-Linked Cholesterol Dimers

We hypothesized that the phosphocholine triglyceride could be functionally replaced with polar ethylene glycol linkers of various lengths. This simple modification might generate dimers that are potentially more synthetically accessible with favorable membrane protective effects similar to dimer **12**. To test this hypothesis, novel cholesterol dimers **13**-**19** were designed that systematically varied the number of ethylene glycol units as well as the functional group for attachment of the steroid to the linker (Figure 5.1). The synthesis of these novel dimers is outlined in Figure 5.2. The starting material **20a** is commercially available, and **20b-c** and **21a-c** were prepared from inexpensive commercial alcohols. Amide **13** was prepared from the intermediate acyl chloride

and 3β-cholesterylamine.[15] Esters **14**-**16** were prepared using DCC coupling of free cholesterol at slightly elevated temperatures. Carbamates **17**-**19** were prepared from condensation of aminoethylene glycols with cholesterol chloroformate. Although these dimers were made in low to moderate yields (28 - 65%), the products could be readily purified by normal phase silica chromatography, and the starting materials were generally inexpensive, making them highly accessible for further studies.

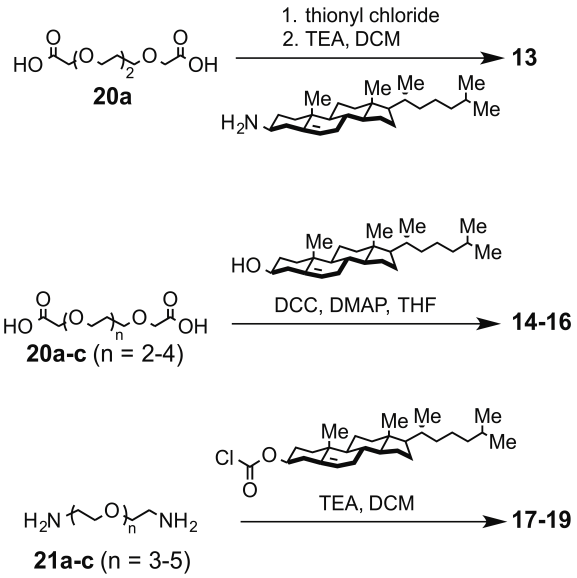

Figure 5.2. Synthesis of the novel cholesterol dimers **13**-**19**.

5.3 Studies of Liposomal Stability

To evaluate the stability of liposomes prepared with the new cholesterol dimers, we collaborated with the laboratory of Prof. Rodney Ho (U. Washington). The Ho laboratory prepared liposomes using **11**-**19** as potential stabilizing agents. It was found that all cholesterol compounds except **13** formed stable

liposomes of similar size (Figure 5.3, panel A). Amide **13** was unable to stabilize liposomes, possibly due to limited incorporation in the bilayer resulting from the higher rigidity of the amide linkage in the dimer.

To examine the effects of the new cholesterol dimers on liposomes, our collaborators examined the effect of binding of total serum proteins to liposomes. As negative and positive controls, liposomes were prepared with either **11** (free cholesterol) or the previously reported dimer **12** (Figure 5.3, panel B). To test liposome stability under approximate *in vivo* conditions, liposome samples were incubated in 100% monkey serum (macaque) for either 1 or 24 hours and stability was measured by monitoring leakage of the encapsulated fluorophore calcein. After 1 h, all dimers except for **17** showed improved liposome stability compared to free cholesterol similar to that seen with **12**. After 24 h, all samples showed increase leakage, but the dimers **14**–**16**, **18**, & **19** showed stability equal to or greater than **12**.

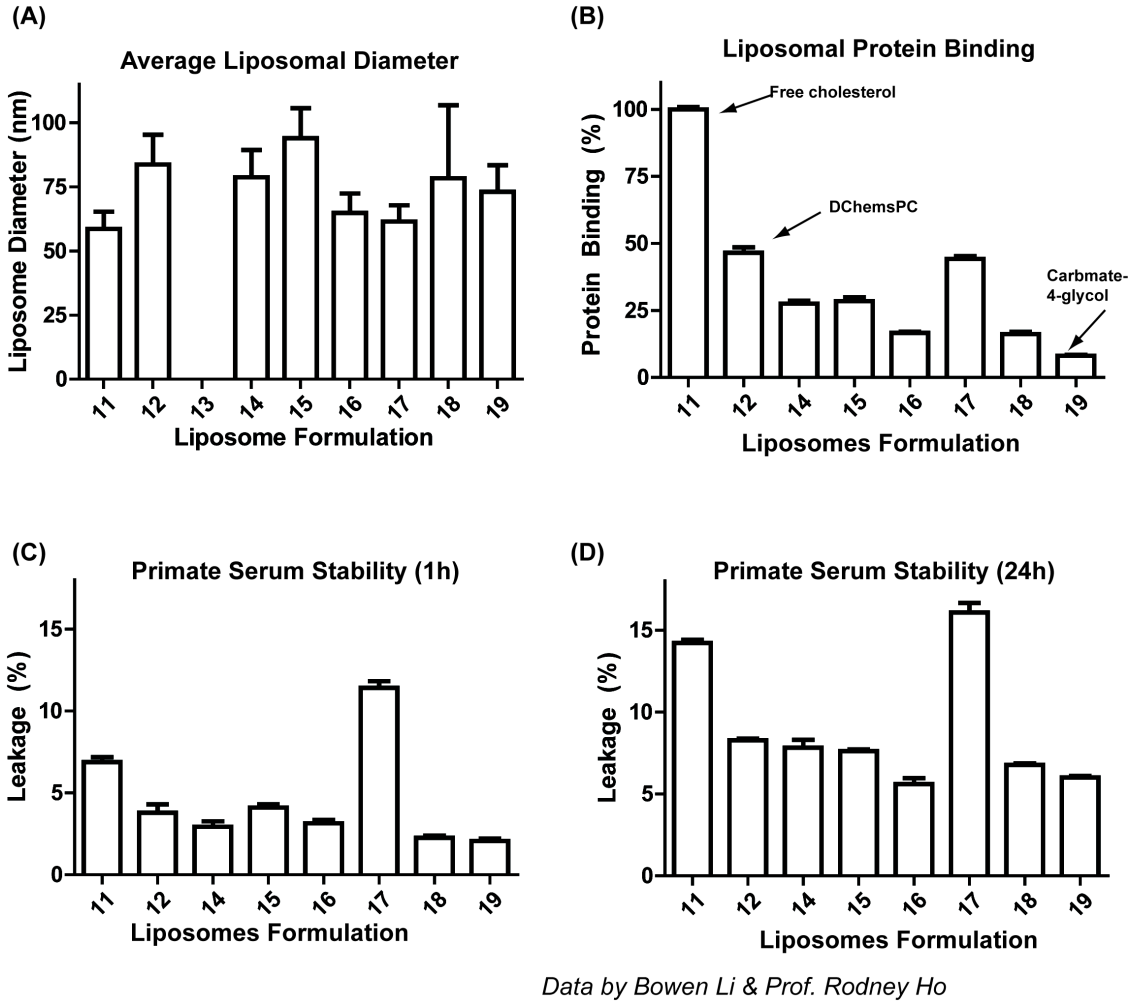

Figure 5.3. Panel A: Average sizes of liposomes containing 45 mol% cholesterol or 22.5 mol% of the indicated dimer (equivalent for total cholesterol) and 55% DSPC. Compound **13** failed to form stable liposomes in DSPC. Panel B: Protein binding to liposomes formulated with each cholesterol agent. Values are normalized to protein binding of liposomes containing free cholesterol. Panel C: Stability of liposomes formulated with each cholesterol agent in 100% primate serum for 1 h. Stability was measured by release of encapsulated calcein. Panel D: Stability of liposomes formulated with each cholesterol agent in 100% primate serum for 24h. Stability was measured by release of encapsulated calein. Data provided by Rodney Ho and Bowen Li (U. Washington).

5.4 Analysis of Liposome Composition by Mass Spectrometry

To quantify the components of the liposomes prepared by our collaborators, mass spectrometry was used to assay the phospholipid component DSPC as well as its hydrolysis product LysoPC (18:0 lysoPC; 1-stearoyl-2-hydroxy-*sn*-glycero-3-phosphocholine, Figure 5.4, panel A). Using commercial lipids, a standard curve was developed to allow for direct quantification of each phosphocholine compound from the total integrated ion count (Figure 5.4, panel B). At low concentrations, the ion count is linear, which allows simple conversion from ion count back to physical quantity in test samples. Since endogenous lipases have the potential to degrade the prepared liposomes *in vivo*, a mass spectrometry-based lipase assay was developed. Using commercial DSPC, increasing amounts of porcine pancreatic lipase (PPL, 0 – 1250 U/mL) produced increasing amount of the lysoPC product that could be quantified using the standard curve (Figure 5.4, panel C). Interestingly, in liposomes prepared with **11**, **12**, **16**, or **19** treated with the same PPL reaction conditions, no appreciable change in lysoPC product levels were observed (Figure 5.4, panel D). These initial results suggest the phospholipids in the prepared liposome samples are less susceptible to hydrolysis by lipases such as PPL. However, further investigation into other lipases or different conditions is warranted. The mass spec analytical technique developed here should serve as a fast and reliable assay for future investigations of lipase activity.

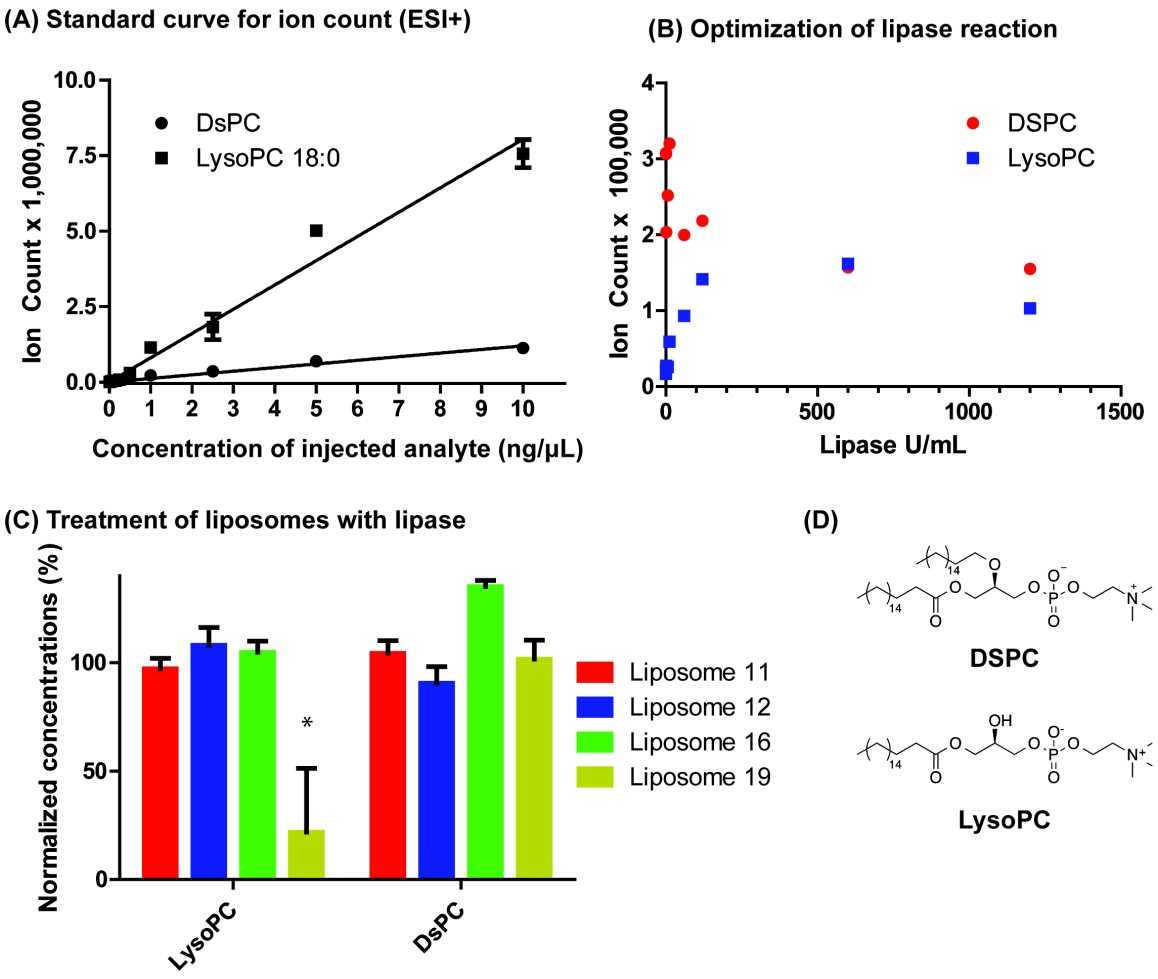

Figure 5.4. Panel A: The standard curve comparing injected samples (ng/μL) verses ion count (ESI^+). Panel B: Optimization of lipase concentration (U/mL) in the hydrolysis reaction of DSPC (10 μM). Panel C: Changes in analyte levels of liposomes (10 mM) treated with lipase (500 U/mL, 1 h) normalized to untreated liposome samples. No significant changes in DSPC levels were observed. *The apparent decrease in lysoPC for liposome **19** is due to high starting levels of lysoPC in the sample. Panel D: Structures of the analytes DSPC and the hydrolysis product lysoPC detected by mass spectrometry.

5.5 Conclusions

This proof-of-concept study suggests that cholesterol dimers bearing linkers containing ethylene glycol units can serve as efficient stabilizers of liposome membranes similar to more complex previously reported cholesterol dimers.[12-13] Through systematic variation of the number of ethylene glycol units

as well as the functional group of the linker, it was shown that longer chain dimers such as ester **16** and carbamate **19** can significantly decrease protein binding and membrane leakage compared to that of free cholesterol and may be superior in some assays to the known compound **12**. Interestingly, liposomes of **17** showed decrease stability and increased leakage compared with free cholesterol, suggesting that the shorter carbamate linkage prevented stable incorporation of this dimer into the lipid bilayer.

The beneficial effects of the ethylene glycol linkages observed in this study are fully consistent with that seen in other pegylated liposomes,[16] nanoparticles,[17] protein therapies.[18-19] Pegylation has been shown to increase bioavailability and decrease *in vivo* degradation by acting to shield the therapeutic agent from biological systems. In fact, the marketed liposomal doxorubicin contains PEG units to increase its half-life in circulation.[4] These results suggest that more detailed investigations comparing **12** with the novel dimers are warranted for potential drug delivery applications.

5.6 Experimental Methods

5.6.1 General. ^{1}H (500 MHz) and ^{13}C (125 MHz) NMR spectra were acquired on a Bruker Avance AC-III 500 instrument. Chemical shifts were reported in reference to $CDCl_3$ (7.26 for ^{1}H and 77.16 for ^{13}C). Coupling constants are reported in hertz and are reported as follows: chemical shift, multiplicity (s = singlet, d = doublet, t = triplet, q = quartet, dd = doublet of doublets, dt = double of triplets, m = multiplet, b = broad), coupling constant, and integration. High-

resolution mass spectrometry was done on a Micromass LCT Premier instrument. Melting points were obtained on a Thomas-Hoover capillary melting point apparatus and are uncorrected. Thin-layer chromatography (TLC) used EMD aluminum-backed silica plates (0.20 mm, 60 F-254) and compounds were visualized with ceric sulfate/molybdic acid. Flash chromatography used ICN silica gel (200-400 mesh) and was carried out using a gradient of either methanol (0 – 4%) in dichloromethane or ethyl acetate (0 – 30%) in hexanes. All reactions were carried out using oven-dried glassware. Dichloromethane and dimethylformamide used in reactions was purified via filtration through two columns of activated basic alumina under an atmosphere of Ar using a Glass Contour solvent purification system. Commercial ethylene glycol derivatives were dried under high vacuum to remove excess water prior to use. All other reagents were purchased from Sigma or Fisher and used as provided. 1,11-diamino-3,6,9-trioxaundecane,[20] 1,14-diamino-3,6,9,12-tetraoxatetradecane,[21] 1,17-diamino-3, 6,9,12,15-pentaheptadecane,[22] 3,6,9,12- tetraoxatetradecanedioic acid,[23] 3,6,9, 12,15-pentaheptadecanedioic acid,[23] and 3β-cholesterylamine[15] were synthesized as previously reported.

5.6.2 Liposome Preparation and *in vitro* Stability Assays. The preparation of liposomes and the stability assays shown for Figure 5.3 were conducted by the lab of Rodney Ho at the University of Washington. They are described here for reference. Stocks of phospholipids, cholesterol, and the dimers **12**-**19** were prepared in chloroform:methanol (2:1). Liposomes were prepared by adding

appropriate amounts of the stock solutions to a glass tube at a final molar ratio of 55:45 DPSC:cholesterol (dimers were calculated as 2 mol equivalents of free cholesterol). The organic solvent was removed with a stream of nitrogen and the lipids were rehydrated (PBS at 60 ˚C with sonication). Final concentrations of the liposome solutions, based on the amount of lipid added, were 10 mM. Liposome sizes were analyzed on a Nicomp 380 PSS by light scattering according to manufacturer guidelines. Serum protein binding was determined by incubating liposome samples (100 μL, 10 mM) with monkey serum (100 μL, macaque, harvested at the University of Washington, 37 ˚C, 24 h). The liposome-protein complexes were eluted through an Agarose M50 column (PBS, pH 7.4). Protein concentrations were determined with a standard BCA assay (Sigma) according to manufacturer guidelines. Liposomal stability assays in monkey (macque) serum were conducted with liposomes formulated as above but with encapsulated calcein (50 mM). Liposome samples (200 μL) were treated with PBS, FBS (30% in PBS), or macaque serum (1.8 mL, 24 h at room temperature). Release of calcein was measured on a standard plate reader and normalized between PBS negative controls and samples lysed with 5 μL of a 10% Triton X-100 solution.

5.6.3 Mass Spectrometry Methods. DSPC and 18:0 LysoPC were obtained from Avanti. Porcine pancreatic lipase (PPL) was from Lee Bioscience. PPL stocks were prepared in TBS (50 mM TrisHCl, 150 mM NaCl, pH 8.0, $CaCl_2$ 55 mM, 1% BSA). Lipase assays were carried out with 50 μL of liposome or pure

DSPC + 5 µL lipase (5500 U/mL stock) for 1 h at 37 ˚C. Stocks (10 mM) of phospholipids in chloroform:methanol (2:1) were prepared and serial diluted with chloroform:methanol (2:1) + 0.01% formic acid for the standard curve. Mass spec analysis was performed on a Waters MicromassZQ electrospray instrument fitted with a 10 µL injection loop. The standard curves were obtained with 10 µL injections and total ion counts integrated over 25 seconds from the chromatograph. Linear least squares fitting used GraphPad Prism 6.0. Lipase concentrations in the hydrolysis reaction was optimized using 0 -1250 U/mL PPL. Suspensions of pure DSPC were prepared by evaporating $CHCl_3$ solution in a glass vial with a flow of N_2, PBS pH 7.4 was added for a final lipid concentration of 10 mM and the solution was sonicated for 30 min in a standard water bath to give a cloudy suspension of liposomes.

5.6.4 Chemical Synthesis and Characterization

Amide-2-glycol dimer (13). 3,6,9-Trioxaundecanedioic acid (0.2 g, 0.9 mmol) was cooled to 4 °C and neat thionyl chloride (0.26 mL, 3.6 mmol) was added dropwise. The mixture was warmed to room temperature and stirred for 1 h. Excess thionyl chloride was removed under reduced pressure. The crude intermediate was treated with 3β-cholesterylamine (0.76 g, 1.98 mmol) in a solution of CH_2Cl_2 (3 mL). Triethylamine (0.38 mL, 2.7mmol) was then added and reaction was stirred for 16 h. The solvents were removed under reduced pressure and the reaction was purified by column chromatography to produce

compound **13** as a white solid (450 mg, 52%). ^{1}H NMR (500 MHz, Chloroform-*d*) δ 6.65 (d, *J* = 8.5 Hz, 2H), 5.35 (dt, *J* = 5.6, 2.0 Hz, 2H), 3.97 (s, 4H), 3.80 – 3.61 (m, 10H), 2.37 – 0.78 (m, 80H), 0.67 (s, 6H). ^{13}C NMR (126 MHz, $CDCl_3$) δ 168.63, 140.06, 122.11, 70.71, 70.46, 70.18, 56.66, 56.11, 50.06, 49.08, 42.29, 39.71, 39.51, 39.21, 37.85, 36.55, 36.18, 35.81, 31.84, 29.09, 28.24, 28.02, 24.28, 23.83, 22.84, 22.58, 20.98, 19.40, 18.72, 11.87.HRMS (ESI) m/z 957.8067 (M+H C62H105N2O5^{+} requires 957.8023). mp 160-164 ºC.

Ester-2-glycol dimer (14). To a stirred solution of 3,6,9-Trioxaundecanedioic acid (0.1 g, 0.45 mmol) in THF (3 mL) at 4 °C was sequentially added DCC (232 mg, 1.125 mmol), cholesterol (382 mg, 0.99 mmol), and 4-dimethylaminopyridine (5.5 mg, 0.045 mmol). The mixture was warmed to 60 °C and stirred overnight (16 h). The solution was cooled to room temperature and filtered. The filtrate was concentrated, re-suspended in CH_2Cl_2, and filtered again. The product was purified by silica column chromatography to give pure **14** as a white solid (122 mg, 28%). ^{1}H NMR (500 MHz, Chloroform-*d*) δ 5.37 (m, 2H), 4.76 – 4.63 (m, 2H), 4.12 (s, 4H), 3.80 – 3.64 (m, 10H), 2.40 – 0.81 (m, 80H), 0.67 (s, 6H). ^{13}C NMR (126 MHz, $CDCl_3$) δ 169.90, 139.40, 122.89, 74.60, 70.84, 70.64, 68.86, 56.67, 56.12, 49.99, 42.31, 39.71, 39.52, 38.07, 36.94, 36.57, 36.18, 35.81, 31.90, 31.84, 29.72, 28.24, 28.03, 27.75, 24.29, 23.84, 22.84, 22.58, 21.03, 19.32, 18.72, 11.87. HRMS (ESI) m/z 981.7549 (M + Na, C62H102O7Na^{+} requires 981.7523). mp 129-131 ºC.

Ester-3-glycol dimer (15). The synthesis was as described for **14** but using 3,6,9,12- tetraoxatetradecanedioic acid (0.7511 mmol) as the starting material to give **15** as a white solid (279.7 mg, 37%). ^{1}H NMR (500 MHz, Chloroform-*d*) δ 5.30 (m, 2H), 4.64 (m, 2H), 4.06 (s, 4H), 3.69 – 3.58 (m, 12H), 2.27– 0.77 (m, 80H), 0.61 (s, 6H). ^{13}C NMR (126 MHz, $CDCl_3$) δ 169.91, 139.39, 122.90, 74.59, 70.84, 70.64, 70.59, 68.84, 56.67, 56.12, 49.99, 42.31, 39.71, 39.52, 38.07, 36.93, 36.57, 36.18, 35.81, 33.97, 31.90, 31.84, 28.24, 28.03, 27.75, 25.62, 24.96, 24.29, 23.84, 22.85, 22.58, 21.03, 19.32, 18.72, 11.87. HRMS (ESI) m/z 1025.8036 (M+Na $C64H106O8Na^+$ requires 1025.7785). mp 111 ºC.

Ester-5-glycol dimer (16). The synthesis was as described for **14** but using 3,6, 9,12,15-pentaheptadecanedioic acid (0.741 mmol) as the starting material to give **16** as a white solid (261.6 mg, 34%). ^{1}H NMR (500 MHz, Chloroform-*d*) δ 5.40 (d, *J* = 3.7 Hz, 2H), 4.71 (ddt, *J* = 16.2, 8.1, 4.2 Hz, 2H), 4.14 (s, 4H), 3.78 – 3.64 (m, 24H), 2.35 (m, 80H), 0.69 (s, 6H). ^{13}C NMR (126 MHz, $CDCl_3$) δ 169.91, 139.39, 122.89, 74.58, 70.85, 70.62, 70.60, 70.59, 68.84, 56.67, 56.12, 49.98, 42.31, 39.71, 39.52, 38.07, 36.93, 36.57, 36.18, 35.81, 31.90, 31.84, 28.24, 28.03, 27.75, 24.29, 23.84, 22.85, 22.58, 21.03, 19.32, 18.72, 11.87. HRMS (ESI) m/z 1069.8356 (M+Na $C66H110O9Na^+$ requires 1069.8048). mp 104ºC.

Carbamate-2-glycol dimer (17). To a solution of 1,11-diamino-3,6,9-trioxaundecane (100 mg, 0.52 mmol) and cholesterol chloroformate (514 mg,

1.14 mmol) in dry dichloromethane (2 mL) at room temperature, triethylamine (283 µL, 2.08 mmol) was added dropwise. The resulting solution was stirred for 2 h. The reaction was diluted with dichloromethane (8 mL) and water was added (30 mL). The reaction was extracted with CH_2Cl_2 (2 x 15 mL) and the pooled organic layers were dried over sodium sulfate, filtered, and the solvent was removed. The crude reaction was purified by silica chromatography to give **17** as a white solid (217 mg, 41%). ^{1}H NMR (500 MHz, Chloroform-*d*) δ 5.36 (dt, *J* = 5.6, 2.1 Hz, 2H), 5.20 (s, 2H), 4.58 – 4.37 (m, 2H), 3.69 – 3.47 (m, 12H), 3.36 (q, *J* = 5.3 Hz, 4H), 2.45 – 0.76 (m, 80H), 0.67 (s, 6H). ^{13}C NMR (126 MHz, $CDCl_3$) δ 156.22, 139.84, 122.47, 74.30, 70.51, 70.25, 70.19, 56.68, 56.12, 49.99, 42.31, 40.69, 39.73, 39.52, 38.60, 37.00, 36.56, 36.18, 35.81, 31.91, 31.87, 28.25, 28.20, 28.02, 24.29, 23.84, 22.84, 22.58, 21.05, 19.36, 18.72, 11.87. HRMS (ESI) m/z 1017.8250 (M+H C64H109N2O7$^+$ requires 1017.8235). mp 137-141 ºC.

Carbamate-3-glycol dimer (18). The synthesis was as described for **17** but using 1,14-diamino-3,6,9,12-tetraoxatetradecane (0.635 mmol) as the starting material to give **18** as a white solid (436 mg, 65%). ^{1}H NMR (500 MHz, Chloroform-*d*) δ 5.47 – 5.21 (m, 4H), 4.60 – 4.42 (m, 2H), 3.77 – 3.57 (m, 12H), 3.57 (t, *J* = 5.1 Hz, 4H), 3.38 (q, *J* = 5.2 Hz, 4H), 2.46 – 0.81 (m, 80H), 0.69 (s, 6H). ^{13C} NMR (126 MHz, $CDCl_3$) δ 156.28, 139.87, 122.45, 74.25, 70.58, 70.51, 70.27, 70.24, 56.68, 56.12, 49.99, 42.31, 40.70, 39.73, 39.52, 38.61, 37.00, 36.56, 36.18, 35.81, 31.91, 31.87, 28.25, 28.20, 28.02, 24.30, 23.84, 22.84,

22.58, 21.05, 19.36, 18.72, 11.87. HRMS (ESI) m/z 1061.8538 (M+H $C_{66}H_{113}N_2O_8^+$ requires 1061.8497). mp 139-141 ºC.

Carbamate-4-glycol dimer (19). The synthesis was as described for **17** but using 1,16-diamino-3,6,9,12,15-pentaoxatetradecane (1.785 mmol) as the starting material to give **19** as a white, vicious solid (965 mg, 49%). ^{1}H NMR (500 MHz, Chloroform-*d*) δ 5.43 – 5.35 (m, 2H), 5.27 (t, *J* = 5.7 Hz, 2H), 4.50 (ddd, *J* = 16.2, 10.0, 3.7 Hz, 2H), 3.72 – 3.60 (m, 16H), 3.56 (t, *J* = 5.1 Hz, 4H), 3.37 (q, *J* = 5.3 Hz, 4H), 2.41 – 0.85 (m, 80H), 0.69 (s, 6H). ^{13}C NMR (126 MHz, $CDCl_3$) δ 156.24, 139.85, 122.46, 74.23, 70.61, 70.58, 70.52, 70.25, 70.17, 56.67, 56.11, 49.98, 42.30, 40.69, 39.72, 39.51, 38.61, 37.00, 36.55, 36.18, 35.81, 31.90, 31.86, 28.25, 28.20, 28.02, 24.29, 23.84, 22.85, 22.58, 21.04, 19.36, 18.72, 11.87. HRMS (ESI) m/z 1127.8960 (M+Na $C_{68}H_{116}N_2O_9Na^+$ requires 1127.8579). mp 104 ºC.

5.7 References

1. Sharma, A.; Sharma, U. S., Liposomes in drug delivery: Progress and limitations. *Int. J. Pharm.* **1997,** *154* (2), 123-140.

2. Pattni, B. S.; Chupin, V. V.; Torchilin, V. P., New Developments in Liposomal Drug Delivery. *Chem. Rev.* **2015**.

3. Barenholz, Y., Doxil® — The first FDA-approved nano-drug: Lessons learned. *J. Controlled Release* **2012,** *160* (2), 117-134.

4. Andreopoulou, E.; Gaiotti, D.; Kim, E.; Downey, A.; Mirchandani, D.; Hamilton, A.; Jacobs, A.; Curtin, J.; Muggia, F., Pegylated liposomal doxorubicin HCL (PLD; Caelyx/Doxil®): Experience with long-term maintenance in responding patients with recurrent epithelial ovarian cancer. *Ann. Oncol.* **2007,** *18* (4), 716-721.

5. Gambling, D.; Hughes, T.; Martin, G.; Horton, W.; Manvelian, G.; Group, f. t. S.-D. E. S., A Comparison of Depodur™, a Novel, Single-Dose Extended-Release Epidural Morphine, with Standard Epidural Morphine for Pain Relief After Lower Abdominal Surgery. *Anesth. Analg.* **2005,** *100* (4), 1065-1074.

6. Silverman, J.; Deitcher, S., Marqibo® (vincristine sulfate liposome injection) improves the pharmacokinetics and pharmacodynamics of vincristine. *Cancer Chemother. Pharmacol.* **2013,** *71* (3), 555-564.

7. Drummond, D. C.; Noble, C. O.; Hayes, M. E.; Park, J. W.; Kirpotin, D. B., Pharmacokinetics and in vivo drug release rates in liposomal nanocarrier development. *J. Pharm. Sci.* **2008,** *97* (11), 4696-4740.

8. Yeagle, P. L., Lipid regulation of cell membrane structure and function. *FASEB J.* **1989,** *3* (7), 1833-42.

9. McMullen, T. P. W.; Lewis, R. N. A. H.; McElhaney, R. N., Differential scanning calorimetric study of the effect of cholesterol on the thermotropic phase behavior of a homologous series of linear saturated phosphatidylcholines. *Biochemistry* **1993,** *32* (2), 516-522.

10. Papahadjopoulos, D.; Nir, S.; Ohki, S., Permeability properties of phospholipid membranes: Effect of cholesterol and temperature. *Biochim. Biophys. Acta* **1972,** *266* (3), 561-583.

11. Phillips, M. C.; Johnson, W. J.; Rothblat, G. H., Mechanisms and consequences of cellular cholesterol exchange and transfer. *Biochim. Biophys. Acta* **1987,** *906* (2), 223-276.

12. Huang, Z.; Szoka, F. C., Sterol-Modified Phospholipids: Cholesterol and Phospholipid Chimeras with Improved Biomembrane Properties. *J. Am. Chem. Soc.* **2008,** *130* (46), 15702-15712.

13. Huang, Z.; Jaafari, M. R.; Szoka, F. C., Disterolphospholipids: Nonexchangeable Lipids and Their Application to Liposomal Drug Delivery. *Angew. Chem. Int. Ed.* **2009,** *48* (23), 4146-4149.

14. Lohse, P.; Chahrokh-Zadeh, S.; Lohse, P.; Seidel, D., Human lysosomal acid lipase/cholesteryl ester hydrolase and human gastric lipase: identification of the catalytically active serine, aspartic acid, and histidine residues. *J. Lipid Res.* **1997,** *38* (5), 892-903.

15. Sun, Q.; Cai, S.; Peterson, B. R., Practical Synthesis of 3β-Amino-5-cholestene and Related 3β-Halides Involving i-Steroid and Retro-i-Steroid Rearrangements. *Org. Lett.* **2008,** *11* (3), 567-570.

16. Immordino, M. L.; Dosio, F.; Cattel, L., Stealth liposomes: review of the basic science, rationale, and clinical applications, existing and potential. *Int. J. Nanomed.* **2006,** *1* (3), 297-315.

17. Vugmeyster, Y.; Entrican, C. A.; Joyce, A. P.; Lawrence-Henderson, R. F.; Leary, B. A.; Mahoney, C. S.; Patel, H. K.; Raso, S. W.; Olland, S. H.; Hegen, M.; Xu, X., Pharmacokinetic, Biodistribution, and Biophysical Profiles of TNF Nanobodies Conjugated to Linear or Branched Poly(ethylene glycol). *Bioconjug. Chem.* **2012,** *23* (7), 1452-1462.

18. Milla, P.; Dosio, F.; Cattel, L., PEGylation of Proteins and Liposomes: a Powerful and Flexible Strategy to Improve the Drug Delivery. *Curr. Drug Metab.* **2012,** *13* (1), 105-119.

19. Harris, J. M.; Chess, R. B., Effect of pegylation on pharmaceuticals. *Nat. Rev. Drug Discov.* **2003,** *2* (3), 214-221.

20. Lill, A.; Scholich, K.; Stark, H., Synthesis of novel dansyl-labeled Celecoxib derivatives. *Tetrahedron Lett.* **2013,** *54* (49), 6682-6686.

21. Ciuffarin, E.; Isola, M.; Leoni, P., Catalysis in aprotic solvents. Inter- and intramolecular hydrogen bonding complexation. *J. Org. Chem.* **1981,** *46* (15), 3064-3070.

22. Cao, Y.; Yang, J., Development of a Folate Receptor (FR)-Targeted Indenoisoquinoline Using a pH-Sensitive N-Ethoxybenzylimidazole (NEBI) Bifunctional Cross-Linker. *Bioconjug. Chem.* **2014,** *25* (5), 873-878.

23. Wittmann, V.; Takayama, S.; Gong, K. W.; Weitz-Schmidt, G.; Wong, C.-H., Ligand Recognition by E- and P-Selectin: Chemoenzymatic Synthesis and Inhibitory Activity of Bivalent Sialyl Lewis x Derivatives and Sialyl Lewis x Carboxylic Acids. *J. Org. Chem.* **1998,** *63* (15), 5137-5143.

APPENDIX A

NMR Spectra

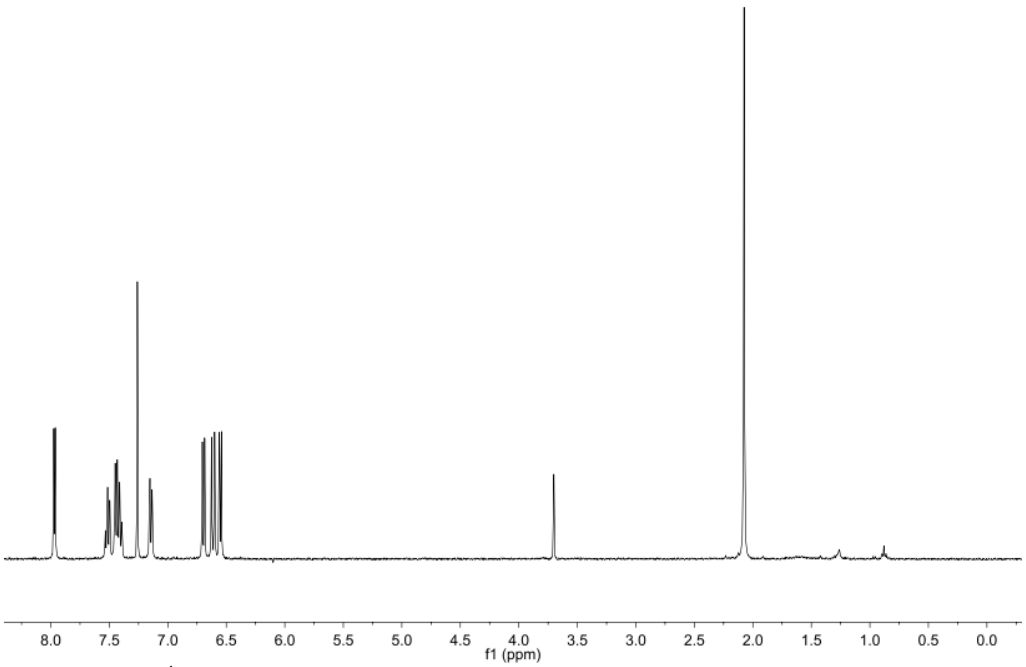

Figure 6.1 ^{1}H NMR (400 MHz, $CDCl_3$) spectrum of **3**.

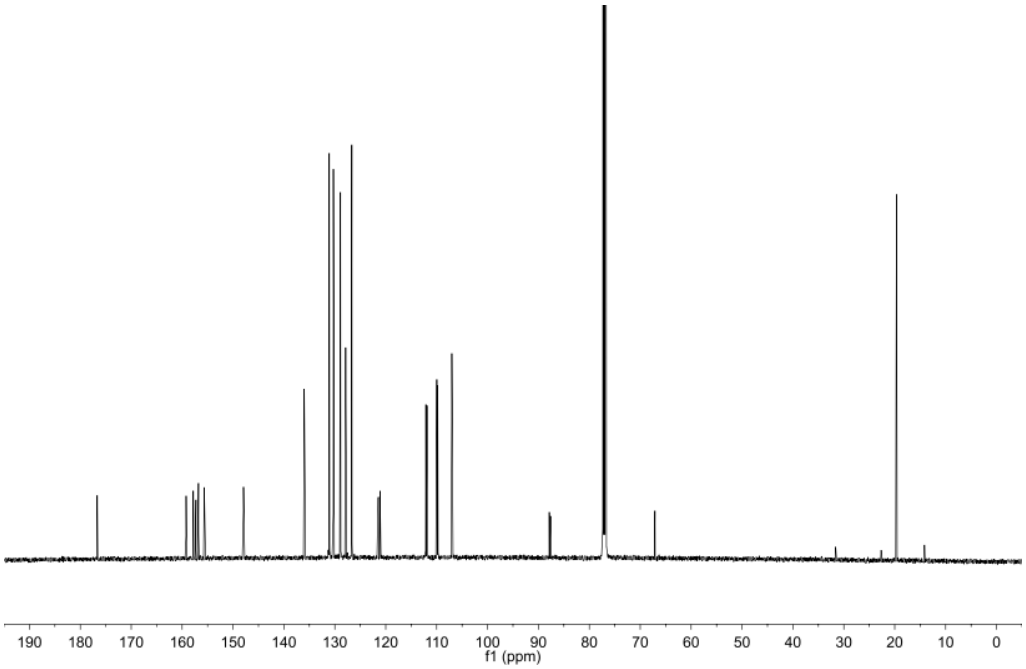

Figure 6.2. ^{13}C NMR (126 MHz, $CDCl_3$) spectrum of **3**.

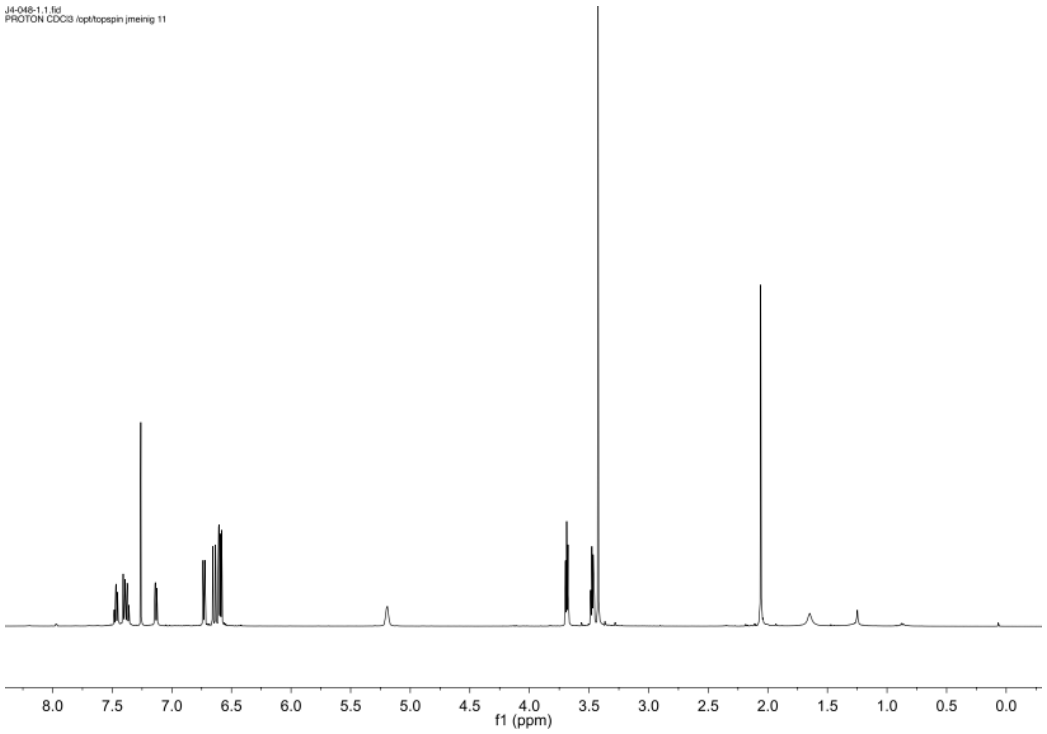

Figure 6.3. ^{1}H NMR (500 MHz, $CDCl_3$) spectrum of **4**.

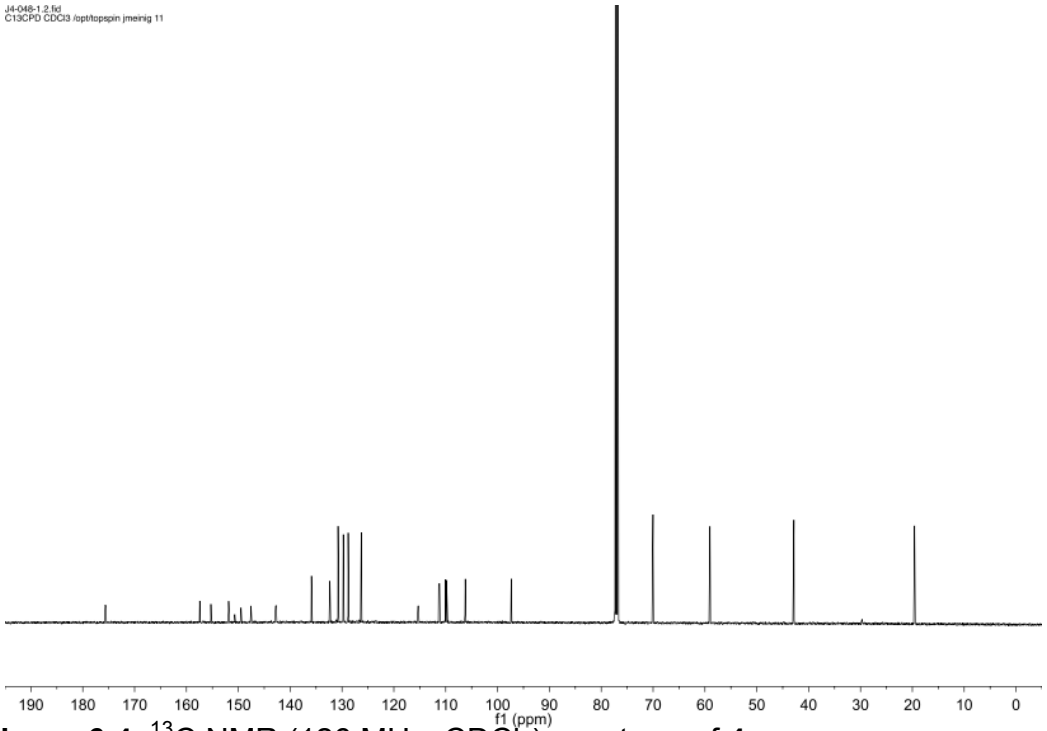

Figure 6.4. ^{13}C NMR (126 MHz, $CDCl_3$) spectrum of **4**.

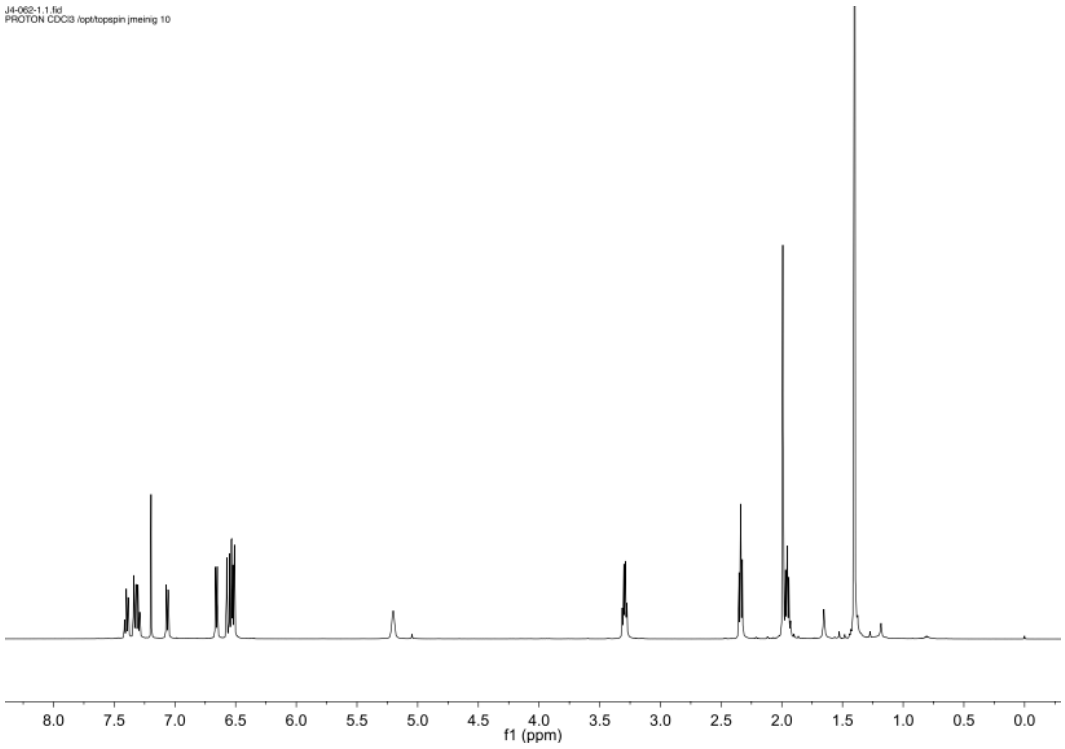

Figure 6.5. ^{1}H NMR (500 MHz, $CDCl_3$) spectrum of **5**.

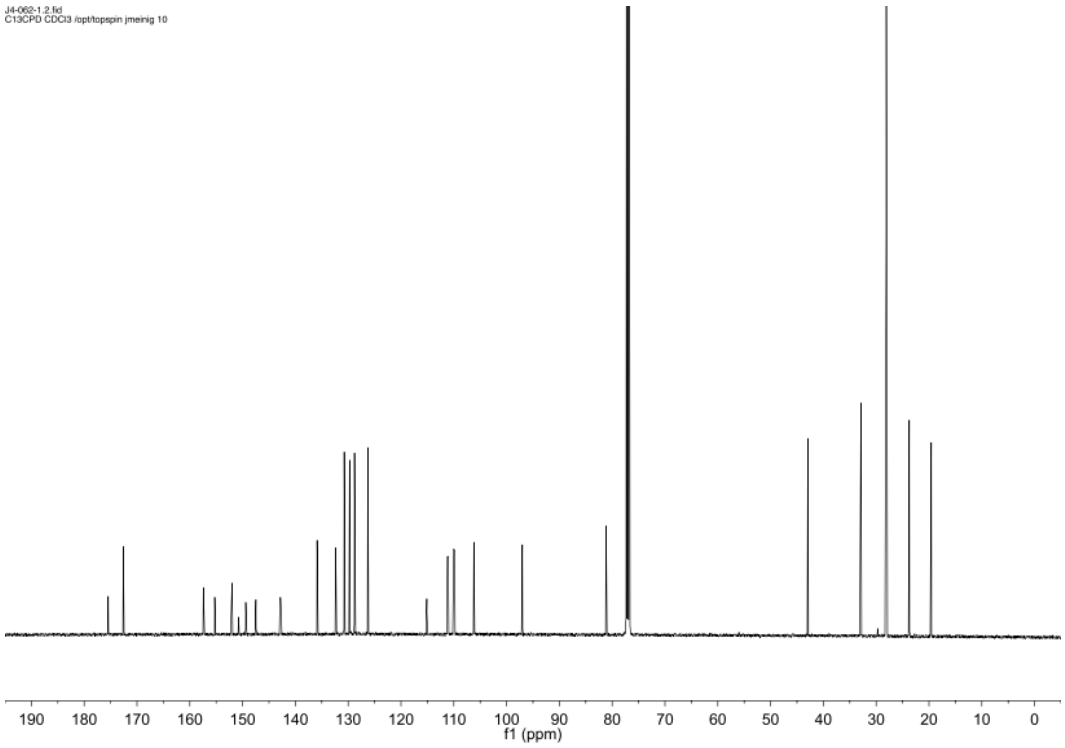

Figure 6.6. ^{13}C NMR (126 MHz, $CDCl_3$) spectrum of **5**.

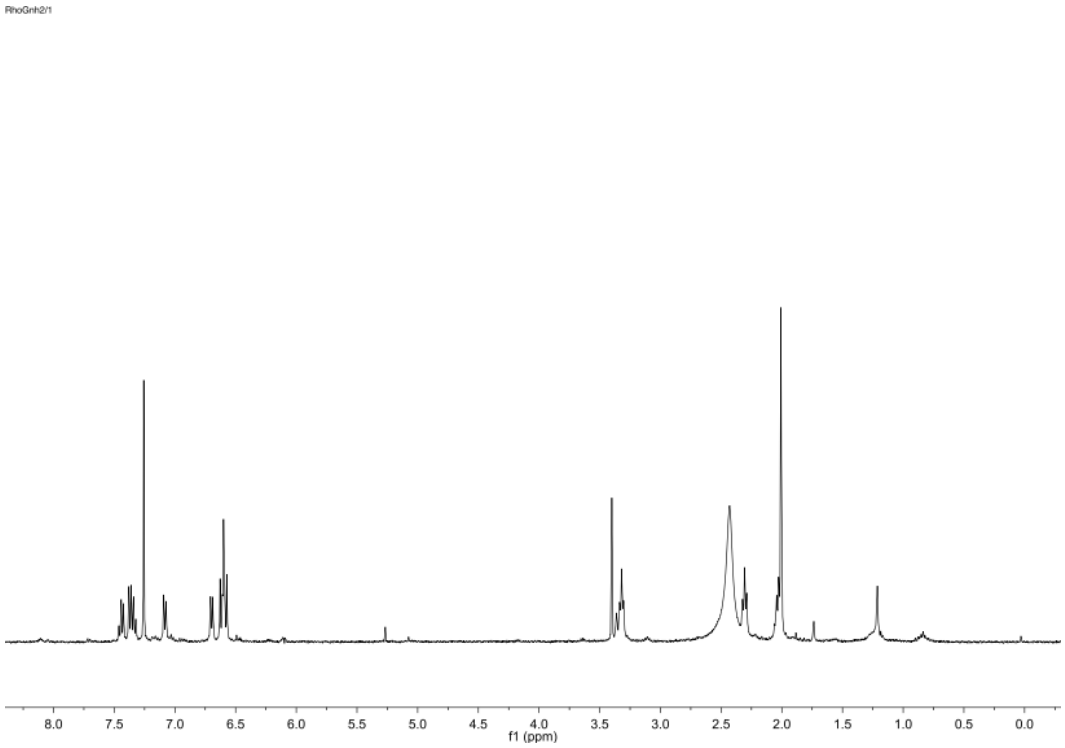

Figure 6.7. ^{1}H NMR (400 MHz, $CDCl_3$) spectrum of **6**.

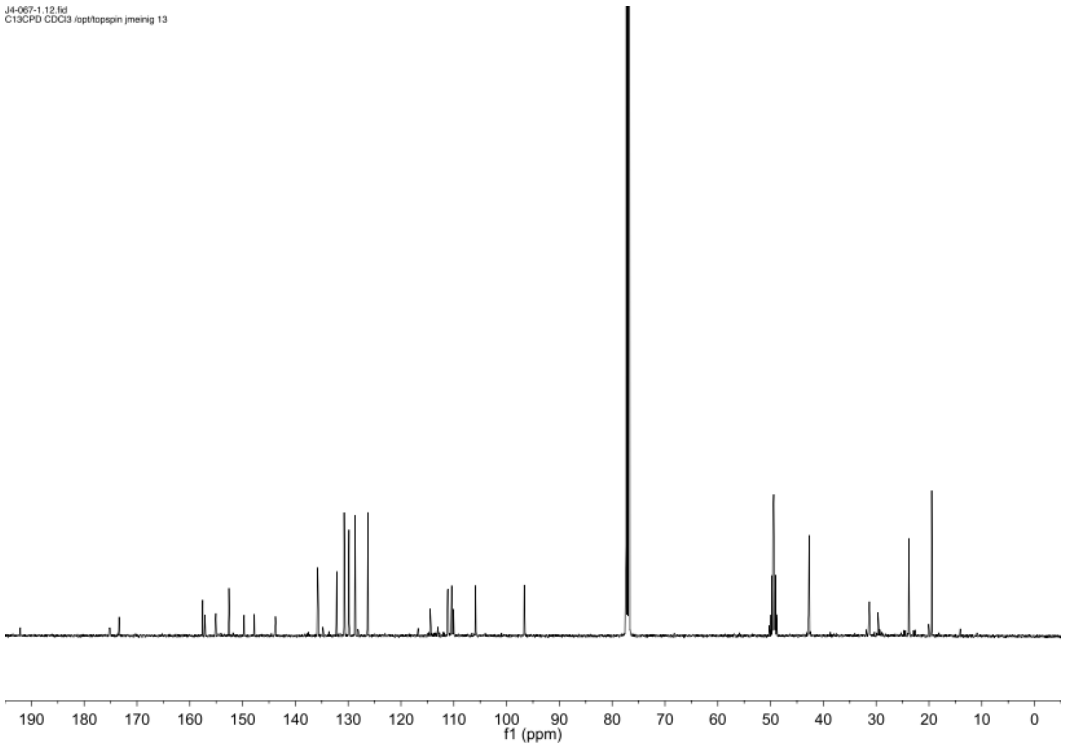

Figure 6.8. ^{13}C NMR (126 MHz, $CDCl_3/CD_3OD$, 9:1) spectrum of **6**.

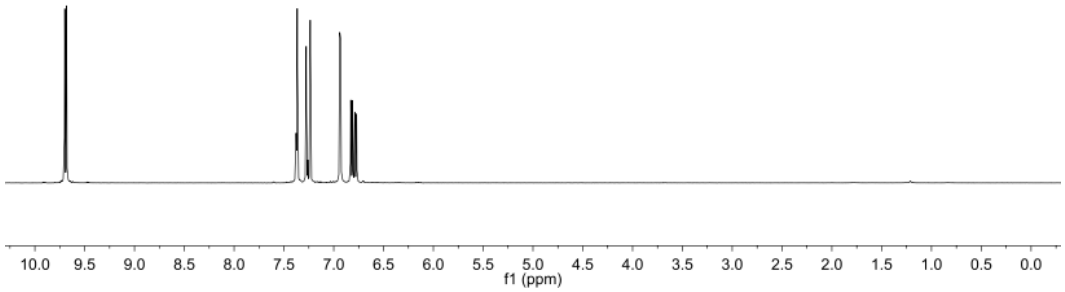

Figure 6.9. ^{1}H NMR (400 MHz, $CDCl_3$) spectrum of **7**.

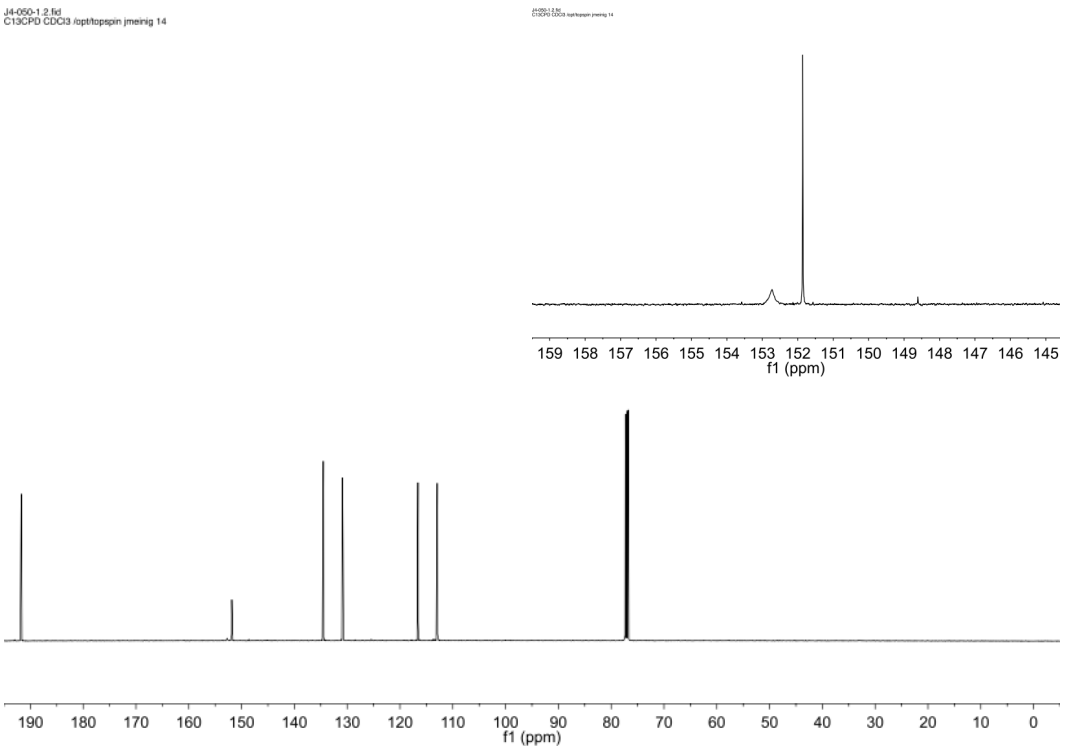

Figure 6.10. ^{13}C NMR (126 MHz, $CDCl_3$) spectrum of **7**. The inset shows an expansion to illustrate the broad resonance of the *ipso* carbon of the furan linked to the nitro group.

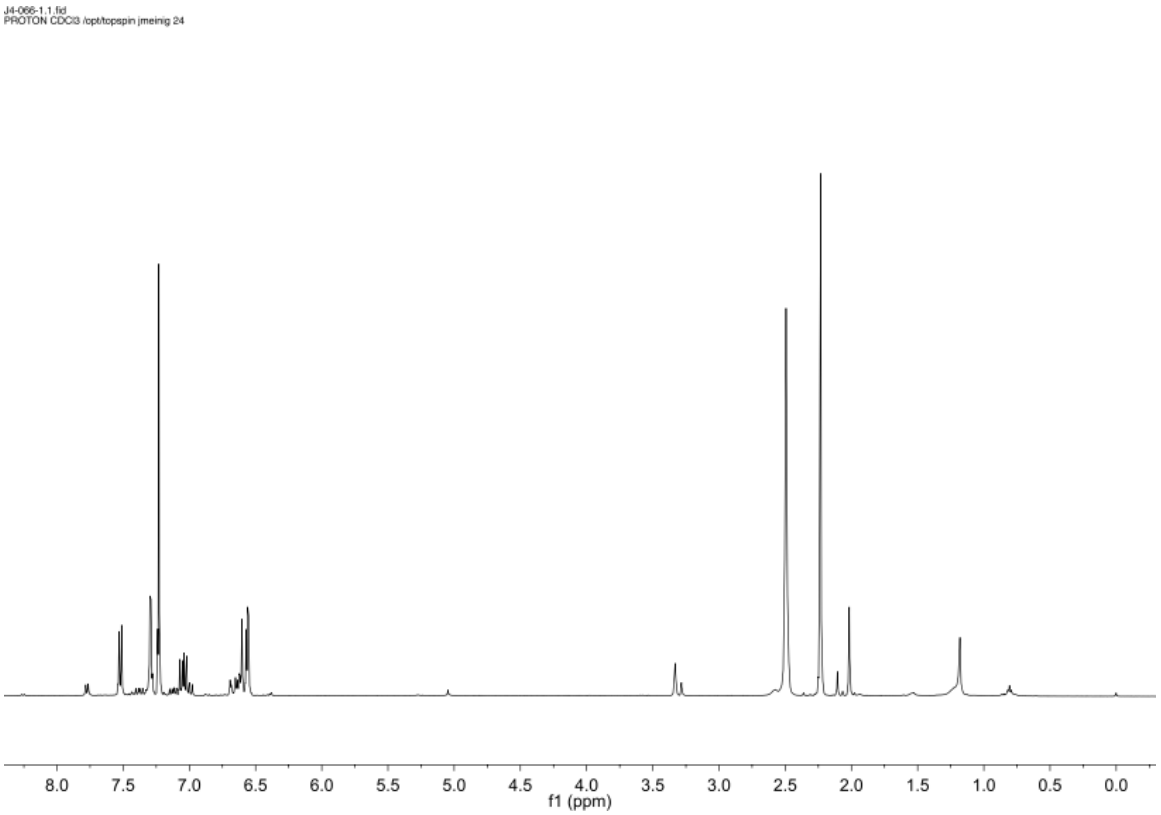

Figure 6.11. ^{1}H NMR (500 MHz, $CDCl_3/CD_3OD$, 9:1) spectrum of **9**.

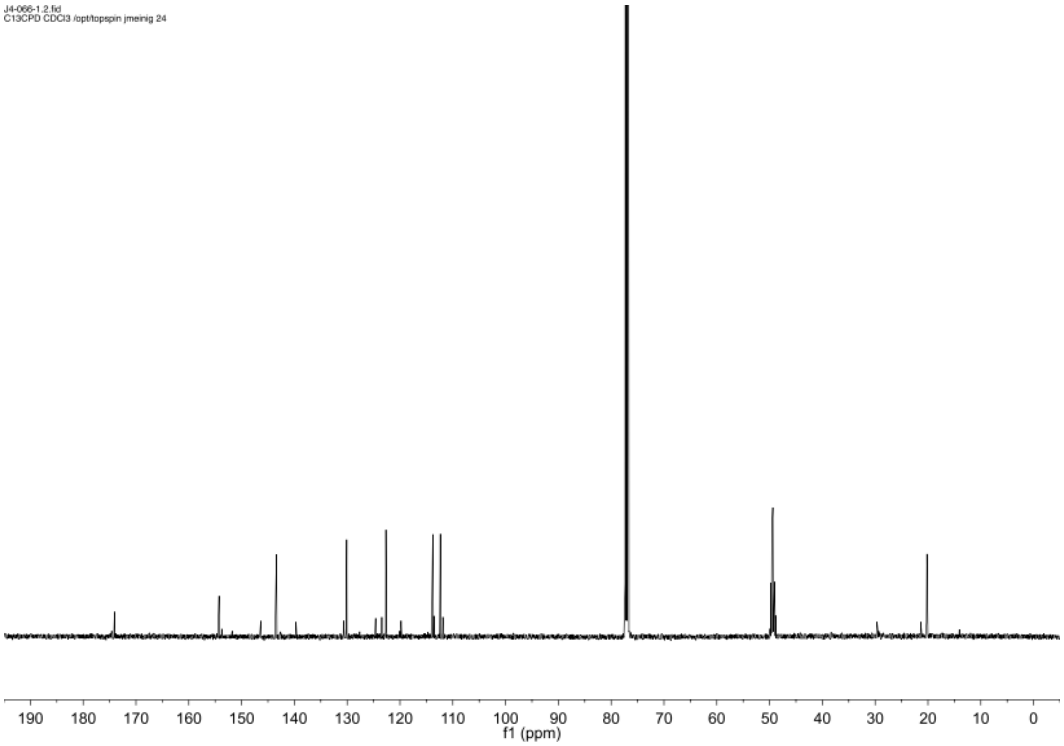

Figure 6.12. ^{13}C NMR (500 MHz, $CDCl_3/CD_3OD$, 9:1) spectrum of **9**.

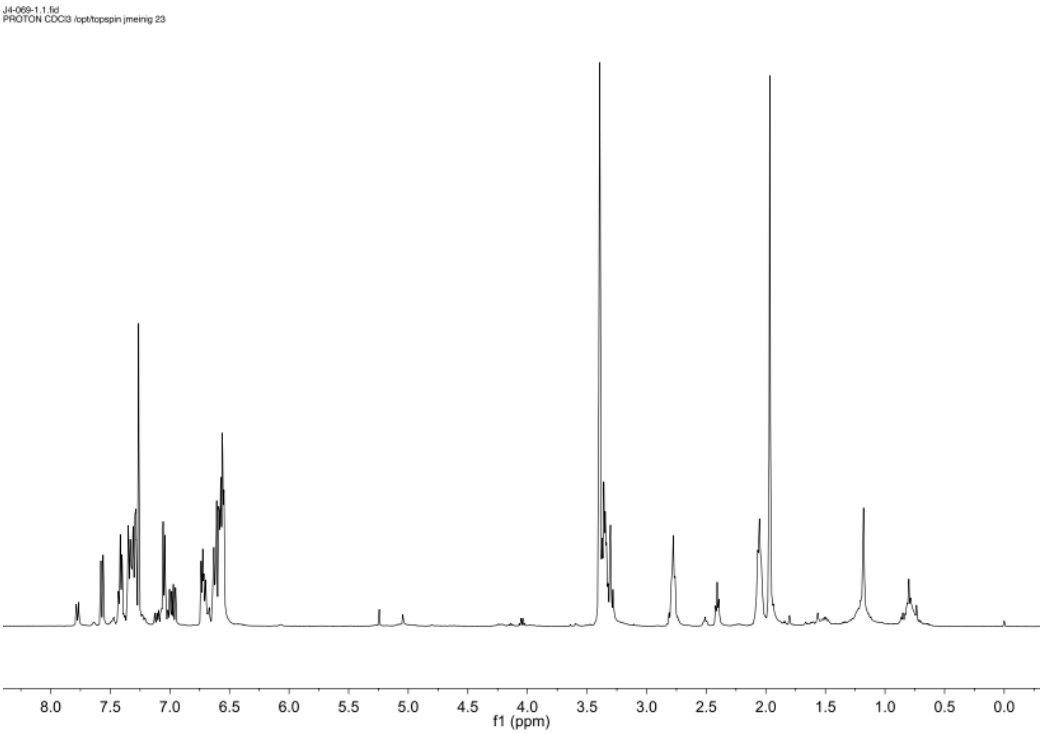

Figure 6.13. ^{1}H NMR (500 MHz, $CDCl_3/CD_3OD$, 9:1) spectrum of **10**.

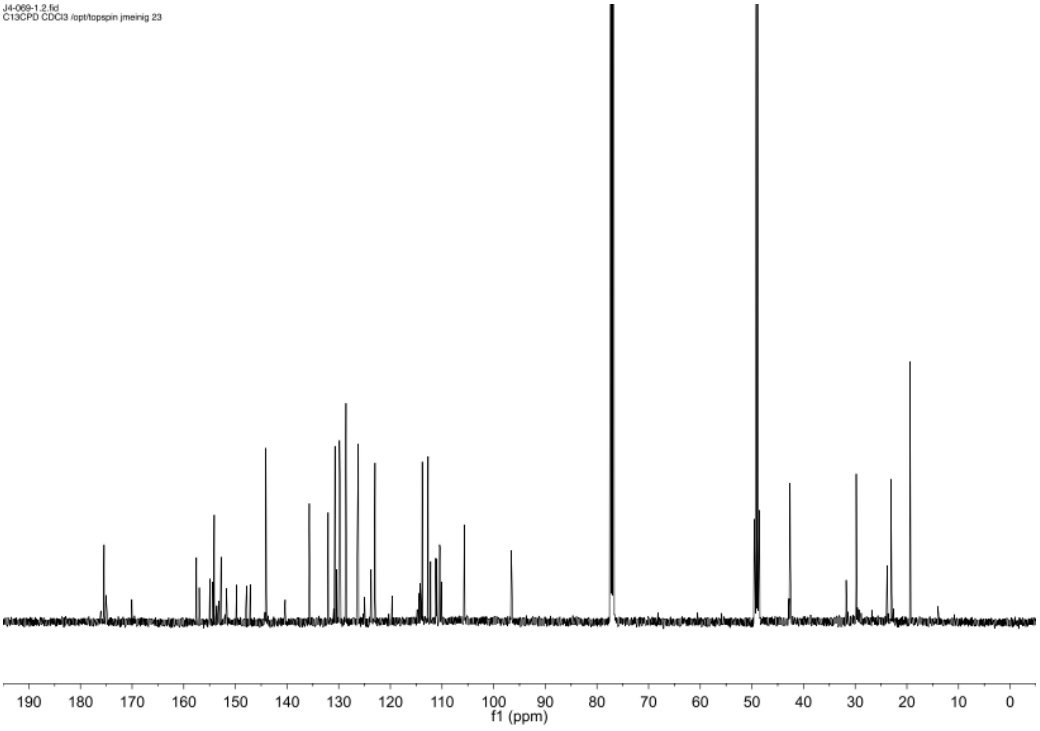

Figure 6.14. ^{13}C NMR (126 MHz, $CDCl_3/CD_3OD$, 9:1) spectrum of **10**.

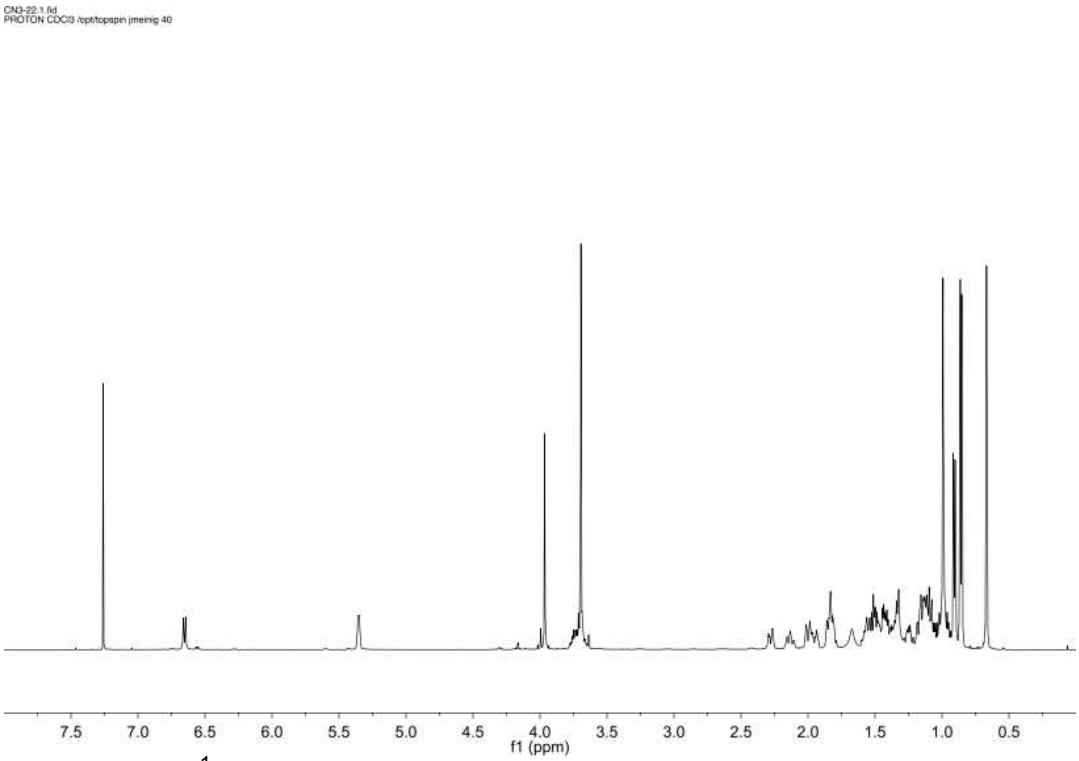

Figure 6.15. ^{1}H NMR of compound **13** in $CDCl_3$**.**

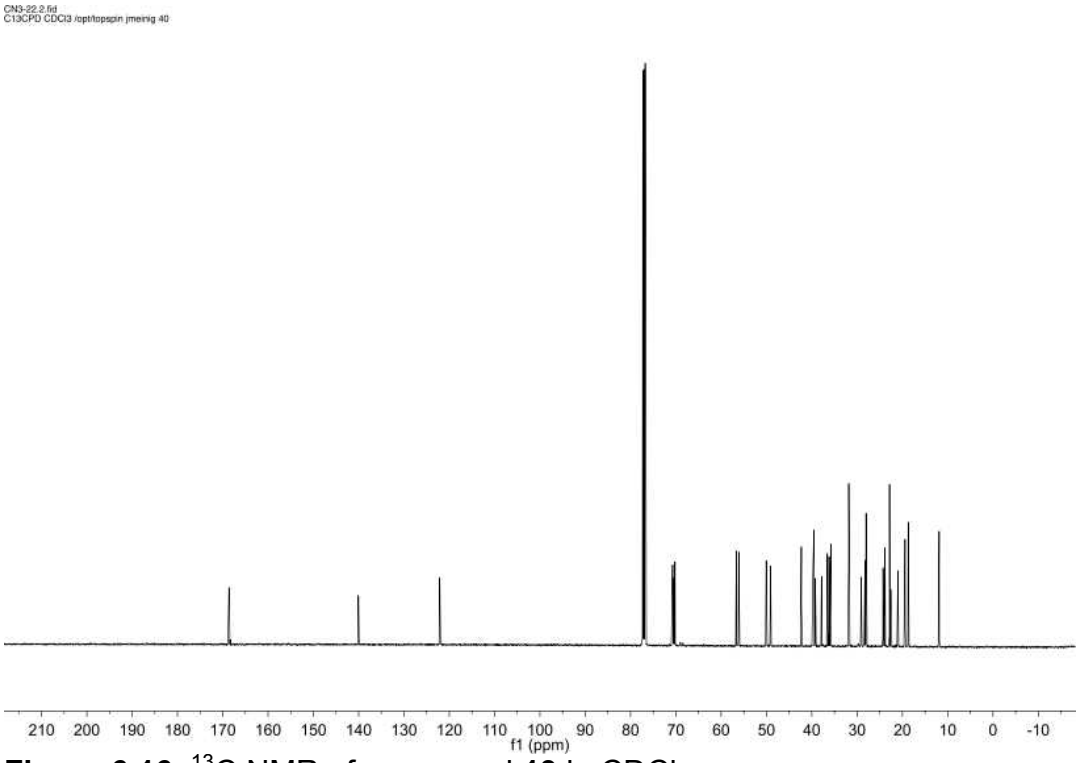

Figure 6.16. ^{13}C NMR of compound **13** in $CDCl_3$.

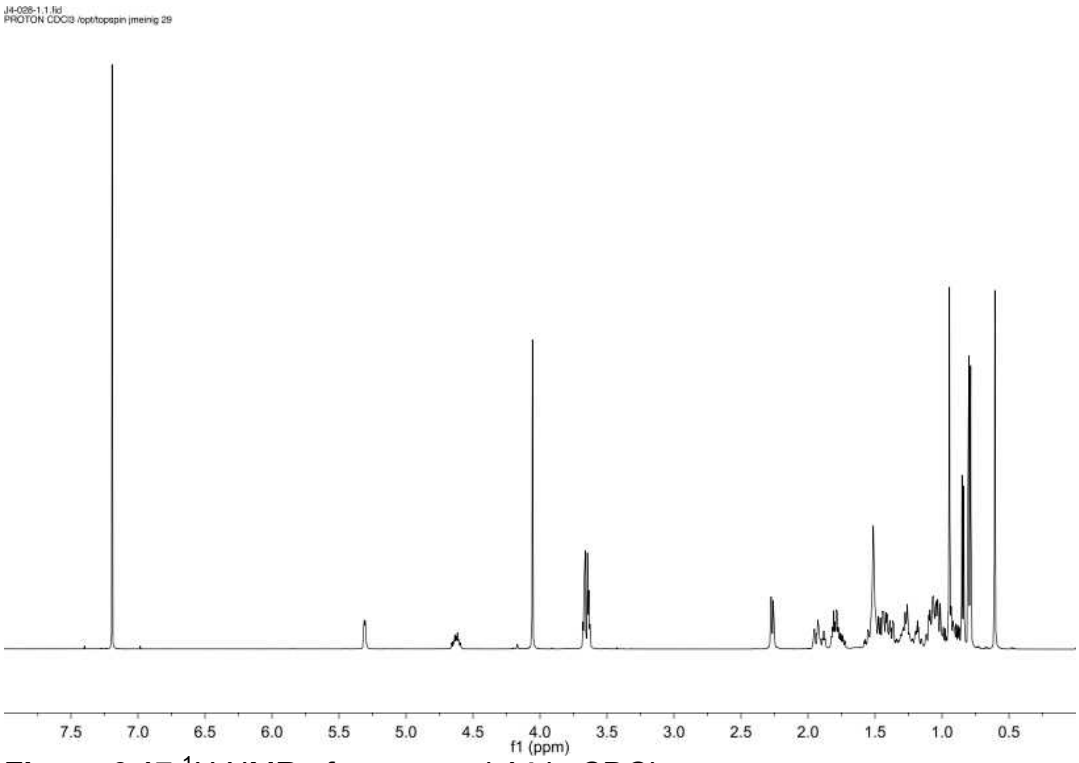

Figure 6.17 ^{1}H NMR of compound **14** in $CDCl_3$**.**

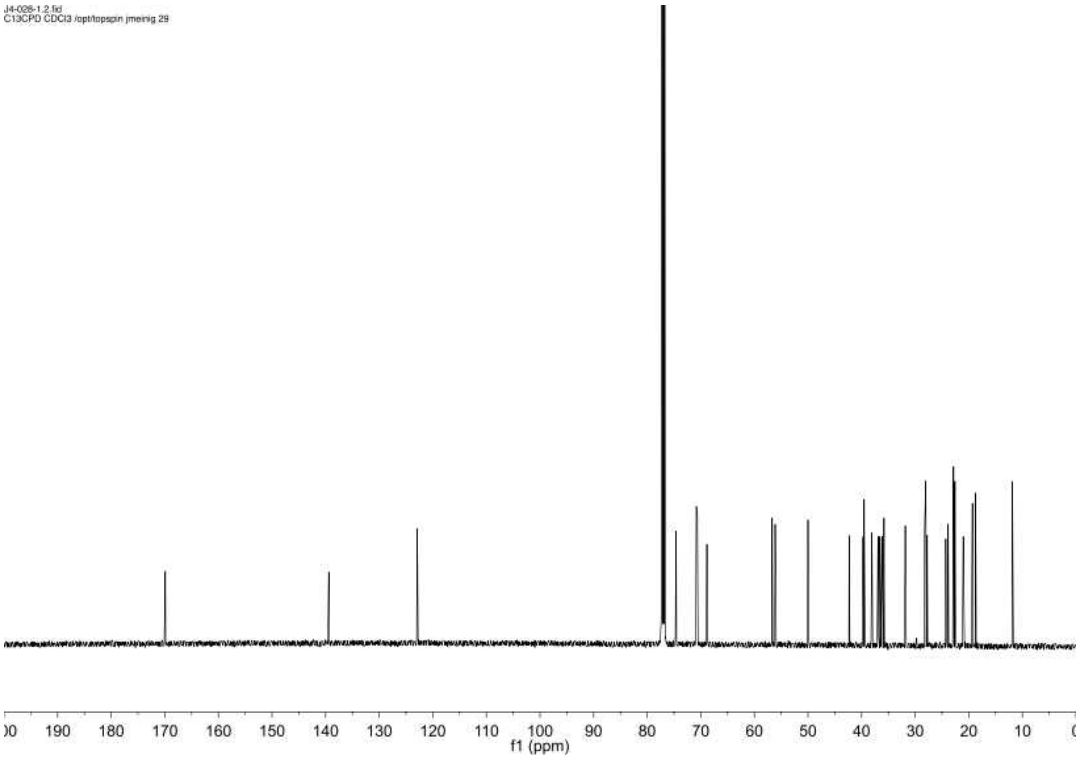

Figure 6.18 ^{13}C NMR of compound **14** in $CDCl_3$.

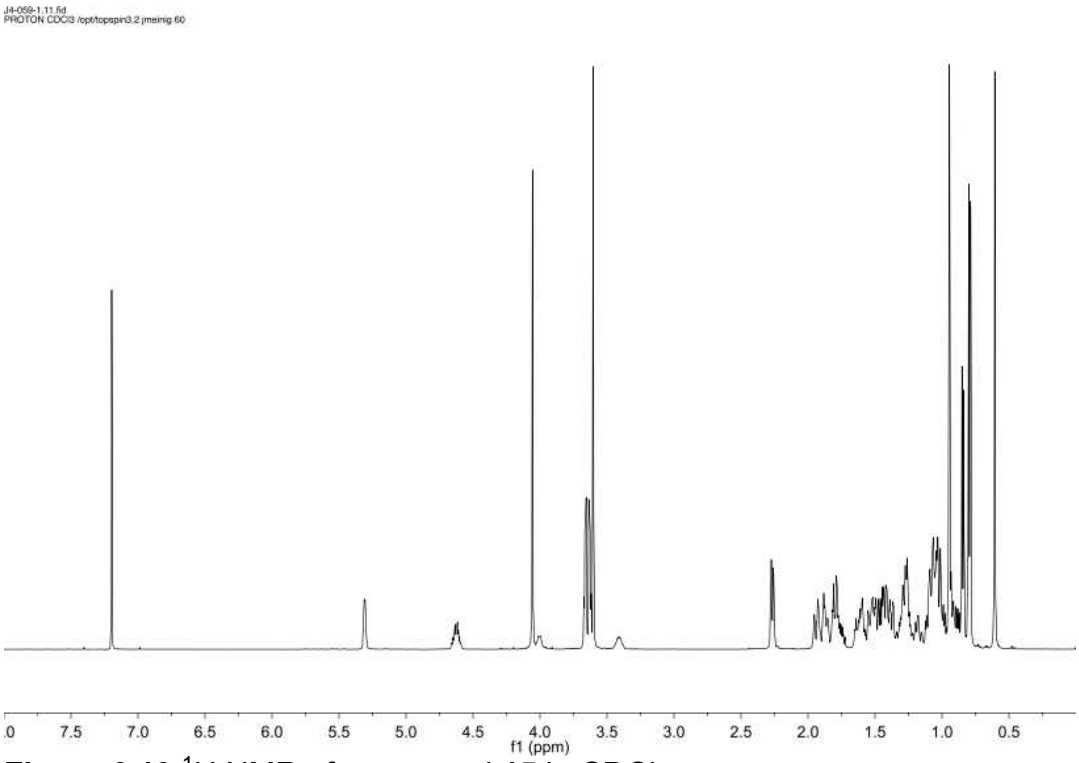

Figure 6.19 ^{1}H NMR of compound **15** in $CDCl_3$**.**

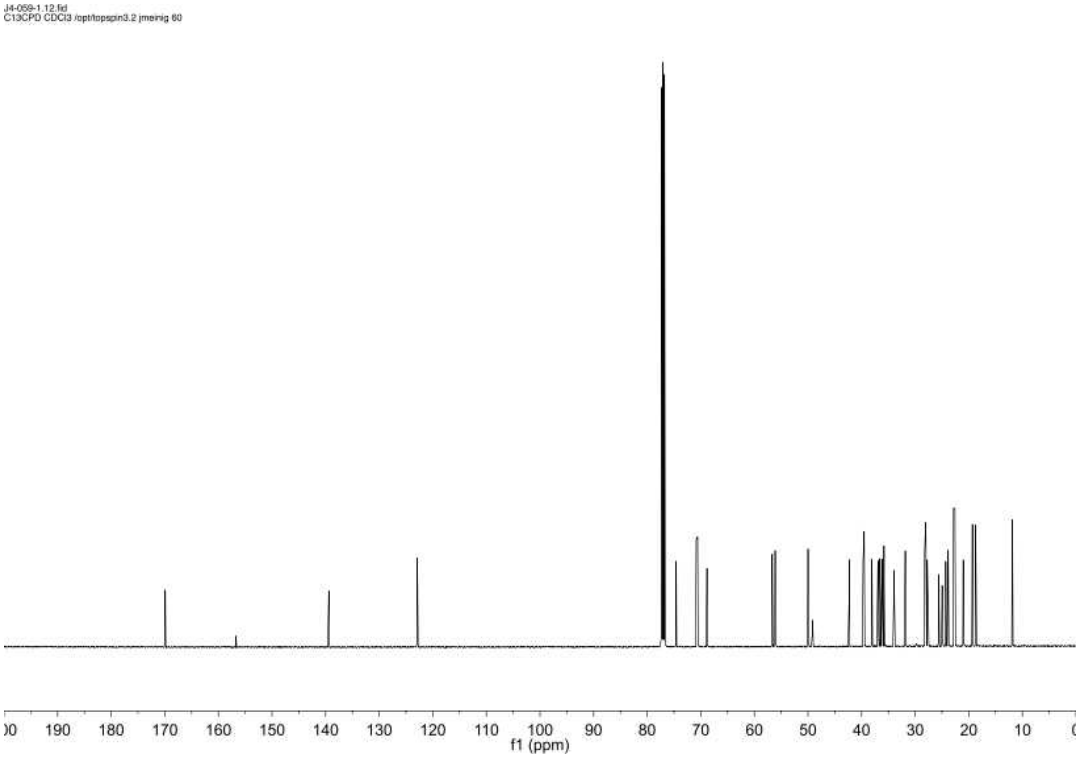

Figure 6.20 ^{13}C NMR of compound **15** in $CDCl_3$.

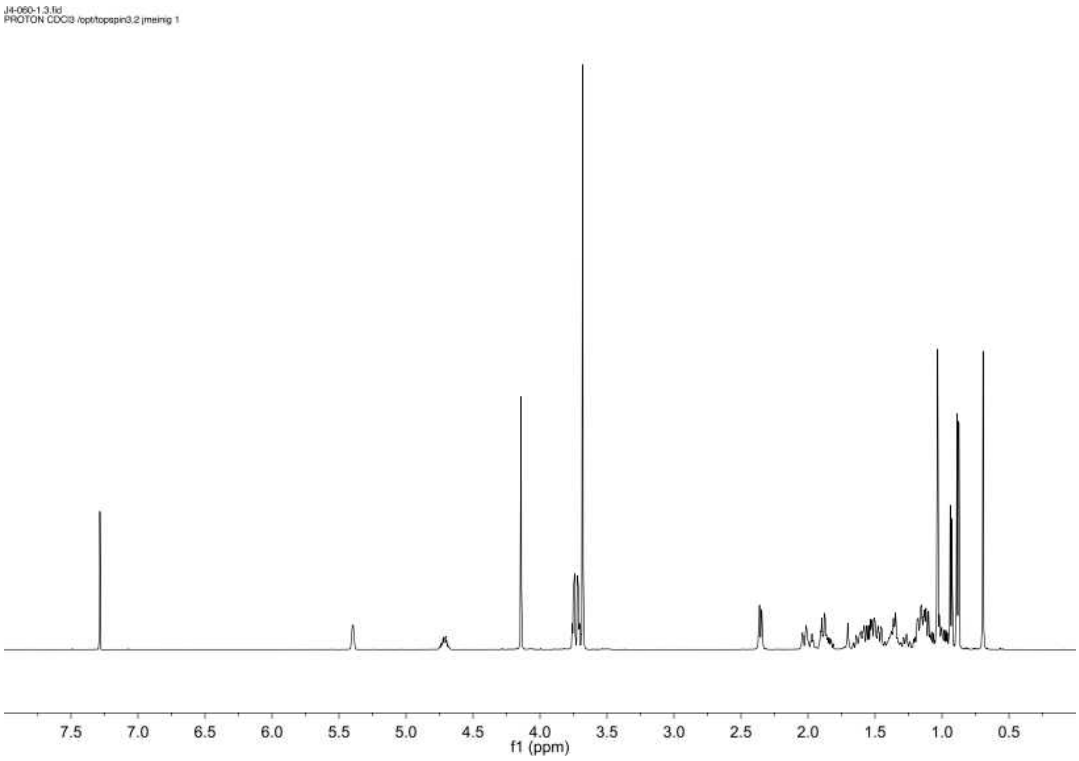

Figure 6.21 ^{1}H NMR of compound **16** in $CDCl_3$**.**

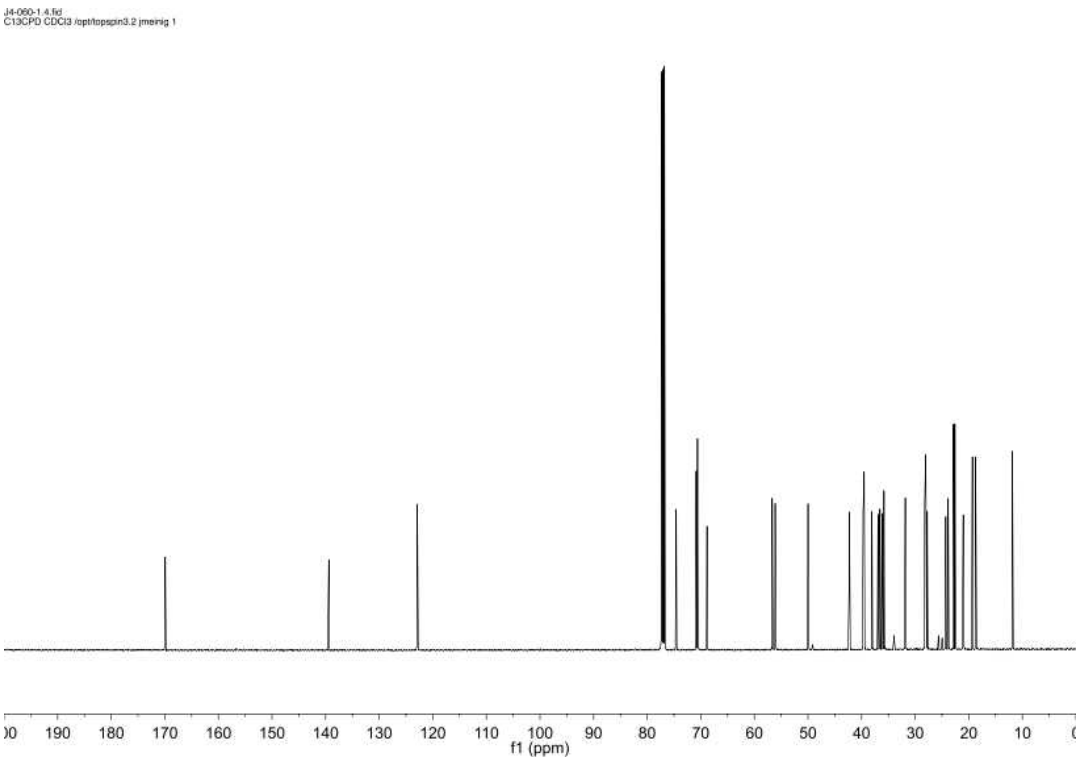

Figure 6.22 ^{13}C NMR of compound **16** in $CDCl_3$.

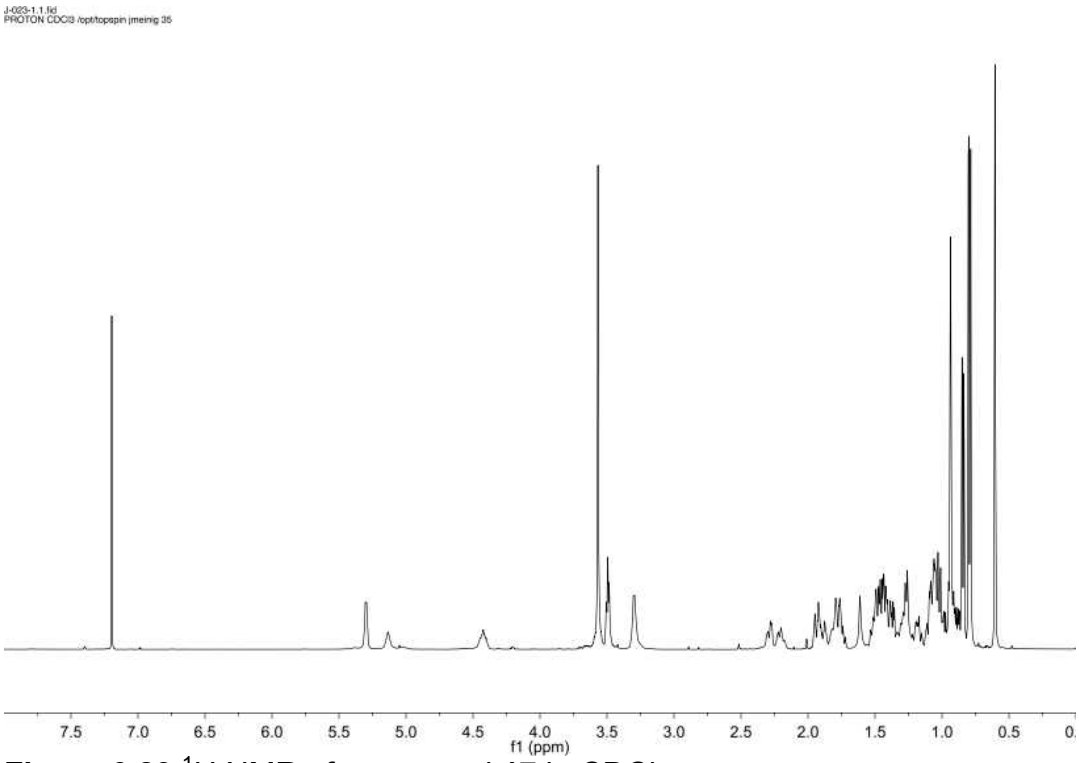

Figure 6.23 ^{1}H NMR of compound **17** in $CDCl_3$**.**

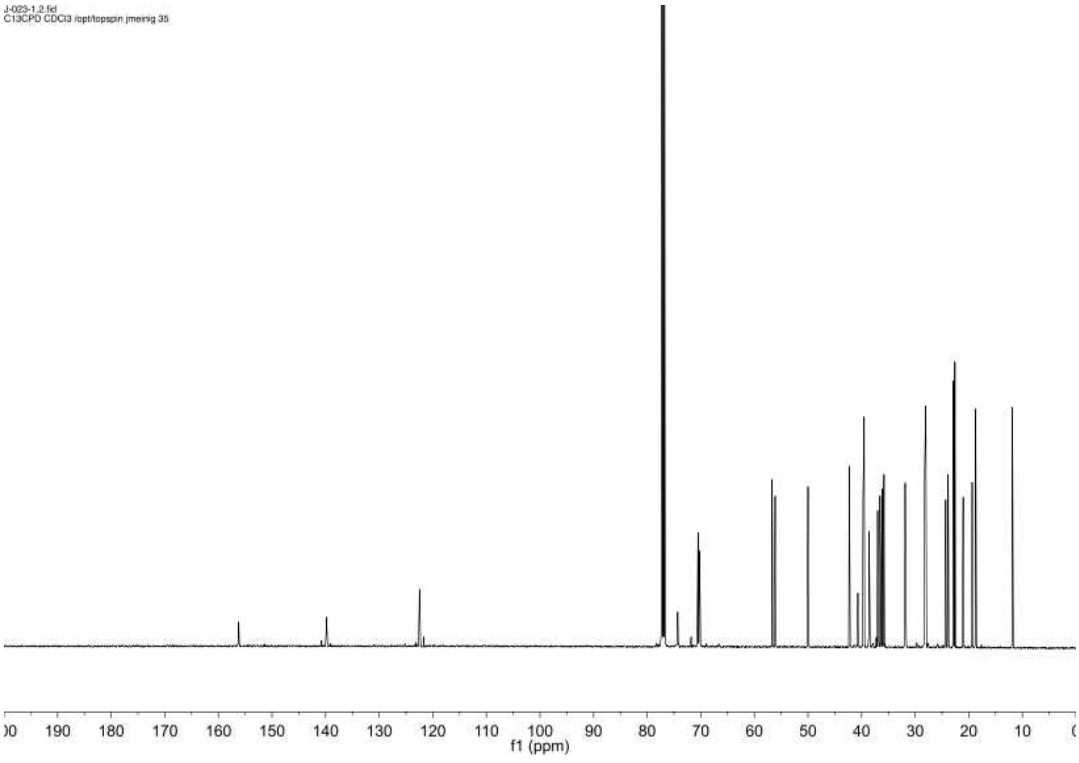

Figure 6.24 ^{13}C NMR of compound **17** in $CDCl_3$.

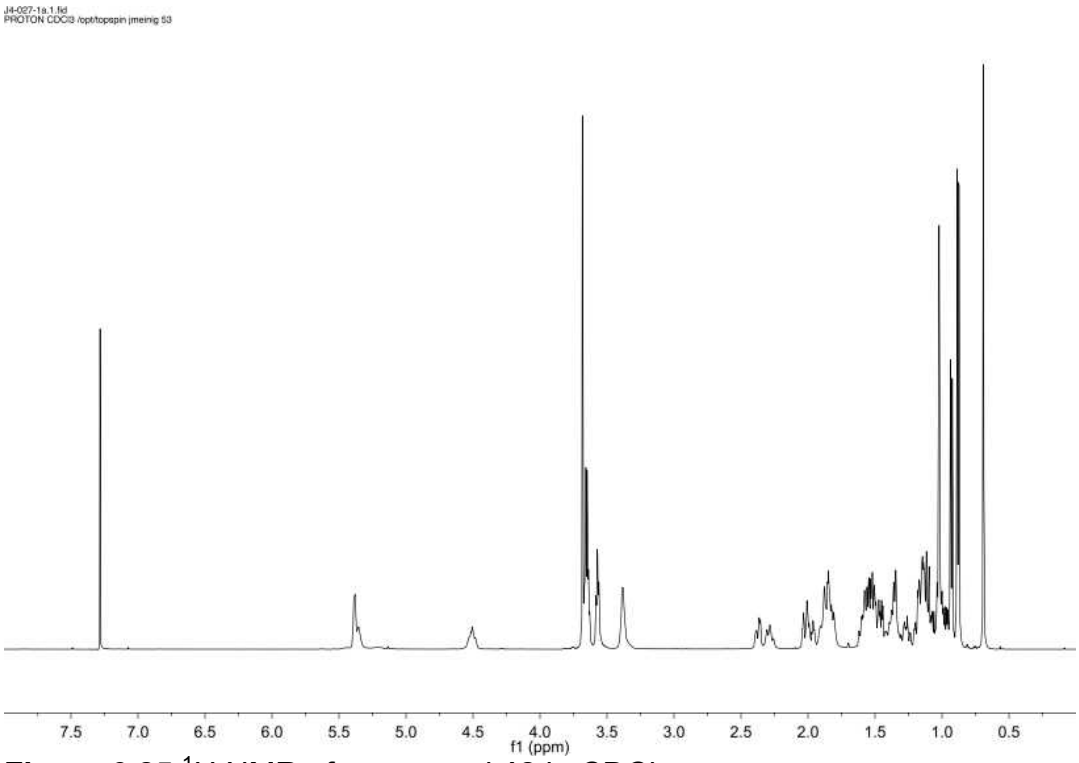

Figure 6.25 ^{1}H NMR of compound **18** in $CDCl_3$**.**

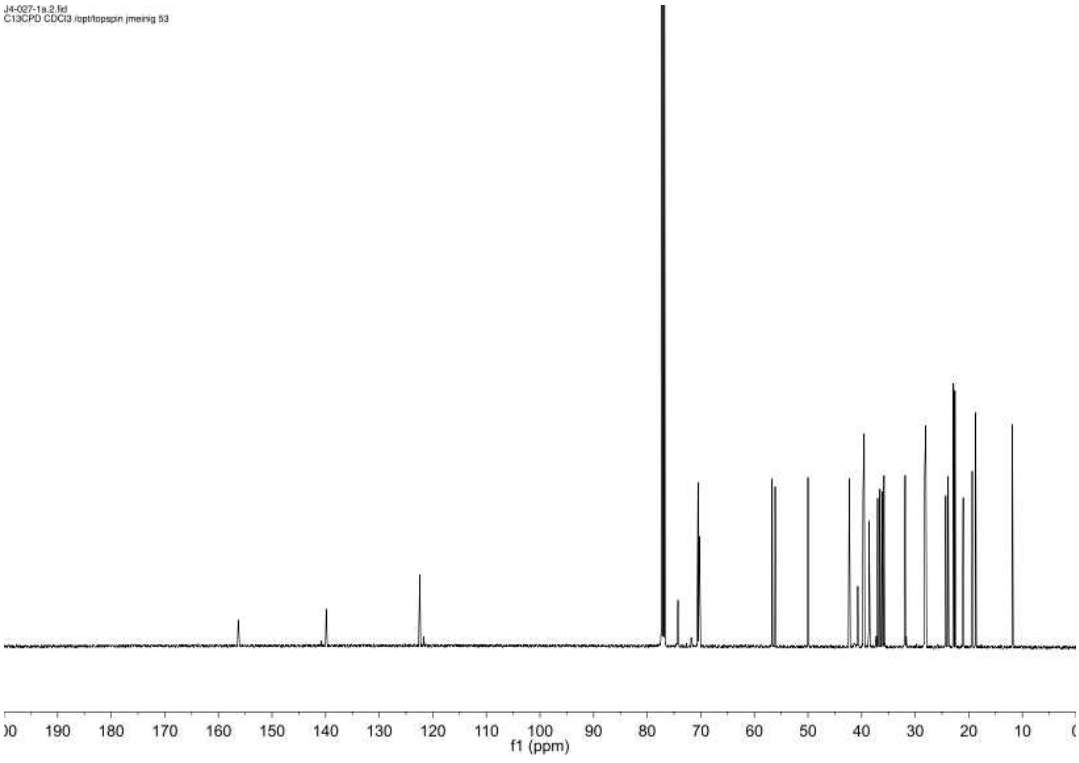

Figure 6.26 ^{13}C NMR of compound **18** in $CDCl_3$.

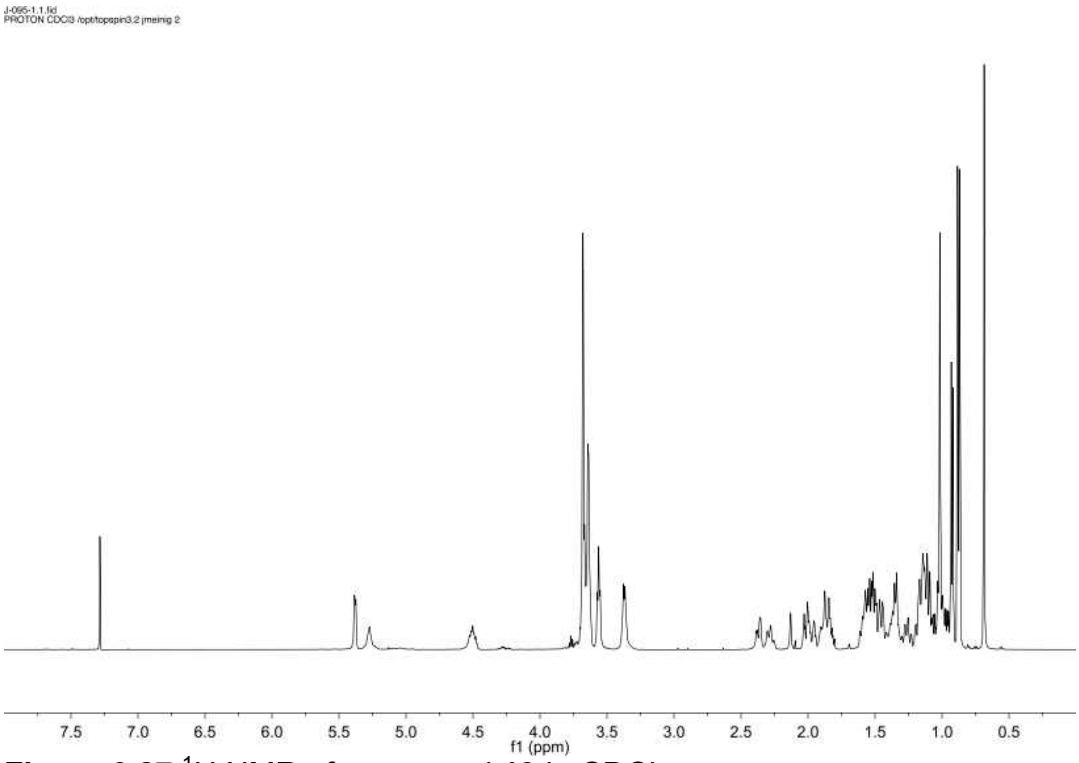

Figure 6.27 ^{1}H NMR of compound **19** in $CDCl_3$**.**

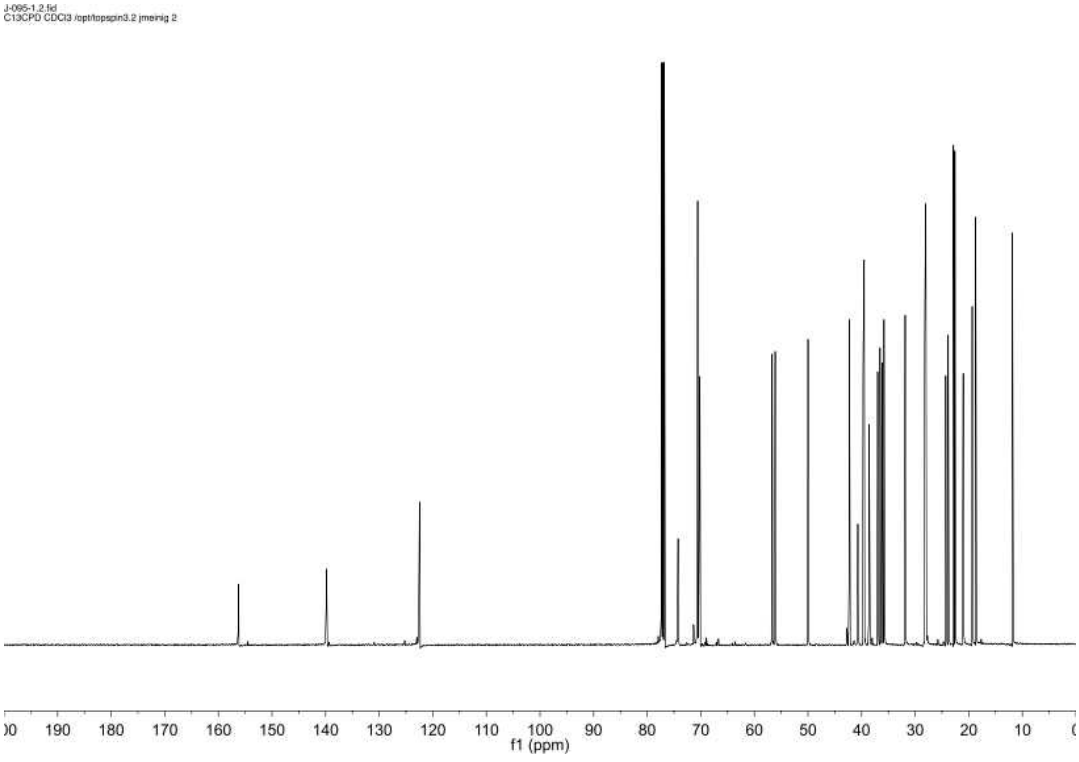

Figure 6.28 ^{13}C NMR of compound **19** in $CDCl_3$.

APPENDIX B

List of cell lines used in this research

Cell Line	Media	Growth	Organism	Tissue	Source	Notes
HeLa	DMEM +10%FBS +Pen/Strep	Adherent	Human	Cervical	ATCC	ATCC #CCL-2
CV-1	DMEM +10%FBS +Pen/Strep	Adherent	Green monkey	Kidney	ATCC	ATCC #CCL-70
Jurkat	RPMI-1680 +10%FBS +Pen/Strep	Suspension	Human	T-Cell Lymphocyte	ATCC	ATCC #TIB-152
CHO-K1	DMEM/F12K +10%FBS +Pen/Strep	Adherent	Hamster	Ovary	ATCC	ATCC #CLL-61
KBM-7	IMEM +10%FBS +Pen/Strep	Suspension	Human	T-Cell Lymphocyte	Haplogen	Haploid line
THP-1	RPMI-1680 +10%FBS +Pen/Strep	Suspension	Human	Macrophage	ATCC	ATCC #TIB-202

List of plasmids

Name	Gene Product	Gene Species	Backbone	Expression Type	Source	Notes
pEGFP-N1	EGFP	n/a	pEGFP-N1	Mammalian	Clonetech	Clonetech #6085-1
mCerulean-N1	Cerulean	n/a	pEGFP-N1	Mammalian	Addgene	Addgene #54742
mCerulean-C1	Cerulean	n/a	pEGFP-N1	Mammalian	Addgene	Addgene #54604
Ub-G76V-YFP	Ubiquitin (G76V)-YFP	Human Ub	pEGFP-N1	Mammalian	Addgene	Addgene #11949
Ub-G76V-Cer	Ubiquitin (G76V)-Cerulean	Human Ub	pEGFP-N1	Mammalian	Subcloning	N1 fusion